AN ANALYSIS ON MULTINUCLEON TRANSFER REACTIONS WITHIN THE FRAMEWORK OF STOCHASTIC MEAN-FIELD APPROACH

A THESIS SUBMITTED TO
THE GRADUATE SCHOOL OF NATURAL AND APPLIED SCIENCES
OF
MIDDLE EAST TECHNICAL UNIVERSITY

BY

MERT ARIK

IN PARTIAL FULFILLMENT OF THE REQUIREMENTS
FOR
THE DEGREE OF MASTER OF SCIENCE
IN
PHYSICS

JULY 1 2024

Approval of the thesis:

AN ANALYSIS ON MULTINUCLEON TRANSFER REACTIONS WITHIN THE FRAMEWORK OF STOCHASTIC MEAN-FIELD APPROACH

submitted by **MERT ARIK** in partial fulfillment of the requirements for the degree of **Master of Science in Physics Department, Middle East Technical University** by,

Prof. Dr. Naci Emre Altun
Dean, Graduate School of **Natural and Applied Sciences**

Prof. Dr. Seçkin Kürkcüoğlu
Head of Department, **Physics**

Prof. Dr. Osman Yılmaz
Supervisor, **Department of Physics, METU**

Prof. Dr. Şakir Ayık
Co-supervisor, **Physics Department, Tennessee Tech University**

Examining Committee Members:

Prof. Dr. İsmail Turan
Department of Physics, METU

Prof. Dr. Osman Yılmaz
Department of Physics, METU

Prof. Dr. Tahmasib Aliyev
Department of Physics, METU

Prof. Dr. Seçkin Kürkcüoğlu
Department of Physics, METU

Prof. Dr. Bülent Yılmaz
Department of Physics, Ankara University

Date:01.07.2024

I hereby declare that all information in this document has been obtained and presented in accordance with academic rules and ethical conduct. I also declare that, as required by these rules and conduct, I have fully cited and referenced all material and results that are not original to this work.

Name, Surname: Mert Arık

Signature :

ABSTRACT

AN ANALYSIS ON MULTINUCLEON TRANSFER REACTIONS WITHIN THE FRAMEWORK OF STOCHASTIC MEAN-FIELD APPROACH

Arık, Mert
M.S., Department of Physics
Supervisor: Prof. Dr. Osman Yılmaz
Co-Supervisor: Prof. Dr. Şakir Ayık

July 1 2024, 79 pages

Multinucleon transfer (MNT) reactions involving heavy projectile and target combinations stand as a promising method for synthesizing yet unknown neutron-rich isotopes and neutron-rich superheavy elements, which may not be possible using hot or cold fusion, fission, or fragmentation reactions. In this thesis, MNT mechanisms in low-energy heavy-ion reactions are investigated within the framework of a quantal diffusion approach based on the stochastic mean-field (SMF) theory. The SMF approach provides a microscopic approach beyond time-dependent Hartree-Fock theory that includes mean-field fluctuations. The quantal transport coefficients, the charge, and mass dispersions of the fragments are calculated to analyze the primary and secondary fragment distributions in MNT reactions, and the results are compared with the experimental data. The observed agreement between the experimental data and SMF results highlights the effectiveness of the quantal diffusion mechanism based on the SMF approach, which does not include any adjustable parameters other than standard parameters of Skyrme energy density functional.

Keywords: Nuclear Diffusion Theory, Low energy Heavy-ion Reactions, Multinucleon Transfer Reactions, Time-Dependent Hartree Fock Theory, Stochastic Mean-field Theory

ÖZ

ÇOKLU-NÜKLEON TRANSFER REAKSİYONLARININ STOKASTİK ORTALAMA ALAN YAKLAŞIMI ÇERÇEVESİNDE ANALİZİ

Arık, Mert
Yüksek Lisans, Fizik Bölümü
Tez Yöneticisi: Prof. Dr. Osman Yılmaz
Ortak Tez Yöneticisi: Prof. Dr. Şakir Ayık

Temmuz 1 2024 , 79 sayfa

Ağır mermi ve hedef iyon kombinasyonlarını içeren çoklu-nükleon transfer (MNT) reaksiyonları, sıcak veya soğuk füzyon, fisyon veya parçalanma reaksiyonları kullanılarak sentezlenmesi mümkün olmayabilecek, henüz bilinmeyen nötron zengini izotopları ve nötron zengini süper ağır elementleri sentezlemek için umut verici bir yöntem olarak öne çıkmaktadır. Bu tezde, düşük enerjili ağır iyon reaksiyonlarında MNT mekanizması, stokastik ortalama-alan (SMF) teorisine dayalı kuantal difüzyon yaklaşımı çerçevesinde incelenmektedir. SMF yaklaşımı, ortalama alan dalgalanmalarını içeren, zamana bağımlı Hartree-Fock teorisinin ötesinde mikroskobik bir yaklaşım sağlar. Kuantal taşıma katsayıları, fragmanların yük ve kütle dağılımları hesaplanarak MNT reaksiyonlarındaki birincil ve ikincil fragman dağılımları analiz edilir ve sonuçlar deneysel verilerle karşılaştırılır. Deneysel veriler ile SMF sonuçları arasındaki gözlemlenen uyum, Skyrme enerji yoğunluk fonksiyonunun standart parametreleri dışında herhangi bir ayarlanabilir parametre içermeyen SMF yaklaşımına dayalı kuantal difüzyon mekanizmasının etkililiğini vurgulamaktadır.

Anahtar Kelimeler: Nükleer Difüzyon Teorisi, Düşük enerjili Ağır-iyon Reaksiyonları, Çoklu-nucleon Transfer Reaksiyonları, Zamana Bağlı Hartree Fock Teorisi, Stokastik Ortalama-alan Teorisi

To my beloved friends and family.

"We're all on one road, and we're only passin' through."

- Leonard Cohen

ACKNOWLEDGMENTS

This work was completed with significant assistance from numerous people. This effort would not have been possible without their emotional support. I want to extend my genuine thanks to some of them for their unconditional aid, though I wish I could thank everyone who contributed to this project.

First and foremost, I want to sincerely thank my supervisor, Osman Yılmaz, for helping me to finish my Master's thesis. I would also like to extend my heartfelt thanks to my co-supervisor, Prof. Dr. Şakir Ayık. Their vast knowledge, experience, and trust in my abilities have been invaluable throughout my academic journey. I am grateful for the past three years and the progress I have made, which would not have been possible without their exceptional supervision.

I want to thank Prof. Dr. Sait Umar for his insightful discussions and for providing the TDHF code and assistance throughout this work. I would also like to thank Assoc. Prof. Samet Bağçe for the delightful discussions and his assistance with bureaucratic matters, regardless of the circumstances.

I want to thank my dear friend, Oğulcan Sönmez, for always being there for me and showing me that the bonds of friendships cannot be shackled by space and time. I would also like to thank my housemate Umut Gülcan for his valuable emotional support and the free house therapy sessions I received in exchange for free backgammon lessons. I am also grateful to Çağdaş Ulus Ağca for his exceptional presence as both a physicist and a close friend and a housemate. His passion for physics and relentless dedication to his field inspired me to delve deeper into my subject. I would also like to thank Arda Hasar for his enjoyable conversations and comfortable silence.

I am profoundly thankful to Ilgın Sıla Arıcı, my closest. Together, we have navigated numerous challenges, shared peaceful moments, and experienced times that were sometimes happy, sometimes blue. I am glad that I ran into you and dear Milka.

I wish to express my heartfelt gratitude to my mother, Mefaret Üstündal, who has been my shelter, guiding pole star, and dear friend throughout my entire life, along with her dog, Lina, for the pure joy and companionship she has brought into our lives. I am and will always remain deeply thankful for everything she has taught me

I acknowledge that this project is partially supported by the Scientific and Technological Research Council of Turkey, TUBITAK, with Grant No. 122F150.

TABLE OF CONTENTS

ABSTRACT v

ÖZ vii

ACKNOWLEDGMENTS x

TABLE OF CONTENTS xii

LIST OF TABLES xiv

LIST OF FIGURES xv

LIST OF ABBREVIATIONS xx

CHAPTERS

1 INTRODUCTION 1

2 QUANTAL TRANSPORT APPROACH BASED ON SMF THEORY 7

  2.1 Langevin equation for nucleon transfer 8

  2.2 Quantal diffusion coefficients 11

  2.3 Potential energy of the di-nuclear system 12

  2.4 Primary and Secondary Product Distribution of the Reaction Products 15

    2.4.1 Probability Distributions of Primary Reaction Fragments . . . 15

    2.4.2 Probability Distributions of Primary FF Fragments 17

    2.4.3 Probability Distributions of Secondary Reaction Fragments . . 17

3 QF AND FF IN THE $^{48}\mathrm{Ca} + {}^{244}\mathrm{Pu}$ AND $^{86}\mathrm{Kr} + {}^{198}\mathrm{Pt}$ REACTIONS . . . 19

3.1 Mean Reaction Dynamics in TDHF 21
3.1.1 Mean values of reaction observables 21
3.1.2 Mean Drift Path and Reduced Curvature Parameters 24
3.2 SMF results 26
3.2.1 Covariances of fragment charge and mass distributions 26
3.2.2 Primary Mass Distribution 28
4 PRIMARY AND SECONDARY ISOTOPE PRODUCTION IN $^{250}\mathrm{Cf}$ + $^{232}\mathrm{Th}$ REACTION 33
4.1 Mean Reaction Dynamics in TDHF 34
4.1.1 Mean values of reaction observables 34
4.1.2 Mean Drift Path and Reduced Curvature Parameters 37
4.1.2.1 Reduced Curvature Parameter β 37
4.1.2.2 Reduced Curvature Parameter α 41
4.2 SMF results 44
4.2.1 Covariances of fragment charge and mass distributions 44
4.2.2 Primary Isotope Distribution 46
4.2.3 Secondary Isotope Distribution 49
5 CONCLUSION 53
REFERENCES 57

LIST OF TABLES

TABLES

Table 3.1 Results of the TDHF calculations for the ^{48}Ca + ^{244}Pu system at $E_{\text{c.m.}} = 203.2$ MeV for the tip orientation of the ^{244}Pu nucleus and the ^{86}Kr + ^{198}Pt system at $E_{\text{c.m.}} = 324.2$ MeV for the tip orientation of the ^{198}Pt nucleus. The table was taken from Ref. [1] 22

Table 3.2 Results of the SMF calculations for the ^{48}Ca + ^{244}Pu system at $E_{\text{c.m.}} = 203.2$ MeV in tip configuration of ^{244}Pu nucleus and the ^{86}Kr + ^{198}Pt system at $E_{\text{c.m.}} = 324.2$ MeV in tip configuration of ^{198}Pt nucleus. The table was taken from Ref. [1]. 27

Table 4.1 Results of the TDHF and SMF calculations for the ^{250}Cf + ^{232}Th system at $E_{\text{c.m.}} = 950.0$ MeV in tip-tip (XX), and tip-side (XY) geometries. 35

Table 4.2 Results of the TDHF calculations for the ^{250}Cf + ^{232}Th system at $E_{\text{c.m.}} = 950.0$ MeV in side-tip (YX), and side-side (YY) geometries. The table was taken from Ref. [1]. 36

Table 4.3 Results of the SMF calculations for the ^{250}Cf + ^{232}Th system at $E_{\text{c.m.}} = 950$ MeV in tip-tip (XX), tip-side (XY), side-tip (YX), and side-side (YY) geometries. 45

LIST OF FIGURES

FIGURES

Figure 1.1 The list of known isotopes from 1935, 1958, and 2015. The figure was taken from Ref. [2]. 2

Figure 1.2 Different stages and processes in low-energy heavy-ion reactions. Deep inelastic collision (I), quasifission (II), fast-fission (III), fusion-fission (IV), and evaporation residue formation (V) are shown. The figure was taken from Ref. [3]. 3

Figure 2.1 Geometry of di-nuclear complex in a collision with beam direction along x axis at a finite impact parameter. The green solid line indicates the symmetry axis, and the red dashed line in the reaction plane indicates the window plane. The figure was taken from Ref. [4]. . 9

Figure 2.2 Typical drift path in $(N - Z)$ plane. (N_0, Z_0) and (N_1, Z_1) represent the local equilibrium state and TLF or PLF, respectively. The dashed thick line represents the iso-scalar line. R_S and R_V represent the iso-vector and iso-scalar distances, respectively. The figure was taken from Ref. [4]. 14

Figure 3.1 Mass-energy distributions of primary fragments at energies near the Bass barrier that was achieved in the reactions$^{48}\mathrm{Ca} + {}^{244}\mathrm{Pu}$ and $^{86}\mathrm{Kr} + {}^{198}\mathrm{Pt}$. The experimental filter gates, which are represented by red rectangles, are used for selecting fissionlike events. The figure was taken from Refs. [5, 6] 20

Figure 3.2 Average numbers of change in neutron and proton numbers in ^{48}Ca + ^{244}Pu system at $E_{\text{c.m.}} = 203.2$ MeV and ^{86}Kr + ^{198}Pt system at $E_{\text{c.m.}} = 324.2$ MeV for the tip orientation of the target-like nuclei are shown as a function of initial angular momentum ℓ_i [1]. 23

Figure 3.3 Mean values of neutron and proton numbers of target-like fragments at initial angular momentum $\ell_i = 40\hbar$ for ^{48}Ca + ^{244}Pu system at $E_{\text{c.m.}} = 203.2$ MeV and $\ell_i = 60\hbar$ for ^{86}Kr + ^{198}Pt system at $E_{\text{c.m.}} = 324.2$ MeV are shown as a function of time. Solid blue lines denote the neutron numbers, and dashed red lines denote the proton numbers of target-like fragments. The labels t_A, t_B, and t_C indicate the projection of the time intervals used to determine the curvature parameters. The figure was taken from Ref. [1]. 24

Figure 3.4 Mean drift path in the $N - Z$ plane for the target-like fragments are given at initial angular momentum $\ell_i = 40\hbar$ for ^{48}Ca + ^{244}Pu system at $E_{\text{c.m.}} = 203.2$ MeV and $\ell_i = 60\hbar$ for ^{86}Kr + ^{198}Pt system at $E_{\text{c.m.}} = 324.2$ MeV. Solid blue lines denote the mean drift path and dashed black lines denote the iso-scalar lines. The labels A, B, and C indicate the projection of the time intervals used to determine the curvature parameters. The figure was taken from Ref. [1]. 25

Figure 3.5 Diffusion coefficient for neutron and proton transfers at initial angular momentum $\ell = 40\hbar$ for ^{48}Ca + ^{244}Pu system at $E_{\text{c.m.}} = 203.2$ MeV, and $\ell = 60\hbar$ for ^{86}Kr + ^{198}Pt system at $E_{\text{c.m.}} = 324.2$ MeV are shown as a function of time. Solid blue lines denote the diffusion coefficients of neutron transfer, $D_{NN}(t)$; dashed red lines denote the diffusion coefficients of proton transfer, $D_{ZZ}(t)$. The figure was taken from Ref. [1]. 26

Figure 3.6 Neutron, proton, and mixed variances as a function of time in ^{48}Ca+^{244}Pu system and ^{86}Kr+^{198}Pt system. Solid blue, dashed red, and dotted green lines denote the neutron variances, σ_{NN}; proton variances, σ_{ZZ}; and the mixed variances, σ_{NZ}, respectively. The figure was taken from Ref. [1]. 27

Figure 3.7 Mass-energy distributions of fragments obtained by the TDHF calculations for the ^{48}Ca + ^{244}Pu system at $E_{\text{c.m.}} = 203.2$ MeV and ^{86}Kr + ^{198}Pt system at $E_{\text{c.m.}} = 324.2$ MeV in tip orientation of target-like nucleus. The red continuous contours represent the gates used in the experiments in Refs. [6, 5, 7] to exclude or reduce the contributions from the elastic events. The figure was taken from Ref. [1]. 29

Figure 3.8 Primary fragment yield in the ^{48}Ca + ^{244}Pu system at $E_{\text{c.m.}} = 203.2$ MeV and ^{86}Kr + ^{198}Pt system at $E_{\text{c.m.}} = 324.2$ MeV in tip orientation of target-like nucleus. The experimental data obtained from Refs. [7, 6] are indicated by the closed black circles. Dashed blue lines indicate the primary product mass distributions calculated within the SMF framework. The FF fragment distribution indicated by the green filled area was calculated using the GEMINI++ code [8]. Solid red lines indicate the summation of yield distribution calculated by the SMF approach and GEMINI++. The figure was taken from Ref. [1]. . . 30

Figure 4.1 Average numbers of change in neutron and proton numbers as a function of initial angular momentum ℓ_i in ^{250}Cf + ^{232}Th system at $E_{\text{c.m.}} = 950.0$ MeV in tip-tip (XX), tip-side (XY), side-tip (YX), and side-side (YY) collision geometries. 34

Figure 4.2 Mean values of neutron and proton numbers of Cf-like fragments at initial angular momentum $\ell_i = 0\hbar$ for ^{250}Cf + ^{232}Th system at $E_{\text{c.m.}} = 950.0$ MeV in tip-tip (XX), tip-side (XY), side-tip (YX), and side-side (YY) are shown as a function of time. Solid blue lines denote the neutron numbers, and dashed red lines denote the proton numbers of Cf-like fragments during the collision. The labels t_A, t_B, and t_C indicate the projection of the time intervals used to determine the averaged value of iso-scalar reduced curvature parameter, $\overline{\beta}$. The figure was taken from Ref. [9]. 38

Figure 4.3 Mean drift path in the $N-Z$ plane for the target-like fragments are given at initial angular momentum $\ell_i = 0\hbar$ for ^{250}Cf$+^{232}$Th system at $E_{\text{c.m.}} = 950.0$ MeV [9]. Solid blue lines denote the mean drift path and thick black lines denote the iso-scalar lines. The labels A, B, and C indicate the projection of the time intervals used to determine the averaged value of the reduced iso-scalar curvature parameter, $\overline{\beta}$. The figure was taken from Ref. [9]. 39

Figure 4.4 Diffusion coefficient for neutron and proton transfers at initial angular momentum $\ell = 0\hbar$ for ^{250}Cf $+$ ^{232}Th system at $E_{\text{c.m.}} = 950.0$ MeV are shown as a function of time. Solid blue lines denote the diffusion coefficients of neutron transfer, $D_{NN}(t)$; dashed red lines denote the diffusion coefficients of proton transfer, $D_{ZZ}(t)$. The figure was taken from Ref. [9]. 40

Figure 4.5 Same as Fig. 4.2 but for the ^{240}Cf $+$ ^{246}Th system.The labels t_A and t_B indicate the projection of the time intervals used to determine the parameter $\overline{\alpha}$. The figure was taken from Ref. [9]. 41

Figure 4.6 Same as Fig. 4.3 but for the ^{240}Cf $+$ ^{246}Th system. The labels A and B indicate the projection of the time intervals used to determine the parameter $\overline{\alpha}$. The figure was taken from Ref. [9]. 42

Figure 4.7 Same as Fig. 4.4 but for the ^{240}Cf $+$ ^{246}Th system. The figure was taken from Ref. [9]. 43

Figure 4.8 Neutron, proton, and mixed variances as a function of time for ^{250}Cf $+$ ^{232}Th system at $E_{\text{c.m.}} = 950.0$ MeV in tip-tip (XX), tip-side (XY), side-tip (YX), and side-side (YY) geometries. Solid blue, dashed red, and dotted green lines denote the neutron, σ_{NN}, proton, σ_{ZZ}, and mixed variances, σ_{NZ}, respectively. The figure was taken from Ref. [9]. 44

Figure 4.9 Primary isotope cross section in $(N-Z)$ plane for ^{250}Cf + ^{232}Th system at $E_{\text{c.m.}} = 950.0$ MeV in tip-tip (XX), tip-side (XY), side-tip (YX), and side-side (YY) geometries. The figure was taken from Ref. [9]. 46

Figure 4.10 Same as Fig. 4.9 but the initial angular momentum range in Eq. 2.32 is decided with the constraints given in the text. 48

Figure 4.11 Secondary isotope cross section in $(N-Z)$ plane for ^{250}Cf + ^{232}Th system at $E_{\text{c.m.}} = 950.0$ MeV in tip-tip (XX), tip-side (XY), side-tip (YX), and side-side (YY) geometries. The figure was taken from Ref. [9]. 49

Figure 4.12 Enlarged view of secondary isotope cross section in $(N-Z)$ plane for ^{250}Cf + ^{232}Th system at $E_{\text{c.m.}} = 950.0$ MeV in tip-tip (XX), tip-side (XY), side-tip (YX), and side-side (YY) geometries. The figure was taken from Ref. [9]. 50

Figure 4.13 Same as Fig. 4.12 but the initial angular momentum range in Eq. 2.40 is decided with the constraints given in the text. 51

LIST OF ABBREVIATIONS

2D	2 Dimensional
3D	3 Dimensional
SMF	Stochastic Mean-field
TDHF	Time-Dependent Hartree Fock
PLF	Projectile-like Fragment
TLF	Target-like Fragment
COM	Center of Mass
QF	Quasi-fission
FF	Fusion-fission
MNT	Multinucleon Transfer
TDRPA	Time-Dependent Random Phase Approximation

CHAPTER 1

INTRODUCTION

It has been more than 100 years since the finding of an atomic nucleus by Rutherford in 1911 [10], which he then followed by performing the first artificial nuclear reaction in 1919. Since then, both theoretical and experimental studies have been developed extensively to produce new isotopes and to understand the nuclear force, types of nuclear reactions, and properties of the nucleus. Fig. 1.1 shows the chart of known nuclides, also known as the Segré chart, from the years 1935, 1958, and 2015. Giorgio Fea published the first list of known nuclides in 1935 [11]. The list was organized into two dimensions based on the number of protons and neutrons of each nuclide. Initially, it had 327 isotopes ranging in elemental composition from uranium to hydrogen, most of which were stable or around the stability line. The discovery of novel reaction types served as the foundation for the massive increase in the number of new isotopes, by more than a factor of ten, during the next 85 years [2]. Nowadays, the number of known isotopes has reached up to 4000, but theoretical models suggest that over 4000 more isotopes [12, 13, 2] remain undiscovered. Most of these yet-unknown-isotopes remain on the *northeast* (neutron-rich) side of the chart, and on the *far northeast* superheavy side, around the predicted "island of stability" near the neutron shell at $N = 184$ and proton shells at $Z = 114, 120$ [14, 15, 16, 17, 18]. Presently, the most compelling reactions to produce isotopes experimentally are fragmentation, fusion, and fission [2]. The production of superheavy elements has thus far resulted from either hot [19, 20, 21, 22, 23, 24, 25, 26, 27] or cold fusion [28, 29, 30, 31, 32] processes, in which the secondary fission and neutron emission play a significant role in de-excitation of the highly excited compound nuclei [1]. Despite the considerable efforts to create new neutron-rich yet unknown isotopes or neutron-rich superheavy elements, these isotopes' comparatively small cross-sections continue to

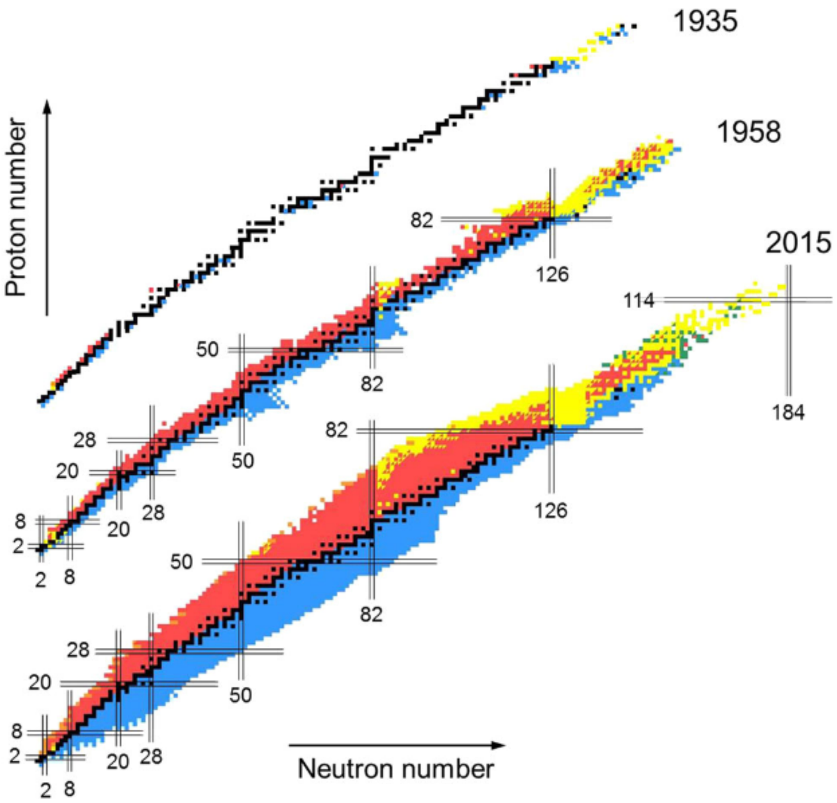

Figure 1.1: The list of known isotopes from 1935, 1958, and 2015. The figure was taken from Ref. [2].

represent a barrier in heavy-ion experiments. As an additional method for producing new, neutron-rich nuclei, the Multinucleon Transfer (MNT) reactions in heavy-ion collisions have been a promising approach since the late 1960s [2]. Between the years 1970-1995, 76 new isotopes of elements ranging from carbon to thorium were found in MNT reactions at experimental facilities, JINR, Orsay, Berkeley, and GSI, and these new isotopes are all found on the nuclide chart's neutron-rich side [33]. During the past few years, recent theoretical calculations suggest that MNT reactions may provide a more efficient method for the production of unstable nuclei such as neutron-rich superheavy isotopes and yet-unknown-neutron-rich isotopes, whose production is complex by fusion, fission, and fragmentation methods. To this end, a great deal of both experimental [34, 35, 36, 37, 38, 39, 40, 41, 42, 43, 44, 45, 46, 47, 5, 48, 49, 50, 51, 52, 53, 54, 55, 56, 57, 58], and theoretical [59, 60, 61, 62, 63, 64, 65, 66, 67, 68,

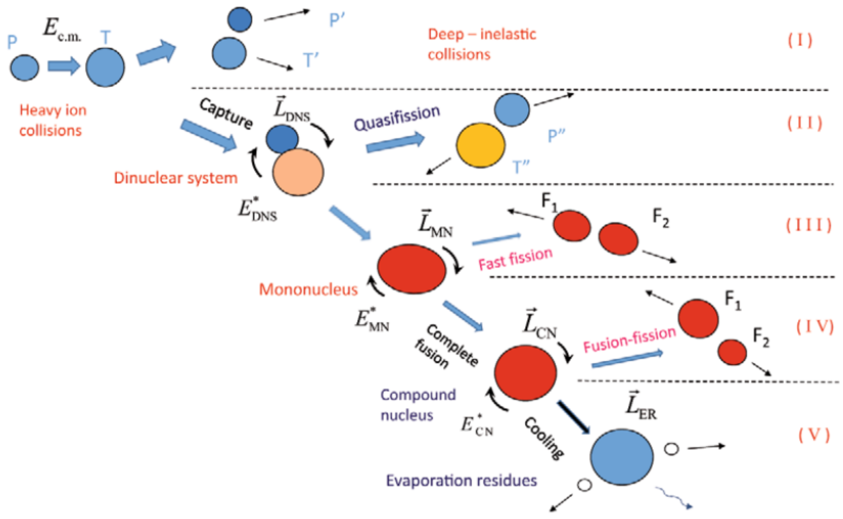
P
$E_{\mathrm{c.m.}}$
T
P′
T′
Deep – inelastic collisions
(I)
Heavy ion collisions
Capture
$\vec{L}_{\mathrm{DNS}}$
Quasifission
P″
T″
(II)
Dinuclear system
E^*_{DNS}
F1
F2
$\vec{L}_{\mathrm{MN}}$
Fast fission
(III)
Mononucleus
E^*_{MN}
Complete fusion
$\vec{L}_{\mathrm{CN}}$
Fusion-fission
F1
F2
(IV)
Compound nucleus
E^*_{CN}
Cooling
$\vec{L}_{\mathrm{ER}}$
(V)
Evaporation residues

Figure 1.2: Different stages and processes in low-energy heavy-ion reactions. Deep inelastic collision (I), quasifission (II), fast-fission (III), fusion-fission (IV), and evaporation residue formation (V) are shown. The figure was taken from Ref. [3].

69, 70, 71, 72, 73, 74, 75, 76, 77, 78, 79, 80, 81, 82, 83, 84, 85, 86, 87, 88, 89, 90] research has been done on MNT reactions involving different projectile and target combinations close to barrier energies.

In MNT reactions involving heavy nuclei, if the initial energy $E_{\mathrm{c.m.}}$ of the projectile fragment is sufficiently large enough to overcome the Coulomb repulsion, the colliding ions stick together due to attractive nuclear force to form a di-nuclear system (see Fig. 1.2 for reference). During this period, the di-nuclear system can either undergo a fast separation called the Quasifission (QF) or fuse to form a compound nucleus (CN). The hot, excited CN then de-excites by fission, called fusion-fission (FF), or de-excites by evaporating light particles, such as neutron, proton, and alpha particles, until it forms an evaporation residue (ER). In QF reactions, many nucleons are transferred between the colliding ions, usually from a heavier partner to a lighter partner, during the collision. So, QF reactions favor the mass symmetric fragments in the exit channel. However, it has been experimentally observed that nucleon transfer from lighter to heavier ions is also possible [47, 91, 92]. This type of reaction is called the Inverse Quasifission (IQF). This type of reaction is essential for synthesizing yet-unknown-neutron-rich heavy isotopes and neutron-rich superheavy elements. In MNT reactions, it has been observed that different entrance channel properties such as N/Z ratio [93, 94], the presence of entrance-channel magicity (the number of spherical shells in the reaction entrance channel) [52], relative orientation of deformed ions [95, 96, 97, 98, 99, 70, 72, 80, 100, 101, 102], and the charge product Z_pZ_t [103, 104, 105, 7, 106] have a significant effect on the reaction outcome. Exploring the interplaying mechanisms behind MNT reactions requires a comprehensive theoretical framework that can adequately account for these intricate processes. To study MNT reactions theoretically, several phenomenological approaches have been employed over the years, such as multidimensional Langevin model [107, 108, 63, 65, 109, 80, 81], the so-called dinuclear system (DNS) model [110, 111, 112], quantum molecular dynamics model [110, 113, 114]. Also, GRAZING [115, 116] model and its extensions with fission mechanism included, GRAZING-F [117] or GRAZING plus GEMINI++ model [118] stand as semiclassical approaches in MNT reactions. The previously mentioned approaches have been thoroughly studied and implemented but depend primarily on phenomenology.

To provide a more accurate description of collision dynamics and the MNT mechanism, it is crucial to develop microscopic approaches, which also provide a test for phenomenological models [9]. The time-dependent Hartree-Fock (TDHF) theory provides a microscopic description of reaction dynamics and it has been employed extensively to analyze MNT reactions [119, 120, 121, 94, 122, 123, 124, 125, 126, 119, 70, 71] (see Refs. [127, 128, 129, 130] for recent reviews of TDHF applications to heavy-ion reactions). In TDHF theory, it is possible to calculate the physical dynamical observables, such as the mean values of the fragment charge and mass and the mean kinetic energy depletion arising from one-body dissipation [131]. To extract the probability of primary fragment production, Simenel [119] suggested the particle-number projection (PNP) method has been used to study MNT reactions. Applicability of this method has been tested over the years [119, 70, 71, 68, 132, 70, 72, 133, 134, 135, 136, 137]. It should be noted that the particle-number projection approach is only a way for obtaining transfer probabilities from the TDHF wave function after collision [73]. It does not extend beyond TDHF. Although the TDHF theory has shown that it is a strong candidate for exploring MNT reactions, it cannot account for fluctuations and dispersions of the fragment mass and charge distributions. To remedy this problem, one must go beyond TDHF [138, 139, 140, 141]. The time-dependent random phase approximation (TDRPA) of Balian and Vénéroni provides an essential improvement of the mean-field description. This approach has been applied to analyze multinucleon transfer in several studies [142, 143, 144, 145, 146, 147]. However, the approach is limited to calculating dispersions of charge and mass distributions in symmetric collisions.

In the present work, we analyze the MNT reactions within an alternative extension to the mean-field approximation, the stochastic mean-field (SMF) theory, which Ayik first proposed in 2008 [148]. The SMF theory goes beyond the TDHF method by including mean-field fluctuations and correlations in the description. Over the last decade, there have been rapid developments and improvements in the description and various MNT reactions are analyzed within the framework of SMF approach [149, 150, 151, 152, 153, 154, 155, 74, 75, 76, 77, 156, 9, 157, 4, 1, 158]. We note here that the SMF approach is not limited to MNT reactions. It has been used in numerous circumstances, including nuclear fission [159], symmetry breaking [160], spinodal instabilities of nuclear matter [161, 162, 163, 164, 165, 166, 167], and Fermionic Hubbard clusters [141].

This thesis is organized as follows. In Chapter 2, our method, the quantal diffusion approach based on the SMF approach, is briefly explained. In Chapter 3, we analyze the QF and FF in the $^{48}\mathrm{Ca} + ^{244}\mathrm{Pu}$ and $^{86}\mathrm{Kr} + ^{198}\mathrm{Pt}$ reactions above the Bass barrier [1], and compare our results with the available experimental data [7, 6]. In Chapter 4, we analyze the primary and secondary isotope production in $^{250}\mathrm{Cf} + ^{232}\mathrm{Th}$ reaction [9] at four different relation orientations. Finally, in Chapter 5, conclusions are given.

CHAPTER 2

QUANTAL TRANSPORT APPROACH BASED ON SMF THEORY

In this Chapter, we present the theoretical framework of the quantal diffusion approach based on SMF theory [148], which will be used to analyze the QF processes in heavy-ion collisions.

In the TDHF method, a single Slater determinant computes a single-particle density matrix given a set of starting conditions. To go beyond this restriction, Ayik suggested [148] to define an ensemble of single-particle matrices that are described in terms of fluctuations in the density matrix at the beginning of time to explain the collision dynamics,

$$\rho_\alpha^\lambda(\vec{r},t) = \sum_{ij\in\alpha} \Phi_j^{*\alpha}(\vec{r},t;\lambda)\rho_{ji}^\lambda \Phi_i^\alpha(\vec{r},t;\lambda) \ , \tag{2.1}$$

where λ denotes each stochastically-generated event, and the notation $\alpha = n, p$ is used for the neutron and proton labels. This ensemble is considered to be generated by incorporating the quantal and thermal fluctuations in the initial state. The initial density matrix's elements p_{ji}^λ in Eq. 2.1, should obey the following conditions according to the main postulate of the SMF theory [148],

$$\overline{\delta\rho_{ij}^\lambda \delta\rho_{kl}^\lambda} = \frac{1}{2}\left[n_i(1-n_j) + n_j(1-n_i)\right]\delta_{kj}\delta_{li}, \tag{2.2}$$

$$\overline{\rho_{ji}^\lambda} = \delta_{ji} n_{ji}, \tag{2.3}$$

where n_i denotes the average occupation numbers of the single-particle states at the initial state. At zero initial temperature, corresponding to the ground state of both PLF and TLF before the collision, the average occupation numbers are either zero or one. In Eqs.(2.2,-2.3) and the rest of this work, the bar over quantities denotes the average over the stochastically-generated ensemble.

In each stochastically generated event, the complete set of single-particle wave functions is determined by the TDHF equations with the self-consistent mean-field Hamiltonian of that event,

$$i\hbar\frac{\partial}{\partial t}\Phi_i(\vec{r},t;\lambda) = h[\rho^\lambda]\Phi_i(\vec{r},t;\lambda). \tag{2.4}$$

In Eq. 2.4, the spin and iso-spin indices are omitted for the sake of simplicity.

The remainder of Chapter 2 is organized as follows. The Langevin equation for macroscopic variables is shared in the following Sec. 2.1. The quantal diffusion coefficients are shared in Sec. 2.2. In Sec. 2.3, covariances of fragment charge and mass distributions are shared. Finally, in Sec. 2.4, primary and secondary product distribution of the reaction products are shared.

2.1 Langevin equation for nucleon transfer

This work considers low-energy collisions at which a di-nuclear structure is maintained during the collision. The identity of colliding nuclei is kept to a large extent, but nucleon transfer takes place between the PLF and the TLF through the window plane. In such a case, one does not need to generate an ensemble of stochastically generated mean-field events, and it is possible to develop a much easier transport description with the help of a window plane and geometric projection. We refer to Refs. [74, 75, 152, 76, 73, 156, 131] for detailed information on the window dynamics and the quantal diffusion description. (see also the supplementary online material [4]). To describe the quantal nucleon transfer mechanism, the relevant macroscopic variables are chosen as the neutron and the proton numbers of the PLF or TLF. This allows us to treat the nucleon transfer as a diffusion process [168]. In this work, the relevant macroscopic variables are the neutron number N_1^λ and the proton number Z_1^λ of the TLF. The geometry of the di-nuclear complex in a generic QF reaction involving heavy-ions is shown in Fig. 2.1. A solid green line denotes the symmetry axis, and its position can be found by diagonalizing the mass quadrupole matrix as described in detail in Refs. [151, 75]. The window plane, which is denoted by the

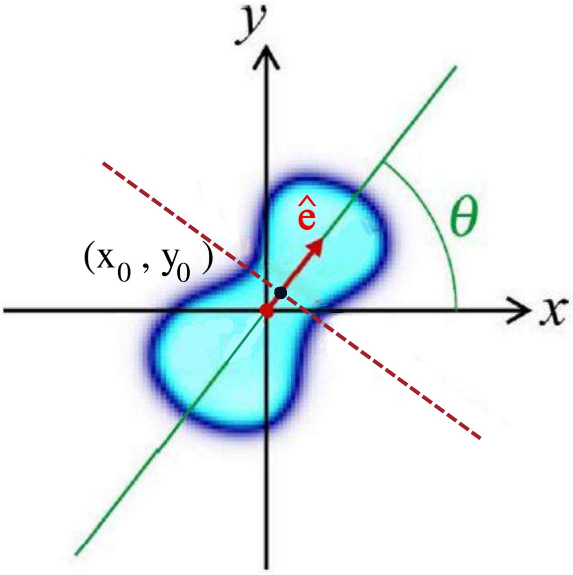

Figure 2.1: Geometry of di-nuclear complex in a collision with beam direction along x axis at a finite impact parameter. The green solid line indicates the symmetry axis, and the red dashed line in the reaction plane indicates the window plane. The figure was taken from Ref. [4].

dashed red line, is perpendicular to the symmetry axis with its center $(x_0(t), y_0(t))$ situated between the colliding ions in the neck's center of the minimum density slice. $\hat{\boldsymbol{e}}$ is the unit vector perpendicular to the window plane which is directed from the center of the PLF to the center of TLF with $\hat{\boldsymbol{e}}(t) = \cos\theta(t)\hat{\boldsymbol{x}} + \sin\theta(t)\hat{\boldsymbol{y}}$. Here, $\theta(t)$ is the smaller angle between the symmetry axis and the beam direction, $x-$axis. Throughout this section, calculations are performed for a specific impact parameter, b, or initial orbital angular momentum, ℓ. However, we do not label the quantities with the impact parameter or angular momentum.

By integrating the nucleon density over the window's TLF side between the colliding nuclei, the neutron and proton counts in each event with the label λ can be determined, and the quantal Langevin equations for macro variables becomes [4],

$$\frac{d}{dt}\begin{pmatrix} N_1^\lambda(t) \\ Z_1^\lambda(t) \end{pmatrix} = \int g\left(x'\right)\begin{pmatrix} \hat{\boldsymbol{e}}\cdot\vec{j}_n^\lambda(\vec{r},t) \\ \hat{\boldsymbol{e}}\cdot\vec{j}_p^\lambda(\vec{r},t) \end{pmatrix} d\vec{r} = \begin{pmatrix} v_n^\lambda(t) \\ v_p^\lambda(t) \end{pmatrix}, \tag{2.5}$$

where the Gaussian function, $g(x') = [1/(\kappa\sqrt{2\pi})]\exp[-x'^2/2\kappa^2]$ is the smoothing function with dispersion κ, extracting the contribution near the window. In the numerical calculations, the value of dispersion is taken as $\kappa = 1.0$ fm, which is in the same order of lattice spacing. In Eq. 2.5, $\vec{j}^{\lambda}_{\alpha}$ is the current density given by,

$$\vec{j}^{\lambda}_{\alpha}(\vec{r},t) = \frac{\hbar}{m}\sum_{ij\in\alpha} \mathrm{Im}\left(\Phi^{*\alpha}_{j}(\vec{r},t;\lambda)\vec{\nabla}\Phi^{\alpha}_{i}(\vec{r},t;\lambda)\rho^{\lambda}_{ji}\right) \ . \tag{2.6}$$

In this work, the linear form of Eq. 2.5 is used with the assumption of small fluctuations around the mean values of macroscopic variables [157],

$$\frac{d}{dt}\begin{pmatrix} \delta N^{\lambda}_{1} \\ \delta Z^{\lambda}_{1} \end{pmatrix} = \begin{pmatrix} \frac{\partial v_n}{\partial Z_1}\delta Z^{\lambda}_{1} + \frac{\partial v_n}{\partial N_1}\delta N^{\lambda}_{1} \\ \frac{\partial v_p}{\partial Z_1}\delta Z^{\lambda}_{1} + \frac{\partial v_p}{\partial N_1}\delta N^{\lambda}_{1} \end{pmatrix} + \begin{pmatrix} \delta v^{\lambda}_{n}(t) \\ \delta v^{\lambda}_{p}(t) \end{pmatrix} \ . \tag{2.7}$$

Here, $\delta N^{\lambda}_{1} = N^{\lambda}_{1} - \overline{N^{\lambda}_{1}}$ and $\delta Z^{\lambda}_{1} = Z^{\lambda}_{1} - \overline{Z^{\lambda}_{1}}$ stands for the stochastic part of the macroscopic variables with the mean values $\overline{N^{\lambda}_{1}} = N_1$ and $\overline{Z^{\lambda}_{1}} = Z_1$ which calculated entirely within the mean-field potential of the TDHF framework. Similarly, $\delta v^{\lambda}_{n} = v^{\lambda}_{n} - \overline{v^{\lambda}_{n}}$ and $\delta v^{\lambda}_{p} = v^{\lambda}_{p} - \overline{v^{\lambda}_{p}}$ stands for the stochastic parts of the drift coefficients with $\overline{v^{\lambda}_{n}} = v_n$ and $\overline{v^{\lambda}_{p}} = v_p$, respectively.

In order to calculate the neutron dispersion $\sigma^2_{NN}(\ell,t) = \overline{\delta N^{\lambda}_{1}\delta N^{\lambda}_{1}}$, proton dispersion $\sigma^2_{ZZ}(\ell,t) = \overline{\delta Z^{\lambda}_{1}\delta Z^{\lambda}_{1}}$, and the mixed dispersion $\sigma^2_{NZ}(\ell,t) = \overline{\delta N^{\lambda}_{1}\delta Z^{\lambda}_{1}}$, one can multiply both side of the Eq. 2.7 by δN^{λ}_{1} and δZ^{λ}_{1}, and take the ensemble average, resulting in a set of coupled partial differential equations,

$$\frac{\partial}{\partial t}\sigma^2_{NN} = 2\frac{\partial v_n}{\partial N_1}\sigma^2_{NN} + 2\frac{\partial v_n}{\partial Z_1}\sigma^2_{NZ} + 2D_{NN}, \tag{2.8}$$

$$\frac{\partial}{\partial t}\sigma^2_{ZZ} = 2\frac{\partial v_p}{\partial Z_1}\sigma^2_{ZZ} + 2\frac{\partial v_p}{\partial N_1}\sigma^2_{NZ} + 2D_{ZZ}, \tag{2.9}$$

and

$$\frac{\partial}{\partial t}\sigma^2_{NZ} = \frac{\partial v_p}{\partial N_1}\sigma^2_{NN} + \frac{\partial v_n}{\partial Z_1}\sigma^2_{ZZ} + \sigma^2_{NZ}\left(\frac{\partial v_p}{\partial Z_1} + \frac{\partial v_n}{\partial N_1}\right), \tag{2.10}$$

with the initial conditions $\sigma^2_{NN}(\ell, t = 0) = 0, \sigma^2_{ZZ}(\ell, t = 0) = 0$, and $\sigma^2_{NZ}(\ell, t = 0) = 0$, since at initial time particle number is not fluctuating. The set of coupled equations is also familiar from the phenomenological nucleon exchange model, and they were derived from the Fokker-Planck equation for the fragment neutron and proton distributions in the deep-inelastic heavy-ion collisions [169, 170, 79]. In this set of equations, D_{NN} and D_{ZZ} are the neutron and proton diffusion coefficients, respectively, which will be explained in the following section, Sec. 2.2.

2.2 Quantal diffusion coefficients

The quantal diffusion coefficients are related to the auto-correlation function of the stochastic part of the drift coefficients [171, 172],

$$D_{\alpha\alpha}(t) = \int_0^t dt' \overline{\delta v_\alpha^\lambda(t) \delta v_\alpha^\lambda(t')}, \tag{2.11}$$

where the stochastic part of the drift coefficients $\delta v_\alpha^\lambda(t)$ given by,

$$\delta v_\alpha^\lambda(t) = \frac{\hbar}{m} \sum_{ij\in\alpha} \int d^3r g\,(x')\, \hat{\boldsymbol{e}} \cdot \mathrm{Im}\left[\Phi_j^{*\alpha}(\vec{r}, t; \lambda) \vec{\nabla} \Phi_i^\alpha(\vec{r}, t; \lambda) \delta\rho_{ji}^\lambda\right]. \tag{2.12}$$

To calculate the Eq. 2.12, one needs to sum over the complete set of particle and hole states indicated by the indices i and j. By employing closure relations in the diabatic limit and using the main postulate of SMF theory (given in Eq. 2.2), it is possible to eliminate the unoccupied states and calculate the diffusion coefficients only in terms of occupied states of the THDF evolution (the detailed derivation of the quantal diffusion coefficients in central and off-central collisions are given in the Refs. [155, 75]),

$$\begin{aligned} D_{\alpha\alpha}(t) = {} & \int_0^t d\tau \int d^3r \tilde{g}\,(x') \big(G_T(\tau) J_{\perp,\alpha}^T(\vec{r}, t-\tau/2) \\ & + G_P(\tau) J_{\perp,\alpha}^P(\vec{r}, t-\tau/2)\big) - \int_0^t d\tau\, \mathrm{Re}\Bigg(\sum_{h'\in P, h\in T} A_{h'h}^\alpha(t) A_{h'h}^{*\alpha}(t-\tau) \\ & + \sum_{h'\in T, h\in P} A_{h'h}^\alpha(t) A_{h'h}^{*\alpha}(t-\tau)\Bigg), \end{aligned} \tag{2.13}$$

here, $\tilde{g}(x') = [1/(\kappa'\sqrt{\pi})]\mathrm{exp}[-x'^2/2\kappa'^2]$ is another smoothing function with $\kappa' = 0.5$ fm and the memory kernels $G_T(\tau)$ are given by,

$$G_T(\tau) = \frac{1}{\sqrt{4\pi}} \frac{1}{\tau_0} \mathrm{exp}\left[-(\tau/2\tau_0)^2\right]. \tag{2.14}$$

The average flow speed u_0 of the target nucleons across the window gives the memory time as $\tau_0 = \kappa'/|u_0|$. $G_P(\tau)$ is given by a similar expression. The magnitude of current densities perpendicular to the window plane is represented by $J_{\perp,\alpha}^\mu(\vec{r}, t)$ in

Eq. 2.13, where contributions come from hole wave functions emanating from the target (μ =T) or projectile (μ =P),

$$J^{\mu}_{\perp,\alpha}(\vec{r},t) = \frac{\hbar}{m}\sum_{h\in\mu}\left|\hat{\boldsymbol{e}}\cdot \mathrm{Im}\left[\Phi^{*\alpha}_{h}(\vec{r},t)\vec{\nabla}\Phi^{\alpha}_{h}(\vec{r},t)\right]\right| . \tag{2.15}$$

Finally, in Eq. 2.13, the hole-hole matrix elements, $A^{\alpha}_{h'h}(t)$, are given by,

$$A^{\alpha}_{h'h}(t) = \hat{\boldsymbol{e}}\cdot\frac{\hbar}{2m}\int d^3r g\left(x'\right)\left[\Phi^{*}_{h'}(\vec{r},t)\vec{\nabla}\Phi^{\alpha}_{h}(\vec{r},t) - \Phi^{\alpha}_{h}(\vec{r},t)\vec{\nabla}\Phi^{*\alpha}_{h'}(\vec{r},t)\right] . \tag{2.16}$$

In Eq. 2.13, the first term gives the sum of nucleon currents across the projectile-like and target-like subsystems, which are integrated over the memory. This is equivalent to the diffusion coefficient in the random walk problem, which is given by the sum of the rate for the forward and backward steps [171, 172]. Conversely, the second term accounts for the Pauli blocking effect in nucleon transfer processes, a term lacking a classical counterpart. The fluctuations, which are specified with quantal diffusion coefficients, are calculated in terms of mean-field properties, i.e., in terms of only occupied single-particle wave functions of TDHF. This is consistent with the fluctuation-dissipation theorem of non-equilibrium statistical mechanics and significantly reduces computation time. Diffusion coefficients include the quantal effects due to shell structure, Pauli blocking, and the full effect of the collision geometry without any adjustable parameters.

2.3 Potential energy of the di-nuclear system

To solve the coupled partial differential equations, Eqs.(2.8-2.10), one needs to calculate the quantal diffusion coefficients, $D_{\alpha\alpha}$ and the derivatives of the mean drift coefficients with respect to neutron and proton numbers. By using Einstein's relation in the overdamped limit, one can relate the drift coefficients to the derivatives of the potential energy of the colliding system in the $(N-Z)$ plane as,

$$v_n(t) = -\frac{D_{NN}(t)}{T^*}\frac{\partial}{\partial N_1}U(N_1,Z_1) , \tag{2.17a}$$

$$v_z(t) = -\frac{D_{ZZ}(t)}{T^*}\frac{\partial}{\partial Z_1}U(N_1,Z_1) , \tag{2.17b}$$

where T^* is the effective temperature of the system, and $U(N_1, Z_1)$ represents the potential energy of the system as a function of neutron and proton numbers of one of the reaction partners. Within the potential energy surface provided by microscopic Skyrme energy density functional, the surface energy, electrostatic energy, symmetry energy, and centrifugal potential energy are included at a microscopic level. However, this potential energy surface of the di-nuclear system as a function of (N_1, Z_1) is expected to have a complex structure. In this work, we approximate the potential by a two-parabolic form,

$$U(N_1, Z_1) = \frac{1}{2} a R_S^2 + \frac{1}{2} b R_V^2, \tag{2.18}$$

where

$$R_V(t) = [N_1(t) - N_0] \cos\phi + [Z_1(t) - Z_0] \sin\phi \ , \tag{2.19}$$

and

$$R_S(t) = [Z_1(t) - Z_0] \cos\phi - [N_1(t) - N_0] \sin\phi \ . \tag{2.20}$$

Here, (N_0, Z_0) stands for the local equilibrium state of the system, and it is determined accordingly for each system, respectively. R_V is called the iso-scalar distance, and it represents the horizontal distance between the fragment and the local equilibrium state. Similarly, R_S is called the iso-vector distance, and it represents the perpendicular distance between the fragment and the local equilibrium state (see Fig. 2.2 for reference). By substituting Eq. 2.18 to Eqs.(2.17a-2.17b), one can get,

$$v_n(t) = -D_{NN}(t) \left[-\alpha R_S \sin\phi + \beta R_V \cos\phi \right] \ , \tag{2.21a}$$

$$v_z(t) = -D_{ZZ}(t) \left[\alpha R_S \cos\phi + \beta R_V \sin\phi \right] \ . \tag{2.21b}$$

Here, $\alpha = a/T^*$ and $\beta = b/T^*$ denote the reduced curvature parameters. The effective temperature is not a parameter in this description since only ratios of the curvature parameters and the effective temperature occur. By inverting Eqs.(2.21a-2.21b) and solving for the reduced curvature parameters α and β, we get,

$$\alpha(t) = \frac{1}{R_S} \left(\frac{v_n}{D_{NN}} \sin\phi - \frac{v_z}{D_{ZZ}} \cos\phi \right) \tag{2.22}$$

$$\beta(t) = \frac{-1}{R_V} \left(\frac{v_n}{D_{NN}} \cos\phi + \frac{v_z}{D_{ZZ}} \sin\phi \right) \tag{2.23}$$

Due to shell effects and microscopic collision dynamics within the TDHF framework, the curvature parameters exhibit time dependence. To accommodate this in the macroscopic transport description, we must mitigate the temporal fluctuations.

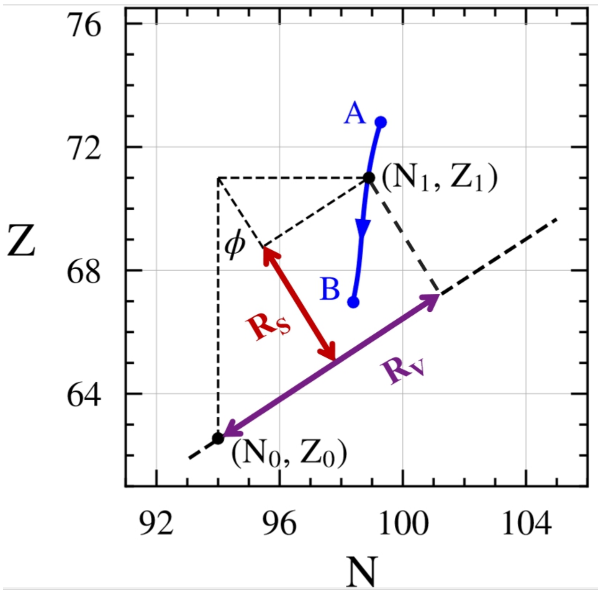

Figure 2.2: Typical drift path in $(N-Z)$ plane. (N_0, Z_0) and (N_1, Z_1) represent the local equilibrium state and TLF or PLF, respectively. The dashed thick line represents the iso-scalar line. R_S and R_V represent the iso-vector and iso-scalar distances, respectively. The figure was taken from Ref. [4].

Thus, we compute the reduced curvature parameters by averaging them over appropriate time intervals while the colliding binary reaction partners overlap sufficiently strongly. Following the drift pattern depicted in Fig. 2.2, the averaged value of the iso-vector reduced curvature parameter between time intervals t_A and t_B is determined as follows:

$$\overline{\alpha} = \frac{1}{\int_{t_A}^{t^B} R_S dt} \int_{t_A}^{t_B} dt \left(\frac{v_n}{D_{NN}} \sin\phi - \frac{v_z}{D_{ZZ}} \cos\phi \right), \tag{2.24}$$

similarly, iso-scalar reduced curvature parameter between time intervals t_A and t_B is determined as,

$$\overline{\beta} = \frac{-1}{\int_{t_A}^{t^B} R_V dt} \int_{t_A}^{t_B} dt \left(\frac{v_n}{D_{NN}} \cos\phi + \frac{v_z}{D_{ZZ}} \sin\phi \right). \tag{2.25}$$

By using the calculated reduced curvature parameters and taking advantage of the analytical form of the potential energy, one can calculate the derivatives of the drift coefficients given in couple partial differential equations(2.8-2.10);

$$\frac{\partial \nu_n}{\partial N_1} = -D_{NN}\left(\alpha \sin^2\phi + \beta \cos^2\phi\right) \ , \tag{2.26}$$
$$\frac{\partial \nu_z}{\partial Z_1} = -D_{ZZ}\left(\alpha \cos^2\phi + \beta \sin^2\phi\right) \ , \tag{2.27}$$
$$\frac{\partial \nu_n}{\partial Z_1} = -D_{NN}\left(\beta - \alpha\right)\sin\phi\cos\phi \ , \tag{2.28}$$
$$\frac{\partial \nu_z}{\partial N_1} = -D_{ZZ}\left(\beta - \alpha\right)\sin\phi\cos\phi \ . \tag{2.29}$$

Together with the calculated quantal diffusion coefficients, the neutron and proton variances and covariances can be determined from the solutions of coupled differential equations (Eqs. 2.8-2.10) with the initial conditions $\sigma_{NN}(t=0)=0$, $\sigma_{ZZ}(t=0)=0$, and $\sigma_{NZ}(t=0)=0$, for each system and angular momentum.

2.4 Primary and Secondary Product Distribution of the Reaction Products

2.4.1 Probability Distributions of Primary Reaction Fragments

For the purpose of creating a binary fragment with neutron N and proton Z numbers, the joint probability distribution function $P_\ell(N,Z)$ is typically found by creating a large number of solutions to Langevin Eq. (2.7). For the distribution function of the macroscopic variables, it is well known that the Langevin Equation is equivalent to the Fokker-Planck equation [172]. In the case when drift coefficients are linear functions of macroscopic variables, as we have in Eq. 2.7, the proton and neutron distribution function for initial angular momentum ℓ is given as a correlated Gaussian function described by the mean values, the neutron, proton, and mixed dispersions as [9],

$$P_\ell(N,Z) = \frac{1}{2\pi\sigma_{NN}(\ell)\sigma_{ZZ}(\ell)\sqrt{1-\rho_\ell^2}}\exp\left(-C_\ell\right) \tag{2.30}$$

Here the exponent C_ℓ for each impact parameter is given by,

$$C_\ell = \frac{1}{2\left(1-\rho_\ell^2\right)}\left[\left(\frac{Z-Z_\ell}{\sigma_{ZZ}(\ell)}\right)^2 + \left(\frac{N-N_\ell}{\sigma_{NN}(\ell)}\right)^2 \right.$$
$$\left. -2\rho\left(\frac{Z-Z_\ell}{\sigma_{ZZ}(\ell)}\right)\left(\frac{N-N_\ell}{\sigma_{NN}(\ell)}\right)\right] \tag{2.31}$$

with the correlation coefficient as $\rho_l = \sigma^2_{NZ}(l)/\left[\sigma_{ZZ}(l)\sigma_{NN}(l)\right]$. The quantities $N_l = \overline{N^\lambda_l}, Z_l = \overline{Z^\lambda_l}$ denote the mean neutron and proton numbers of the target-like or project-like fragments determined by the TDHF calculations.

Production cross-sections of primary isotopes are calculated using the standard expression,

$$\sigma^{\mathrm{S,pri}}(N,Z) = \frac{\pi\hbar^2}{2\mu E_{\mathrm{c.m.}}}\sum_{\ell_{\min}}^{\ell_{\max}}(2l+1)P^{\mathrm{S,pri}}_{\ell}(N,Z) \tag{2.32}$$

with,

$$P^{\mathrm{S,pri}}_{\ell}(N,Z) = \frac{1}{2}\left[P^{\mathrm{S,pri}}_{\ell,\mathrm{pro}}(N,Z) + P^{\mathrm{S,pri}}_{\ell,\mathrm{tar}}(N,Z)\right] \tag{2.33}$$

In these expressions, the label "S" indicates different collision geometries and μ is the reduced mass of the projectile and target nuclei. Quantities $P^{\mathrm{S,pri}}_{\ell,\mathrm{pro}}(N,Z)$ and $P^{\mathrm{S,pri}}_{\ell,\,\mathrm{tar}}(N,Z)$ denotes the normalized probability of producing projectile-like and target-like fragments by using Eq. 2.30. To normalize the total primary fragment distribution to unity, a factor of $1/2$ is introduced. The range of angular momentum in a summation over ℓ depends on the detector's geometry in the laboratory frame and the experimental configuration. In our computations, we sum over the interval $\ell_{\min}$ to $\ell_{\max}$, which is determined separately in each system. If only mass numbers of fragments are identified, double probability in the cross-section expression is replaced by mass number distribution,

$$P^{\mathrm{S,pri}}_{\ell}(A) = \frac{1}{2}\left[P^{\mathrm{S,pri}}_{\ell,\mathrm{pro}}(A) + P^{\mathrm{S,pri}}_{\ell,\mathrm{tar}}(A)\right] \tag{2.34}$$

Summing over N or Z and maintaining the total mass number constant A $= N + Z$ yields the probability distribution of the mass number of the fragments created,

$$P^{\mathrm{S,pri}}_{\ell,\mathrm{pro}}(A) = \frac{1}{\sqrt{2\pi}}\frac{1}{\sigma_{AA}(\ell)}\exp\left[-\frac{1}{2}\left(\frac{A - A_{\ell,\mathrm{pro}}}{\sigma_{AA}(\ell)}\right)^2\right] \tag{2.35}$$

where mass variance is given by $\sigma^2_{AA}(\ell) = \sigma^2_{NN}(\ell) + \sigma^2_{ZZ}(\ell) + 2\sigma^2_{NZ}(\ell)$. Similarly, for target-like fragments, $P^{\mathrm{S,pri}}_{\ell,\mathrm{tar}}(A)$ is given by,

$$P^{\mathrm{S,pri}}_{\ell,\mathrm{tar}}(A) = \frac{1}{\sqrt{2\pi}}\frac{1}{\sigma_{AA}(\ell)}\exp\left[-\frac{1}{2}\left(\frac{A - A_{\ell,\mathrm{tar}}}{\sigma_{AA}(\ell)}\right)^2\right]. \tag{2.36}$$

If the compared experimental results are in arbitrary units, the primary yield distribution is calculated accordingly by the standard expression [173],

$$Y^{\mathrm{S,pri}}(A) = \frac{1}{\sum_{\ell_{\min}}^{\ell_{\max}}(2\ell+1)} \sum_{\ell_{\min}}^{\ell_{\max}}(2\ell+1)P_{\ell}^{\mathrm{S,pri}}(A). \tag{2.37}$$

2.4.2 Probability Distributions of Primary FF Fragments

Using the quantal diffusion approach (Eq. 2.37), we can determine the fragment mass distribution due to the MNT mechanism. But, the primary mass distribution near the mass symmetric region ($\frac{A_{\text{pro}}+A_{\text{tar}}}{2} \pm 20$) usually consists of contributions from both FF and QF mechanisms. The statistical Monte Carlo code GEMINI++ [8] is utilized for this region to analyze the contributions from FF-like events. The validity of this method is tested and confirmed in the Refs. [158, 1, 156]. The excitation energy of the compound nuclei is estimated by, $E^{*}_{\text{CN}} = E_{\text{c.m.}} + Q_{gg}$, where Q_{gg} stands for released disintegration energy in fusion reaction. Combined with contributions from the FF-like events calculated by GEMINI++, total primary fragment mass distribution takes the form

$$Y(A)^{sum} = \left[\eta^{MNT} Y(A)^{\text{S,pri}} + \eta^{FF} Y(A)^{FF}\right] \ , \tag{2.38}$$

where $Y(A)^{FF}$ stands for the probability of reaching fission-fragment with mass number A, after the statistical de-excitation of compound nuclei. In this work, the number of Monte-Carlo simulation times is set to $M_{\text{trial}} = 100\ 000$ in GEMINI++ calculations, which is sufficient to get a statistical distribution for this region. In Eq. (2.38), η^{MNT} and η^{FF} stand for normalizing constants for distributions arising from the MNT reactions and fission reactions, respectively. The value of η^{MNT} is determined by matching the peak values of the experimental yield, and the value of η^{FF} is determined by matching the experimental yield at mass middle point $A = \frac{A_{\text{pro}}+A_{\text{tar}}}{2}$.

2.4.3 Probability Distributions of Secondary Reaction Fragments

Primary fragments are excited and cool down by light particle emission, mostly neutrons, protons, and alpha particles, or they may decay via binary fission. We analyze the de-excitation mechanisms of the primary fragments using the statistical code GEMINI++ [8]. We estimate the total excitation energy of the primary fragments according to $E^*_\ell(N,Z) = E_{\text{c.m.}} - \text{TKE}_\ell + Q_{\text{gg}}(N,Z)$. In this expression, TKE_ℓ denotes the asymptotic value of the total kinetic energy after the collision, and $Q_{\text{gg}}(N,Z)$ denotes ground state Q-value of the primary fragments relative to the initial value [9]. Usually, the total spin and the total excitation energy after the collision should have distributions around their mean values. In the present analysis, we share the mean value of the total excitation energy and the total angular momentum transfer proportionately to the mass ratio of the primary fragments, ignoring the fluctuations around mean values. Until the parent nucleus's disintegration is energetically prohibited, the excited parent nucleus decays through a sequence of light particle evaporations and secondary fission. The statistical code GEMINI++ calculates the probability $W_\ell(N,Z \to N',Z')$ of reaching the final nucleus (N',Z'), starting from an excited parent nucleus with neutron and proton numbers (N,Z), excitation energy $E^*_\ell(N,Z)$, and spin J. Then, the probability distribution of secondary isotopes can be expressed as

$$P_\ell^{\text{S,sec}}(N',Z') = \sum_{N\geq N'}\sum_{Z\geq Z'} P_\ell^{\text{S,pri}}(N,Z) W_\ell(N,Z \to N',Z') \;. \tag{2.39}$$

Here, the summation over (N,Z) covers the pairs of PLF and TLF of the di-nuclear system according to their probability distributions. Combined with the de-excitation process, the expression for the production cross-section of secondary isotopes takes the form,

$$\sigma_\ell^{\text{S,sec}}(N',Z') = \frac{\pi\hbar^2}{2\mu E_{\text{c.m.}}} \sum_{\ell_{\min}}^{\ell_{\max}} (2\ell+1) P_\ell^{\text{sec}}(N',Z') \;. \tag{2.40}$$

CHAPTER 3

QF AND FF IN THE $^{48}\mathrm{Ca} + {}^{244}\mathrm{Pu}$ AND $^{86}\mathrm{Kr} + {}^{198}\mathrm{Pt}$ REACTIONS

In this part of Chapter 3 of the thesis, we extend our calculation to reactions with heavier nuclei. In reactions involving heavy nuclei, although both QF and FF mechanisms take place simultaneously, the expected dominant process is the QF process because of the suppression of the fusion process due to the strong Coulomb repulsion. The primary fragments near the mass symmetric region $(\frac{A_{pro}+A_{tar}}{2} \pm 20)$ are either result of FF or QF processes. Calculations need to consider both mechanisms to explain the primary mass distribution in heavy systems. In this part, we aim to show that SMF theory, combined with GEMINI++, is a promising tool for explaining the reaction mechanism in reactions involving heavy nuclei.

In this Chapter, we investigate the QF and FF processes in the $^{48}\mathrm{Ca} + {}^{244}\mathrm{Pu}$ reaction at $\mathrm{E}_{\mathrm{c.m.}} = 203.2$ MeV and $^{86}\mathrm{Kr} + {}^{198}\mathrm{Pt}$ reaction at $\mathrm{E}_{\mathrm{c.m.}} = 324.2$ MeV. The fusion-evaporation cross-section, fission modes of superheavy compound Flevorium nuclei in the $^{48}\mathrm{Ca} + {}^{244}\mathrm{Pu}$ reaction have been investigated experimentally in Refs. [7, 174, 19, 175], whereas the MNT and QF reaction products and their properties have been investigated experimentally in the Refs. [176, 7, 5]. In Ref. [177], QF and MNT reactions in this system are investigated theoretically within the TDHF framework. In Refs. [5, 7], $^{48}\mathrm{Ca} + {}^{244}\mathrm{Pu}$ system is investigated at $\mathrm{E}_{\mathrm{c.m.}} = 203.2$ MeV, corresponding to the ratio $\mathrm{E}_{\mathrm{c.m.}}/V_{\mathrm{Bass}} = 1.03$, where $V_{\mathrm{Bass}} = 197.29$ MeV [5, 178, 179]. In the subpanel (a) of Fig. 3.1, the mass-energy distributions of primary fragments obtained in the $^{48}\mathrm{Ca} + {}^{244}\mathrm{Pu}$ reaction at energy above the Bass barrier in the experimental work in Ref. [7] are shown. The continuous red contours in Fig. 3.1 are used to exclude the elastic events and select fissionlike events arising from either FF or QF processes. In this experiment, which theoretical calculations in this work will

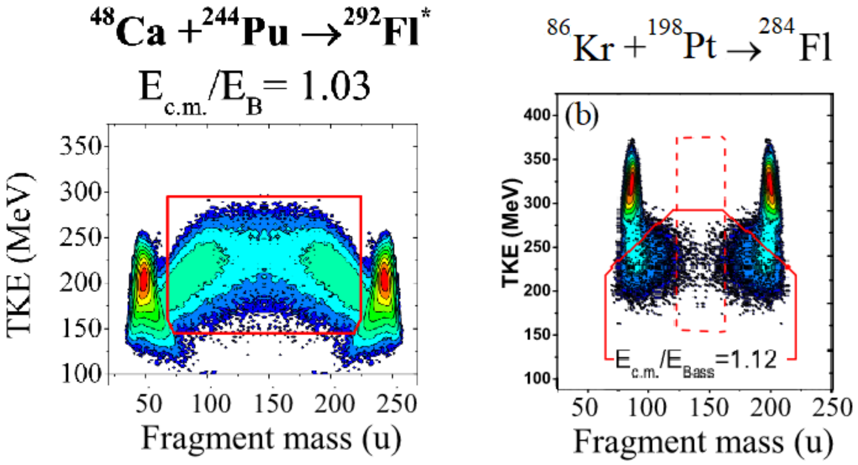

Figure 3.1: Mass-energy distributions of primary fragments at energies near the Bass barrier that was achieved in the reactions$^{48}\mathrm{Ca} + {}^{244}\mathrm{Pu}$ and $^{86}\mathrm{Kr} + {}^{198}\mathrm{Pt}$. The experimental filter gates, which are represented by red rectangles, are used for selecting fissionlike events. The figure was taken from Refs. [5, 6]

be compared with, binary primary fragments are detected between $42° - 78°$ in the laboratory frame. The superheavy element Flevorium can also be synthesized in the $^{86}\mathrm{Kr} + {}^{198}\mathrm{Pt}$ reaction, and it is also investigated experimentally in the Refs. [6, 7] at E$_{\text{c.m.}}$ $= 324.2$ MeV which corresponds to E$_{\text{c.m.}}/V_{\text{Bass}} = 1.12$. In subpanel (b) of Fig. 3.1, the mass-tke distribution of binary primary fragments in $^{86}\mathrm{Kr} + {}^{198}\mathrm{Pt}$ reaction at the above barrier energy is shown [6]. In this experiment, which theoretical calculations in this work will be compared with, the binary primary fragments are detected between $30° - 68°$ in the laboratory frame.

The remainder of this Chapter is organized as follows. In Sec. 3.1, the mean-field results calculated within the TDHF framework are shared and discussed. In Sec. 3.2, the covariances of fragment mass and charge calculated within the SMF framework are shared. Finally, the estimated primary mass distributions are compared with the available experimental data [7, 6].

3.1 Mean Reaction Dynamics in TDHF

3.1.1 Mean values of reaction observables

This computation and all other numerical computation in this section are carried out by employing the three-dimensional TDHF program of Umar et al. [180, 181] using the SLy4d Skyrme energy density functional [182, 183], with a box size of 60 × 60 × 36 fm in the $x-y-z$ directions. TDHF ground state calculations show that both ^{48}Ca and ^{86}Kr nuclei exhibit spherical shapes, whereas ^{244}Pu and ^{198}Pt nuclei exhibit strong prolate and oblate deformations, respectively. For this reason, to consider all possible relative orientations of the deformed nuclei, the TDHF and SMF calculations were performed for all possible relative orientations of the reaction partners. As a convention, we denote the initial orientation of the target principal deformation axis as being in the beam direction as the tip direction and the case when their principal axis is perpendicular to the beam direction as the side direction. To reduce the computation time, quantities are evaluated for every two units of initial angular momentum for ^{48}Ca + ^{244}Pu system, and ten units of initial angular momentum for ^{86}Kr + ^{198}Pt system. In Table 3.1, the TDHF results for ^{48}Ca + ^{244}Pu system at $E_{\text{c.m.}} = 203.2$ MeV for the tip orientation of the ^{244}Pu nucleus and ^{86}Kr + ^{198}Pt system at $E_{\text{c.m.}} = 324.2$ MeV for the tip orientation of the ^{198}Pt nucleus are shown for a range initial orbital angular momenta, ℓ_i, final values of charge and mass numbers of PLF Z_1^f, A_1^f and TLF Z_2^f, A_2^f, final total kinetic energy TKE (in MeV units), contact time t_c(in zs units), the scattering angles in the center of mass frame $\theta_{\text{c.m.}}$, and the laboratory frame θ_1^{lab} and θ_2^{lab}, respectively.

For each collision in the center-of-mass frame, the scattering angles in the laboratory frame, θ_1^{lab} and θ_2^{lab}, are calculated according to[179, 75],

$$\tan\theta_1^{\text{lab}} = \frac{\sin\theta_{\text{c.m.}}}{\sqrt{\frac{A_1^i A_1^f}{A_2^i A_2^f}\frac{E_{\text{c.m.}}}{TKE}} + \cos\theta_{\text{c.m.}}} \tag{3.1}$$

and

$$\tan\theta_2^{\text{lab}} = \frac{\sin\theta_{\text{c.m.}}}{\sqrt{\frac{A_1^i A_2^f}{A_1^f A_2^i}\frac{E_{\text{c.m.}}}{TKE}} - \cos\theta_{\text{c.m.}}} \tag{3.2}$$

Table 3.1: Results of the TDHF calculations for the ^{48}Ca + ^{244}Pu system at $E_{\text{c.m.}} = 203.2$ MeV for the tip orientation of the ^{244}Pu nucleus and the ^{86}Kr + ^{198}Pt system at $E_{\text{c.m.}} = 324.2$ MeV for the tip orientation of the ^{198}Pt nucleus. The table was taken from Ref. [1]

ℓ_i ($\hbar$)	Z_1^f	A_1^f	Z_2^f	A_2^f	$TKE(MeV)$	t_{c}(zs)	$\theta_{\text{c.m.}}$	θ_1^{lab}	θ_2^{lab}
^{48}Ca + ^{244}Pu system at $E_{\text{c.m.}} = 203.2$ MeV									
44	35.4	88.9	78.6	203.1	218.8	6.4	94.9	78.8	53.7
46	35.1	88.4	78.9	203.6	217.8	6.5	89.1	73.4	57.6
48	35.0	89.4	79.0	203.6	216.6	6.6	84.0	68.6	61.4
50	35.0	88.2	79.0	203.8	217.2	6.6	79.7	64.9	64.3
52	34.9	87.7	79.1	204.3	218.3	6.6	76.7	62.4	66.5
54	34.9	87.6	79.1	204.4	218.4	6.5	74.1	60.1	68.5
56	35.1	87.9	78.9	204.1	216.9	6.5	70.9	57.2	71.0
58	34.7	86.8	79.3	205.2	215.2	6.6	66.9	53.8	73.6
60	35.5	83.8	80.5	208.2	214.8	6.7	62.2	50.1	76.4
62	35.5	88.7	78.5	203.3	215.6	7.0	56.3	44.7	83.4
64	36.6	92.1	77.4	199.9	211.1	8.2	43.6	34.1	-83.1
66	33.9	84.5	80.1	207.5	197.5	7.9	43.7	34.4	-88.5
68	32.5	80.8	81.5	211.2	190.0	6.8	57.4	45.7	76.4
70	26.5	65.0	87.5	227.0	168.2	5.2	75.1	61.9	55.9
^{86}Kr + ^{198}Pt system at $E_{\text{c.m.}} = 324.2$ MeV									
60	39.1	95.9	74.9	188.1	214.2	4.2	109.4	75.3	32.8
70	37.6	92.3	76.4	191.7	215.6	3.4	110.7	77.5	31.6
80	36.7	89.7	77.3	194.3	220.6	2.9	102.9	71.8	34.9
90	36.8	89.8	77.2	194.2	219.3	2.6	106.9	75.1	33.1
100	36.2	88.4	77.8	195.6	223.6	2.3	98.4	68.6	36.7
110	36.2	88.1	77.8	195.9	231.9	2.0	103.7	73.6	34.8
120	36.2	88.3	77.8	195.7	242.5	1.7	93.9	66.0	39.7

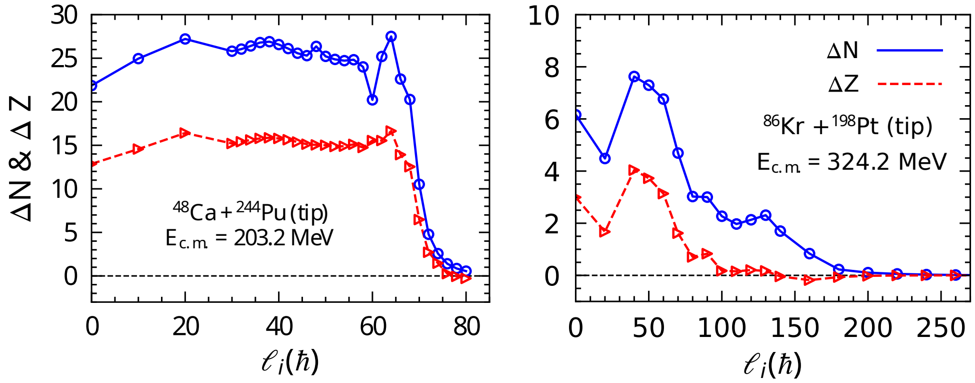

Figure 3.2: Average numbers of change in neutron and proton numbers in ^{48}Ca+^{244}Pu system at $E_{\text{c.m.}} = 203.2$ MeV and ^{86}Kr + ^{198}Pt system at $E_{\text{c.m.}} = 324.2$ MeV for the tip orientation of the target-like nuclei are shown as a function of initial angular momentum ℓ_i [1].

As can be seen in Tab. 3.1, the TDHF computation results for ^{48}Ca + ^{244}Pu system predicts a pronounced plateau behavior in the average number of nucleons of Pu-like fragment nuclei throughout all analyzed initial angular momenta, which may be due to significant stability of doubly magic ^{208}Pb in the exit channel. In Fig. 3.2, the average numbers of change in neutron and proton numbers in ^{48}Ca + ^{244}Pu system at $E_{\text{c.m.}} = 203.2$ MeV and ^{86}Kr + ^{198}Pt system at $E_{\text{c.m.}} = 324.2$ MeV for the tip orientation of the target-like nuclei are shown as a function of initial angular momentum ℓ_i. As the initial angular momentum increases, the average number of changes in both proton and neutron numbers decreases. This behavior is usually expected and observed in QF reactions. In Fig. 3.2, one can easily see that the average number of transferred nucleons is much higher in ^{48}Ca + ^{244}Pu system compared to the ^{86}Kr + ^{198}Pt system. This is mainly due to the difference in charge product (Z_pZ_t) of the two systems. We also have to mention that fusion reactions are not observed in either reaction in the tip orientation of the target-like fragments. Yet, within our calculations, which are not shared here, fusion emerges within the side orientation of the ^{244}Pu nucleus during central collisions.

3.1.2 Mean Drift Path and Reduced Curvature Parameters

To calculate the average values of reduced curvature parameters which mentioned in the Sec. 2.3, the collision at the initial angular momentum $\ell_i = 40\hbar$ is selected for the ^{48}Ca + ^{244}Pu system and the collision at $\ell_i = 60\hbar$ is selected for the ^{86}Kr + ^{198}Pt system. In Fig. 3.3, the time evolution of mean values of the neutron $N(t)$ and proton $Z(t)$ numbers of target-like fragments in ^{48}Ca+^{244}Pu at $\ell_i = 40\hbar$ and ^{86}Kr+^{198}Pt system at $\ell_i = 60\hbar$ are shown [1]. In Fig. 3.3, labels $t_A,\ t_B$,and t_C denote the time intervals used for calculating the average values of reduced curvature parameters in each system. To project the change in neutron and proton numbers of collision partners into $N - Z$ plane, time dependence in $N_1(t)$ and $Z_1(t)$ is eliminated, and the resultant graph is given in Fig. 3.4. In Fig. 3.4, dashed black lines represent the iso-scalar lines, and thick blue lines represent the mean drift path of the target-like fragments in each system. In both systems, the iso-scalar line extends from the projectile-like fragment up to the target-like fragment, passing through the mass symmetry point (N_0, Z_0), where $N_0 = (N_1 + N_2)/2$. The charge asymmetry of the reaction fragments, denoted with $\delta = \frac{N-Z}{A}$, are found to be $\delta(\text{Ca}) \simeq 0.167$, $\delta(\text{Pu}) \simeq 0.229$, $\delta(\text{Kr}) \simeq 0.163$, and $\delta(\text{Pt}) \simeq 0.212$.

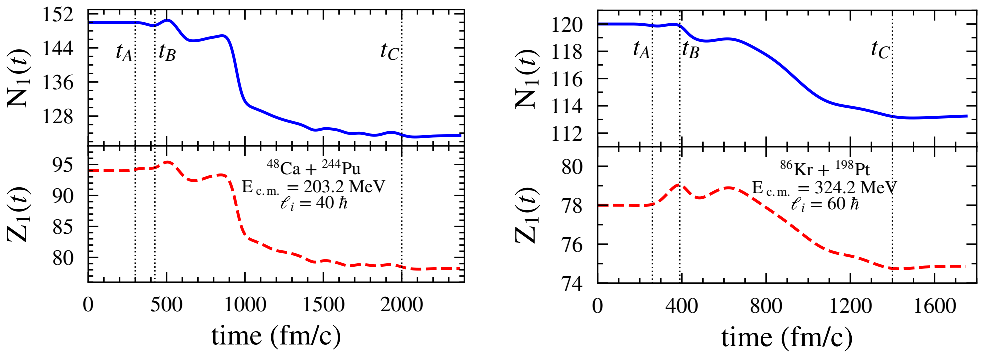

Figure 3.3: Mean values of neutron and proton numbers of target-like fragments at initial angular momentum $\ell_i = 40\hbar$ for ^{48}Ca + ^{244}Pu system at $E_{\text{c.m.}} = 203.2$ MeV and $\ell_i = 60\hbar$ for ^{86}Kr + ^{198}Pt system at $E_{\text{c.m.}} = 324.2$ MeV are shown as a function of time. Solid blue lines denote the neutron numbers, and dashed red lines denote the proton numbers of target-like fragments. The labels t_A, t_B, and t_C indicate the projection of the time intervals used to determine the curvature parameters. The figure was taken from Ref. [1].

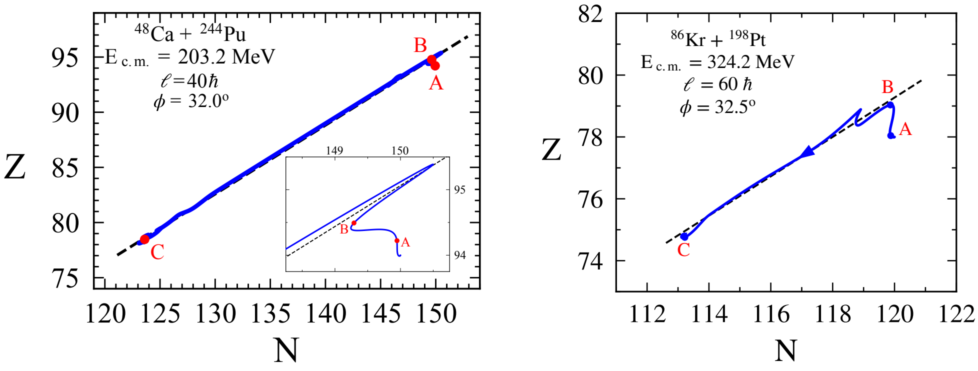

Figure 3.4: Mean drift path in the $N-Z$ plane for the target-like fragments are given at initial angular momentum $\ell_i = 40\hbar$ for ^{48}Ca + ^{244}Pu system at $E_{\text{c.m.}} = 203.2$ MeV and $\ell_i = 60\hbar$ for ^{86}Kr + ^{198}Pt system at $E_{\text{c.m.}} = 324.2$ MeV. Solid blue lines denote the mean drift path and dashed black lines denote the iso-scalar lines. The labels A, B, and C indicate the projection of the time intervals used to determine the curvature parameters. The figure was taken from Ref. [1].

Because the reaction partners in both systems have different charge asymmetries, during the initial phase of the collision, the reaction partners exchange nucleons to reach the same charge asymmetry value, which is $\delta \simeq 0.219$ (^{48}Ca + ^{244}Pu system) and $\delta \simeq 0.197$ (^{86}Kr + ^{198}Pt system). In this stage, the resulting drift is towards the iso-scalar line in the iso-vector direction. Then, the reaction partners continue to exchange nucleons and drift towards the local equilibrium, the mass symmetry point. But, since the contact time is insufficient, the reaction partners separate long before reaching the mass symmetry point.

The quantal diffusion coefficients related to both systems are calculated, and the results for each system are given in Fig. 3.5. As described in Sec. 2.3, one can calculate the average values of reduced curvature parameters by using the quantal diffusion coefficients, neutron and proton numbers of TLF. In the ^{48}Ca + ^{244}Pu system, the parameter $\overline{\alpha}$ is calculated between the time interval $(300-425)$ fm/c and its value is equal to 0.156. The parameter $\overline{\beta}$ is calculated between the time interval $(425-2000)$ fm/c, and its value equals 0.004. In the ^{86}Kr + ^{198}Pt system, parameter $\overline{\alpha}$ is calculated between the time interval $(260-390)$ fm/c and it is equal to 0.176. The parameter $\overline{\beta}$ is calculated between the time interval $(390-1400)$ fm/c, equal to 0.003.

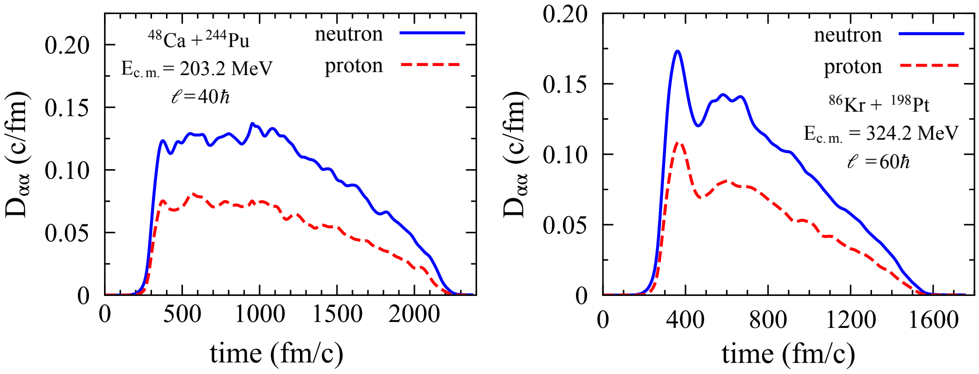

Figure 3.5: Diffusion coefficient for neutron and proton transfers at initial angular momentum $\ell = 40\hbar$ for ^{48}Ca + ^{244}Pu system at $E_{\text{c.m.}} = 203.2$ MeV, and $\ell = 60\hbar$ for ^{86}Kr + ^{198}Pt system at $E_{\text{c.m.}} = 324.2$ MeV are shown as a function of time. Solid blue lines denote the diffusion coefficients of neutron transfer, $D_{NN}(t)$; dashed red lines denote the diffusion coefficients of proton transfer, $D_{ZZ}(t)$. The figure was taken from Ref. [1].

3.2 SMF results

3.2.1 Covariances of fragment charge and mass distributions

In both systems, Eqs.(2.8-2.10) are solved numerically for the proton, neutron variances, and mixed covariances by using the calculated reduced curvature parameters and the quantal diffusion coefficients. In Tab. 3.2, we share the asymptotic values for neutrons σ_{NN}, protons σ_{ZZ}, mixed σ_{NZ}, and mass σ_{AA} dispersions calculated for each initial angular momentum. As an example, the calculated neutron, proton, and mixed variances as a function of time in ^{48}Ca + ^{244}Pu reaction at $\ell_i = 40\hbar$ and ^{86}Kr + ^{198}Pt reaction at $\ell_i = 60\hbar$ are shown in Fig 3.6. In both systems, we see that during the initial phase of the reaction, up to about $t \simeq 500$ fm/c, the magnitude of variances are in order as $\sigma_{NZ} < \sigma_{ZZ} < \sigma_{NN}$. After that, the correlations evolve, changing the order to $\sigma_{ZZ} < \sigma_{NZ} < \sigma_{NN}$, demonstrating the importance of correlations arising from significant energy dissipation[1, 73].

Table 3.2: Results of the SMF calculations for the ^{48}Ca + ^{244}Pu system at $E_{\text{c.m.}} = 203.2$ MeV in tip configuration of ^{244}Pu nucleus and the ^{86}Kr+^{198}Pt system at $E_{\text{c.m.}} = 324.2$ MeV in tip configuration of ^{198}Pt nucleus. The table was taken from Ref. [1].

^{48}Ca + ^{244}Pu					^{86}Kr + ^{198}Pt				
ℓ_i ($\hbar$)	σ_{NN}	σ_{ZZ}	σ_{NZ}	σ_{AA}	ℓ_i ($\hbar$)	σ_{NN}	σ_{ZZ}	σ_{NZ}	σ_{AA}
44	11.6	7.4	8.9	18.7	60	10.3	6.7	8.0	16.7
46	11.6	7.5	8.9	18.7	70	9.4	6.2	7.2	15.2
48	11.7	7.5	9.0	18.8	80	8.5	5.6	6.4	13.7
50	11.7	7.5	9.0	18.8	90	7.9	5.2	5.9	12.6
52	11.7	7.5	8.9	18.8	100	7.2	4.8	5.3	11.5
54	11.6	7.4	8.9	18.6	110	6.6	4.4	4.8	10.4
56	11.5	7.4	8.8	18.5	120	5.9	4.0	4.1	9.2
58	11.4	7.3	8.8	18.4					
60	11.5	7.4	8.8	18.5					
62	11.5	7.4	8.8	18.5					
64	11.9	7.6	9.2	19.2					
66	11.5	7.4	8.8	18.5					
68	10.6	6.8	8.1	17.0					
70	8.9	5.8	6.7	14.2					

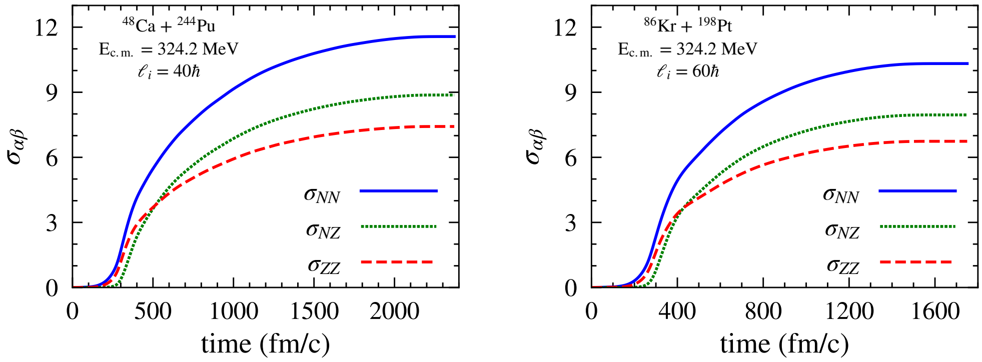

Figure 3.6: Neutron, proton, and mixed variances as a function of time in ^{48}Ca+^{244}Pu system and ^{86}Kr + ^{198}Pt system. Solid blue, dashed red, and dotted green lines denote the neutron variances, σ_{NN}; proton variances, σ_{ZZ}; and the mixed variances, σ_{NZ}, respectively. The figure was taken from Ref. [1].

3.2.2 Primary Mass Distribution

In this section, we continue with discussing the primary fragment distributions in ^{48}Ca + ^{244}Pu system at $E_{\text{c.m.}} = 203.2$ MeV and ^{86}Kr + ^{198}Pt system at $E_{\text{c.m.}} = 324.2$ MeV, and compare the results with the available experimental data [6, 7]. In both systems, we have to use Eq. 2.38 since both QF and FF mechanisms have contributions in primary mass distributions, especially near the mass symmetric region. The initial angular momentum boundaries in Eq. 2.37 are determined by comparing the mass-energy distributions shown in Fig. 3.1 and the scattering angles in the laboratory frame, θ^1_{lab} and θ^2_{lab}, given in Tab. 3.1, with the experimentally observed mass-energy distributions and angular coverage ranges in the Refs. [7, 6]. The TKE vs. mass value is scattered in the TKE-mass plane for each computed collision with different initial angular momentum values, and the resulting distribution is plotted for both systems in Fig. 3.7. The red continuous contours in Fig. 3.7 represent the gates used in the experiments in Refs. [6, 5, 7] to exclude or reduce the contributions from the elastic events. With these constraints taken into account, we determined that the initial angular momenta range in Eq. 2.37 to be $44\hbar \leq \ell_i \leq 70\hbar$ for the ^{48}Ca + ^{244}Pu system and $60\hbar \leq \ell_i \leq 120\hbar$ for the ^{86}Kr + ^{198}Pt system. It is essential to mention that, for the side orientation of the target nuclei, the primary binary products do not satisfy the angular range and mass-energy conditions at the same time. Thus, in this study, primary fragment yield distributions are calculated using only the tip orientation of target nuclei in both systems. In Fig. 3.8, we share the calculated primary product distributions for ^{48}Ca + ^{244}Pu system at $E_{\text{c.m.}} = 203.2$ MeV and ^{86}Kr + ^{198}Pt system at $E_{\text{c.m.}} = 324.2$ MeV in tip orientation of target-like nucleus and compare the results with the experimental data available [7, 6]. Dashed blue lines indicate primary product mass distribution calculated within the SMF framework, whereas filled green areas represent the fusion-fission fragment distribution calculated using the GEMINI++ code [8]. The summation of yield distribution calculated by Eq. 2.38 is indicated by solid red lines. For comparison, the positions of initial reaction partners are shown by vertical dashed black lines in Fig. 3.8.

In Eq. 2.38, the value of η^{MNT} is determined by matching the peak values of experimental yield [7] at A≈208 to give value $\eta^{\text{MNT}} = 202$ for ^{48}Ca + ^{244}Pu system

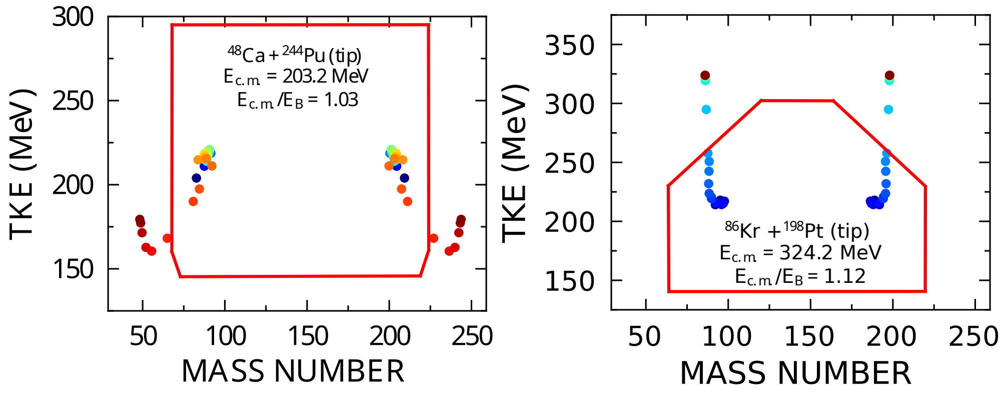

Figure 3.7: Mass-energy distributions of fragments obtained by the TDHF calculations for the ^{48}Ca + ^{244}Pu system at $E_{\text{c.m.}} = 203.2$ MeV and ^{86}Kr + ^{198}Pt system at $E_{\text{c.m.}} = 324.2$ MeV in tip orientation of target-like nucleus. The red continuous contours represent the gates used in the experiments in Refs. [6, 5, 7] to exclude or reduce the contributions from the elastic events. The figure was taken from Ref. [1].

and peak value of experimental yield [6] at A≈200 to give value $\eta^{\text{MNT}} = 230$ for ^{86}Kr + ^{198}Pt system. Similarly, for FF mechanism, the value of η^{FF} is determined by matching the experimental yield at A≈146 for both systems to give value $\eta^{FF} = 17$ for ^{48}Ca + ^{244}Pu system and $\eta^{FF} = 4$ for ^{86}Kr + ^{198}Pt system.

First, we can compare the SMF results obtained by calculating the Eq. 2.37 for both systems. In the vicinity of the peak position, around 40 nucleons are exchanged between the reaction partners in ^{48}Ca + ^{244}Pu system, and five nucleons are exchanged in the ^{86}Kr+^{198}Pt system. Firstly, it is evident from Fig. 3.8 that the SMF approach in both systems can accurately predict the peak position of the mass distribution. Moreover, in the ^{48}Ca + ^{244}Pu system, the SMF method can explain the transfer channels up to ~55 nucleon transfer, or up to A$\approx$ 100 for projectile-like fragments ($A \approx 190$ for target-like fragments). In the mass symmetric region, the contributions from FF reactions play an important role, especially in the ^{48}Ca + ^{244}Pu system. It can be seen from GEMINI++ results that the ^{292}Fl compound nucleus decays mainly by the fission mechanism, and the distribution resembles a symmetric Gaussian distribution. With the inclusion of the contributions from the FF reactions, we can clearly state that the results indicated by the solid red lines coincide with the experimental data values quite well in the ^{48}Ca + ^{244}Pu system.

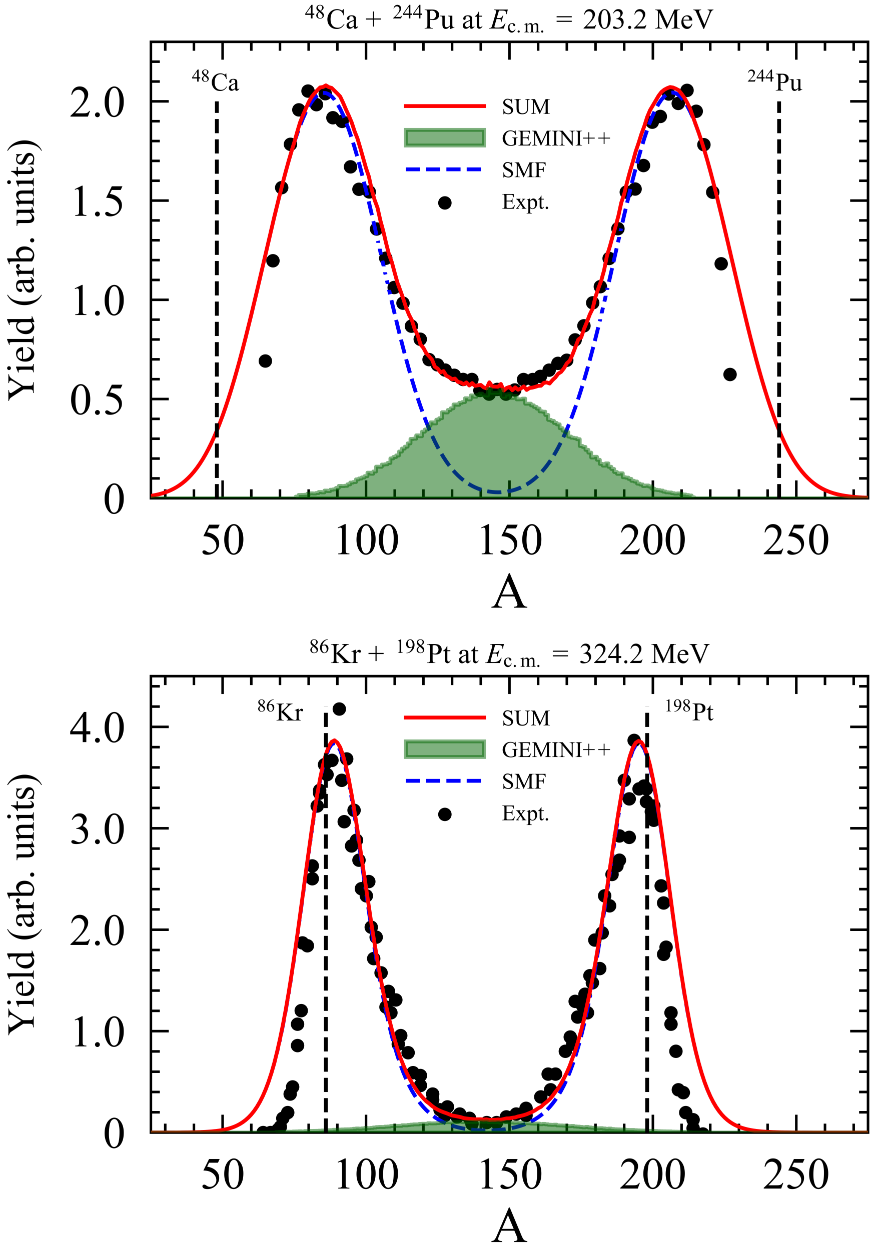

Figure 3.8: Primary fragment yield in the $^{48}\mathrm{Ca} + {}^{244}\mathrm{Pu}$ system at $E_{\mathrm{c.m.}} = 203.2$ MeV and $^{86}\mathrm{Kr} + {}^{198}\mathrm{Pt}$ system at $E_{\mathrm{c.m.}} = 324.2$ MeV in tip orientation of target-like nucleus. The experimental data obtained from Refs. [7, 6] are indicated by the closed black circles. Dashed blue lines indicate the primary product mass distributions calculated within the SMF framework. The FF fragment distribution indicated by the green filled area was calculated using the GEMINI++ code [8]. Solid red lines indicate the summation of yield distribution calculated by the SMF approach and GEMINI++. The figure was taken from Ref. [1].

In the ^{86}Kr $+$ ^{198}Pt system, we can see from the experimental results that the competing QF reactions heavily hinder FF reactions. This is mainly due to the strong Coulomb repulsion present in the system, which inhibits the compound nucleus formation during the collision. Similarly, in the ^{86}Kr $+$ ^{198}Pt system, we can see that the contributions from QF reactions predicted by the SMF approach are dominant compared to the FF reactions and the SMF results agree quite well with the experimental data over the whole mass range. It is also important to mention here that, since the primary mass fragment probability $P_\ell(A)$ in Eq.2.35(or Eq. 2.36) is normalized to unity, the value of normalization constant η^{MNT} also determines the total integrated yield value under the mass-distribution function. To compare and analyze the contribution from FF reactions in both systems, we can calculate the ratio of integrated yield value in the mass symmetric ($A_{\text{CN}} \pm 20$) region to the total integrated yield value under the available experimental data range. The interval for the available experimental data range in the ^{48}Ca$+$^{244}Pu system is taken as $65 \leq A \leq 225$ to give the value $22.3/201.3 \approx 11\%$. Similarly, in the ^{86}Kr $+$ ^{198}Pt system the interval is taken as $65 \leq A \leq 215$ to give the value $6.5/225.4 \approx 3\%$. These results agree with the experimentally calculated results in Refs. [7, 6]. By comparing the calculated ratio values for both systems, we can clearly state that with the increasing Coulomb factor ($Z_p Z_t$), QF reactions dominate the FF reactions.

CHAPTER 4

PRIMARY AND SECONDARY ISOTOPE PRODUCTION IN $^{250}\mathrm{Cf} + ^{232}\mathrm{Th}$ REACTION

In this part of Chapter 3 of the thesis, we extend our calculation to reactions where both of the binary reaction fragments lie within the superheavy region of the nuclear chart. Here, we investigate the primary and secondary isotope production in the $^{250}\mathrm{Cf} + ^{232}\mathrm{Th}$ reaction at $\mathrm{E_{c.m.}} = 950.0$ MeV. In this system, both nuclei exhibit strong prolate deformation in their ground states. Thus, the relative orientation of the reaction partners strongly affects the collision dynamics and the MNT mechanism. To analyze the effect of relative orientation of reaction partners, we consider tip-tip (XX), tip-side (XY), side-tip (YX), and side-side (YY) geometries, where similar to Ref. [64], we indicate initial orientation of the target or projectile along the beam direction with letter X, and perpendicular to the beam direction with letter Y. In the Ref. [64], within the framework of the TDHF, head-on collisions ($\ell_i = 0\hbar$) in the $^{250}\mathrm{Cf} + ^{232}\mathrm{Th}$ reaction are analyzed at various bombarding energies and at five different relative orientations. The average variation of proton and neutron numbers of the ^{250}Cf-like fragments as a function of center-of-mass energy is given in Fig. 3 in Ref. [64]. It has been observed that the maximum number of nucleons are transferred roughly at $\mathrm{E_{c.m.}} = 950$ MeV. There is no experimental work performed on this system yet; however, our calculations can be considered as a suggestion for an experiment on this system.

4.1 Mean Reaction Dynamics in TDHF

4.1.1 Mean values of reaction observables

This computation and all other numerical computations in this section are carried out by employing the three-dimensional TDHF program of Umar et al. [180, 181] using the SLy4d Skyrme energy density functional [182, 183], with a box size of 60 $\times$ 60 $\times$ 36 fm in the $x-y-z$ directions. For each different relative orientation, the collisions ranging from $0\hbar$ to $480\hbar$ are evaluated for every forty units of initial angular momentum. In Tab. 4.1 and Tab. 4.2 the TDHF results for ^{250}Cf + ^{232}Th system at $E_{\text{c.m.}} = 950.0$ MeV are shown for a range initial orbital angular momenta, ℓ_i, final values of charge and mass numbers of Cf-like fragments Z_1^f, A_1^f and Th-like fragments Z_2^f, A_2^f, final total kinetic energy TKE (in MeV units), the scattering angles in the center of mass frame $\theta_{\text{c.m.}}$, and the laboratory frame θ_1^{lab} and θ_2^{lab} for the four different collision geometries. In Fig. 4.1, the average numbers of change in neutron and proton numbers after the collision in ^{250}Cf + ^{232}Th system at $E_{\text{c.m.}} = 950.0$ MeV in tip-tip (XX), tip-side (XY), side-tip (YX), and side-side (YY) collision geometries are shown. In tip-tip and tip-side geometries, the heavier partner (Cf-like fragments) loses nucleons, resulting in more mass symmetric yields in the exit channel.

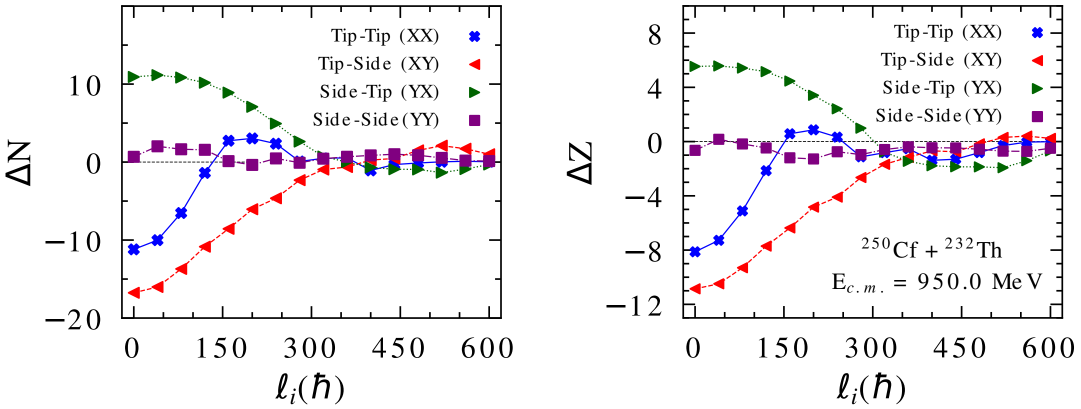

Figure 4.1: Average numbers of change in neutron and proton numbers as a function of initial angular momentum ℓ_i in ^{250}Cf + ^{232}Th system at $E_{\text{c.m.}} = 950.0$ MeV in tip-tip (XX), tip-side (XY), side-tip (YX), and side-side (YY) collision geometries.

Table 4.1: Results of the TDHF and SMF calculations for the ^{250}Cf + ^{232}Th system at $E_{\text{c.m.}} = 950.0$ MeV in tip-tip (XX), and tip-side (XY) geometries.

Geometry	ℓ_i $(\hbar)$	Z_1^f	A_1^f	Z_2^f	A_2^f	ℓ_f $(\hbar)$	TKE	$\theta_{\text{c.m.}}$	θ_1^{lab}	θ_2^{lab}
tip-tip (XX)	0	89.9	230.7	98.1	251.3	0.0	612.8	180.0	0.0	0.0
	40	90.7	232.7	97.3	249.3	27.1	606.7	171.9	3.7	28.6
	80	92.9	238.4	95.1	243.6	63.1	603.9	163.2	7.6	47.6
	120	95.9	246.5	92.1	235.5	92.4	589.0	154.0	11.5	55.9
	160	98.6	253.3	89.4	228.7	123.3	571.1	144.5	15.3	57.8
	200	98.9	253.9	89.1	228.1	147.9	564.3	135.2	19.1	56.0
	240	98.3	252.7	89.7	229.3	178.1	563.6	125.3	23.3	53.1
	280	96.9	248.9	91.1	233.0	219.5	567.0	115.3	27.8	49.3
	320	97.2	249.7	90.8	232.3	243.4	590.4	106.9	31.6	47.1
	360	97.5	250.0	90.5	232.0	258.7	625.5	100.9	34.7	45.8
	400	96.6	247.5	91.4	234.4	283.8	668.3	95.8	37.8	44.4
	440	96.7	248.4	91.3	233.6	330.9	718.7	90.5	41.0	43.2
	480	97.2	249.1	90.8	232.9	398.7	774.9	85.7	44.1	42.0
tip-side (XY)	0	87.1	222.4	100.9	259.6	0.0	627.4	180.0	0.0	0.0
	40	87.5	223.5	100.5	258.5	30.7	624.7	169.7	4.9	31.3
	80	88.7	227.0	99.3	255.0	64.7	625.0	159.1	9.9	47.7
	120	90.3	231.4	97.7	250.6	98.6	612.5	148.4	14.6	52.9
	160	91.6	235.1	96.4	246.9	141.6	592.2	137.1	19.5	52.7
	200	93.2	239.1	94.8	242.9	181.7	586.2	125.9	24.2	51.3
	240	93.9	241.3	94.1	240.7	212.1	591.6	116.4	28.2	49.1
	280	95.4	245.0	92.6	237.0	244.7	569.0	107.6	31.3	46.0
	320	96.3	247.4	91.7	234.6	258.7	607.0	102.1	34.1	45.4
	360	96.8	248.2	91.2	233.8	286.5	634.0	96.1	37.0	43.8
	400	97.3	249.6	90.7	232.4	316.7	667.6	91.4	39.4	42.7
	440	97.3	249.7	90.7	232.3	363.7	708.3	87.4	42.0	41.7
	480	97.8	251.3	90.2	230.7	400.7	745.3	83.5	44.2	40.7

Table 4.2: Results of the TDHF calculations for the ^{250}Cf + ^{232}Th system at $E_{\text{c.m.}} = 950.0$ MeV in side-tip (YX), and side-side (YY) geometries. The table was taken from Ref. [1].

Geometry	ℓ_i ($\hbar$)	Z_1^f	A_1^f	Z_2^f	A_2^f	ℓ_f ($\hbar$)	TKE	$\theta_{\text{c.m.}}$	θ_1^{lab}	θ_2^{lab}
side-tip (YX)	0	103.5	266.5	84.5	215.5	0.0	647.7	180.0	0.0	0.0
	40	103.6	266.7	84.4	215.3	30.8	647.3	169.9	4.4	70.0
	80	103.4	266.3	84.6	215.7	73.4	644.5	159.6	8.9	71.7
	120	103.2	265.3	84.8	216.7	96.8	632.4	149.6	13.1	68.0
	160	102.5	263.4	85.5	218.6	133.0	613.8	139.1	17.5	62.8
	200	101.4	260.5	86.6	221.5	177.4	607.1	128.6	22.0	58.1
	240	100.4	257.3	87.6	224.7	207.5	601.3	119.0	26.1	53.5
	280	99.0	253.6	89.0	228.4	238.9	597.5	110.1	30.1	49.2
	320	97.2	249.9	90.8	232.1	265.0	615.7	103.1	33.6	46.4
	360	96.5	248.6	91.5	233.4	286.2	642.3	97.6	36.4	44.7
	400	96.2	247.5	91.8	234.5	315.1	668.2	92.3	39.3	42.8
	440	96.1	247.2	91.9	234.8	346.4	700.5	87.9	41.9	41.5
	480	96.1	247.2	91.9	234.8	387.8	740.5	84.2	44.3	40.5
side-side (YY)	0	97.4	250.0	90.6	232.0	0.0	620.0	180.0	0.0	0.0
	40	98.2	252.2	89.8	229.8	27.3	634.6	167.6	5.5	55.3
	80	97.8	251.5	90.2	230.5	51.1	632.9	155.0	11.2	62.1
	120	97.5	251.1	90.5	230.9	90.9	627.0	142.8	16.5	60.6
	160	96.8	248.9	91.2	233.1	135.7	613.6	130.7	21.8	56.2
	200	96.7	248.3	91.3	233.7	177.0	616.9	120.7	26.3	52.9
	240	97.2	249.7	90.8	232.3	199.3	639.5	113.1	29.8	51.2
	280	97.0	249.0	91.0	233.0	236.8	638.0	105.1	33.2	47.7
	320	97.4	249.8	90.6	232.2	280.7	627.6	97.5	36.1	44.4
	360	97.6	250.3	90.4	231.7	312.6	638.7	93.0	38.1	42.8
	400	97.5	250.4	90.5	231.6	341.0	659.1	87.5	40.8	40.8
	440	97.5	250.5	90.5	231.5	378.4	687.9	83.8	42.9	39.7
	480	97.4	250.3	90.6	231.7	416.4	725.6	81.2	44.9	39.2

This type of transfer is usually expected in QF reactions. However, in collision with small initial angular momenta, $\ell_i \leq 80\hbar$ for tip-tip and $\ell_i \leq 160\hbar$ for tip-side, Cf-like fragments lose nucleons during the collision until they reach thorium-side of the nuclear chart and become the lighter fragment. This type of reaction is called 'Swap Inverse Quasifission' in the Ref. [64]. In side-tip (YX) and side-side (YY) geometries, the reaction dynamics are completely different than tip-tip (XX) and tip-side (XY) geometries. In these geometries, heavy Cf-like fragments gain nucleons and become heavier. The IQF reaction observed in these geometries are crucial for producing neutron-rich isotopes within the superheavy region with reasonable yields. Also, with increasing initial angular momentum, kinetic energy dissipation and the total number of transferred nucleons decrease throughout all geometries.

4.1.2 Mean Drift Path and Reduced Curvature Parameters

Since the reaction dynamics differ throughout all four geometries, the reduced curvature parameters are calculated separately for each geometry. In this system, the charge asymmetry values of ^{250}Cf and ^{232}Th are both equal to 0.22. As a result, nucleon drift in the iso-vector direction is not observed during the collision. In other words, the nucleon transfer takes place only in the iso-scalar direction. Because of this, to calculate the iso-vector reduced curvature parameter, $\overline{\alpha}$, the neighboring ^{240}Cf$+^{246}$Th system at $E_{\text{c.m.}} = 950.0$ MeV is analyzed [4, 9]. The detailed calculations of iso-scalar and iso-vector reduced curvature parameters are given in the following sections, Sec. 4.1.2.1 and Sec. 4.1.2.2.

4.1.2.1 Reduced Curvature Parameter β

To calculate the average values of iso-scalar reduced curvature parameters mentioned in the Sec. 2.3, in all four geometries, the collisions at the initial angular momentum $\ell_i = 0\hbar$ are selected for the ^{250}Cf $+$ ^{232}Th system. In Fig. 4.2, the time evolution of mean values of the neutron $N(t)$ and proton $Z(t)$ numbers of target-like fragments in ^{250}Cf $+$ ^{232}Th at $\ell_i = 0\hbar$ are shown [9]. In Fig. 4.2, labels $t_A,\ t_B$,and t_C denote the time intervals used for calculating the averaged value of iso-scalar reduced curvature

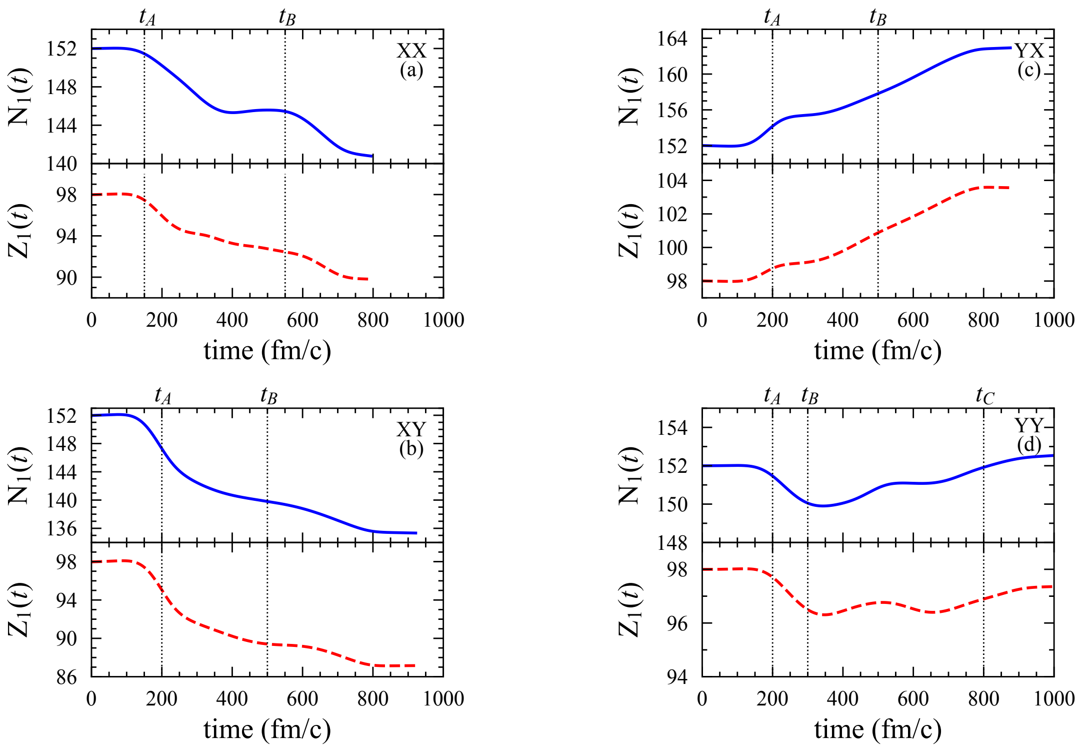

Figure 4.2: Mean values of neutron and proton numbers of Cf-like fragments at initial angular momentum $\ell_i = 0\hbar$ for ^{250}Cf $+$ ^{232}Th system at $E_{\text{c.m.}} = 950.0$ MeV in tip-tip (XX), tip-side (XY), side-tip (YX), and side-side (YY) are shown as a function of time. Solid blue lines denote the neutron numbers, and dashed red lines denote the proton numbers of Cf-like fragments during the collision. The labels t_A, t_B, and t_C indicate the projection of the time intervals used to determine the averaged value of iso-scalar reduced curvature parameter, $\overline{\beta}$. The figure was taken from Ref. [9].

parameter, $\overline{\beta}$, in each relative orientation. To project the change in neutron and proton numbers of collision partners into $N - Z$ plane, time dependence in $N_1(t)$ and $Z_1(t)$ is eliminated, and the resultant graph is given in Fig. 4.3. In Fig. 4.3, solid blue lines represent the mean drift path of Cf-like fragments, and thick black lines represent the iso-scalar line. As mentioned in Sec. 4.1.2, since charge asymmetry values of reaction partners are roughly equal, mean drift takes place parallel to the iso-scalar line. This trend can be seen in every relative orientation in Fig. 4.3. The quantal diffusion coefficients related to each different relative orientation are calculated, and the results for each geometry are given in Fig. 4.4. In the tip-tip (XX) geometry, Cf-like heavy fragments lose nucleons along the stability valley until they reach the

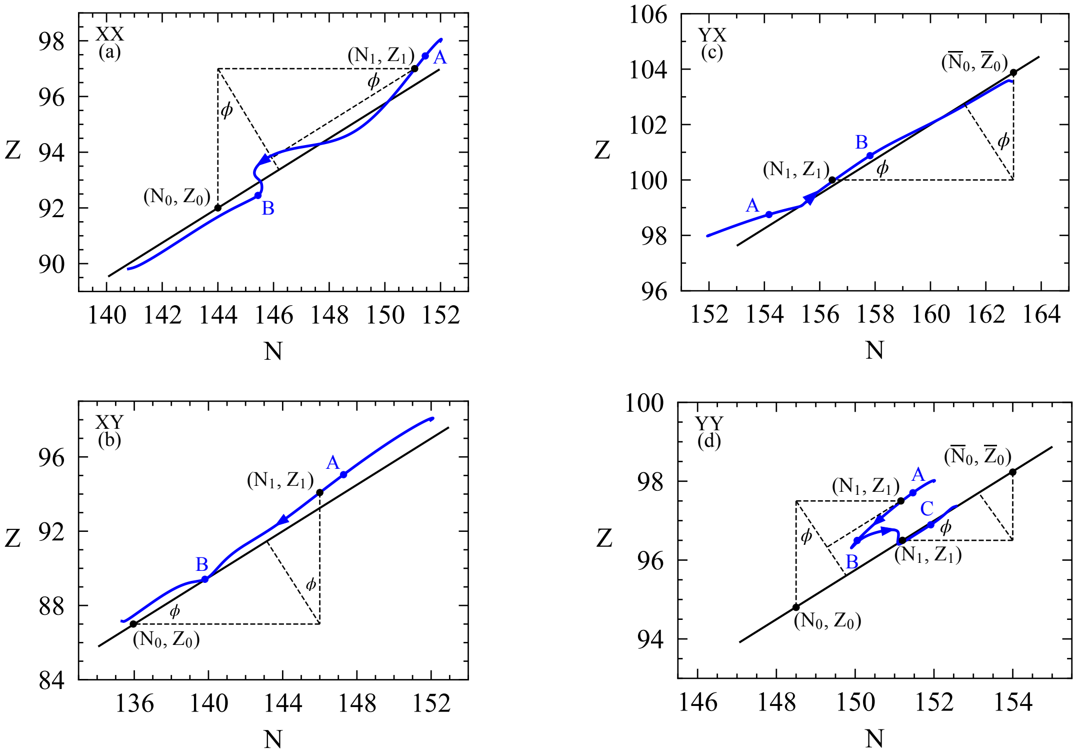

Figure 4.3: Mean drift path in the $N - Z$ plane for the target-like fragments are given at initial angular momentum $\ell_i = 0\hbar$ for ^{250}Cf + ^{232}Th system at $E_{\text{c.m.}} = 950.0$ MeV [9]. Solid blue lines denote the mean drift path and thick black lines denote the iso-scalar lines. The labels A, B, and C indicate the projection of the time intervals used to determine the averaged value of the reduced iso-scalar curvature parameter, $\overline{\beta}$. The figure was taken from Ref. [9].

vicinity of the thorium isotopes. The $\overline{\beta}$ is calculated by using Eq. 2.25 between the interval, $t_A = 150$ fm/c and $t_B = 550$ fm/c to give value $\overline{\beta}(XX) = 0.005$. In tip-side (XY) geometry, we see a similar mean drift path, and similarly, in this relative orientation, the time interval is taken as $t_A = 200$ fm/c and $t_B = 500$ fm/c to give value $\overline{\beta}(XY) = 0.009$. The mean drift in side-tip (YX) is completely different, where Cf-like heavy fragments gain nucleons to reach the vicinity of $Z = 104$, rutherfordium isotopes. Roughly 17 nucleons drift from Th-like fragments to Cf-like fragments along the stability valley. In this IQF reaction, the interval for parameter $\overline{\beta}$ is taken as $t_A = 200$ fm/c and $t_B = 500$ fm/c to give value $\overline{\beta}(YX) = 0.009$. Finally, in side-side$(YY)$ geometry, Cf-like fragments lose nucleons along the stability valley at the initial stages of the reaction. Then, until separation is mainly caused by Coulomb

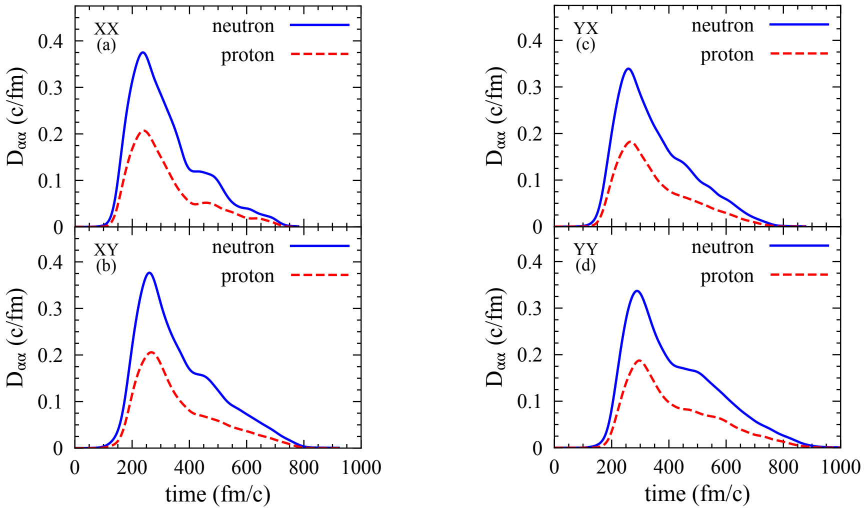

Figure 4.4: Diffusion coefficient for neutron and proton transfers at initial angular momentum $\ell = 0\hbar$ for ^{250}Cf + ^{232}Th system at $E_{\mathrm{c.m.}} = 950.0$ MeV are shown as a function of time. Solid blue lines denote the diffusion coefficients of neutron transfer, $D_{NN}(t)$; dashed red lines denote the diffusion coefficients of proton transfer, $D_{ZZ}(t)$. The figure was taken from Ref. [9].

repulsion, it gains nucleons again along the stability valley, resulting in almost no transfer in total. In this geometry, we use the average value of two calculated $\overline{\beta}$ parameter values given with $\overline{\beta}(YY) = \left(\overline{\beta}_{sym} + \overline{\beta}_{asym}\right)/2$. Where $\overline{\beta}_{sym}$ is calculated between the time interval $t_A = 200$ fm/c and $t_B = 300$ fm/c in which drift is towards the symmetry to give value $\overline{\beta}_{sym} = 0.004$ and $\overline{\beta}_{asym}$ is calculated between the time interval $t_B = 300$ fm/c and $t_C = 800$ fm/c in which drift is towards the asymmetry to give the same value $\overline{\beta}_{asym} = 0.004$. The mean value is then calculated as $\overline{\beta}(YY) = 0.004$. The value of local equilibrium state (N_0, Z_0) is located in the vicinity of the lead valley with neutron and proton numbers around $N_0 = 128$ and $Z_0 = 82$ and the heavier local equilibrium state is located in the vicinity of the superheavy valley with neutron and proton numbers around $\overline{N_0} = N_T - N_0 = 166$ and $\overline{Z_0} = Z_T - Z_0 = 106$. Here $N_T = 152 + 142$ is the total neutron number and $Z_T = 98 + 90$ is the total proton number of the dinuclear system, respectively.

4.1.2.2 Reduced Curvature Parameter α

In Sec. 2.3, we have stated that the potential energy near the local equilibrium point (N_0, Z_0) can be parametrized in the form of a double parabola. Using the mean drift along the iso-scalar direction, we calculated the average value of the iso-scalar reduced curvature parameter, $\overline{\beta}$, related to each geometry. But, to analyze the potential energy along the iso-vector direction and calculate the average value of the reduced iso-vector curvature parameter, $\overline{\alpha}$, we need to choose a suitable neighboring system to ^{250}Cf $+$ ^{232}Th. The head-on collision of ^{240}Cf $+$ ^{246}Th system at $E_{\text{c.m.}} = 950.0$ MeV is chosen for this purpose. Since the charge asymmetry values of ^{240}Cf and ^{246}Th are $\delta(\text{Cf}) \approx 0.183$, and $\delta(\text{Th}) \approx 0.268$, it is expected that the mean drift should be mainly in iso-vector direction, towards the iso-scalar line. In Fig. 4.5, the time evolution of mean values of the neutron $N(t)$ and proton $Z(t)$ numbers of target-like fragments in ^{240}Cf $+$ ^{246}Th at $\ell_i = 0\hbar$ are shown [9].

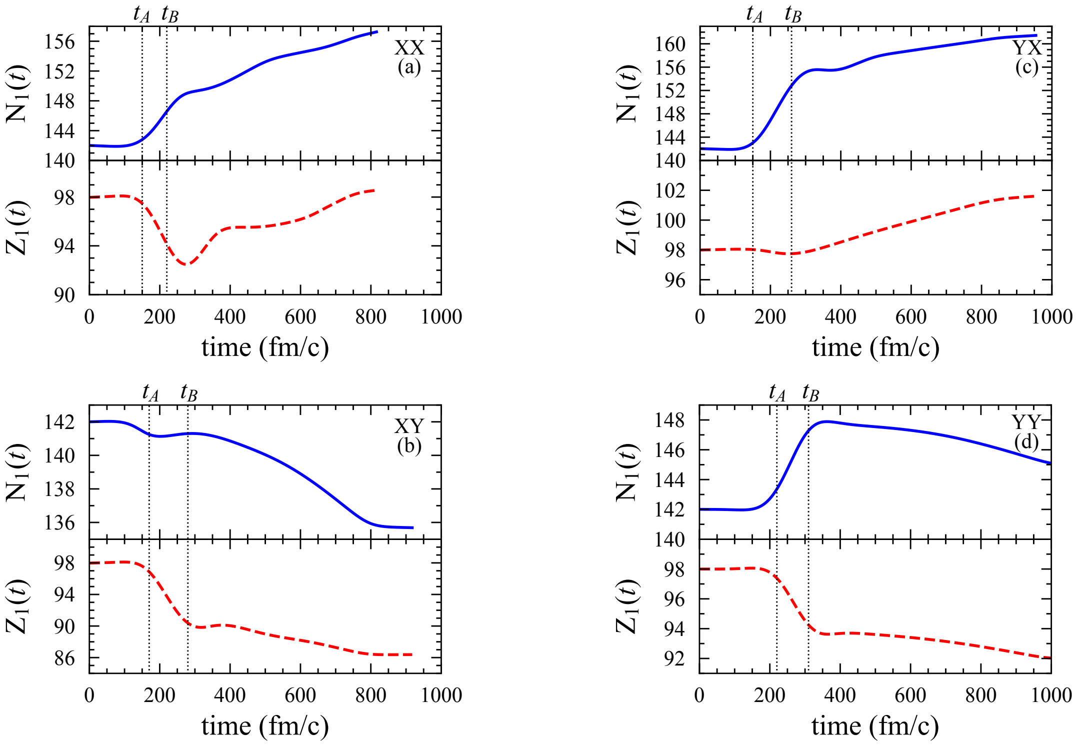

Figure 4.5: Same as Fig. 4.2 but for the ^{240}Cf $+$ ^{246}Th system.The labels t_A and t_B indicate the projection of the time intervals used to determine the parameter $\overline{\alpha}$. The figure was taken from Ref. [9].

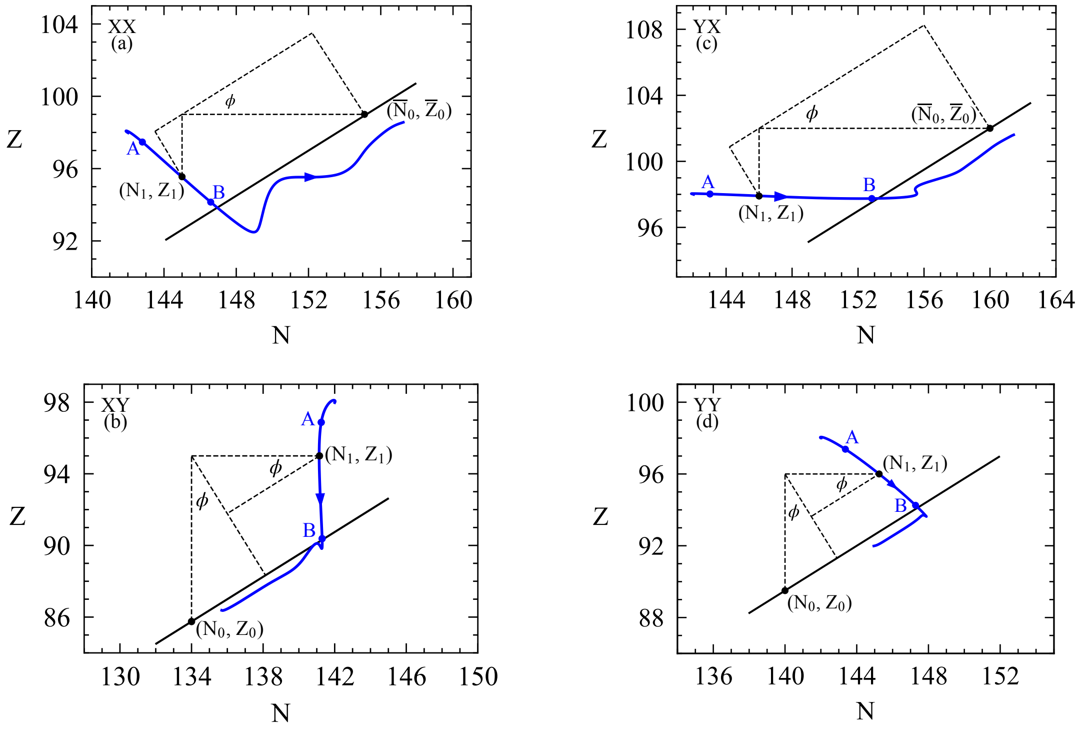

Figure 4.6: Same as Fig. 4.3 but for the ^{240}Cf + ^{246}Th system. The labels A and B indicate the projection of the time intervals used to determine the parameter $\overline{\alpha}$. The figure was taken from Ref. [9].

In Fig. 4.5, labels t_A and t_B denote the time intervals used for calculating the averaged value of iso-vector reduced curvature parameter, $\overline{\alpha}$, in each relative orientation. To project the change in neutron and proton numbers of collision partners into $N - Z$ plane, time dependence in $N_1(t)$ and $Z_1(t)$ is eliminated, and the resultant graph is given in Fig. 4.6. In Fig. 4.6, solid blue lines represent the mean drift path of Cf-like fragments, and thick black lines represent the iso-scalar line. As expected, throughout all four geometries, the drift is along the iso-vector direction, and one can use these reactions to extract information about the potential energy in a perpendicular direction to the stability valley. The quantal diffusion coefficients related to each different relative orientation in ^{240}Cf + ^{246}Th system at $E_{\text{c.m.}} = 950.0$ MeV are calculated. The results for each geometry are given in Fig. 4.7.

Firstly, in tip-tip (XX), side-tip (YX), and side-side (YY) geometries, during the initial phases of the collisions, Cf-like fragments lose protons and gain neutrons until TLF and PLF reach the same charge asymmetry values, which is roughly 0.22.Cf-like fragments then gain nucleons towards mass asymmetry in tip-tip (XX) and side-tip (YX) geometries. In side-side (YY) geometry, Cf-like fragments drift along the stability line towards the mass symmetry. In tip-side (XY) geometry, Cf-like fragments lose neutrons and protons to reach the same charge asymmetry value and then continue to lose nucleons along the stability valley towards mass symmetry. We must mention that the iso-scalar line, represented by a thick black line, is the same as Fig. 4.3. In tip-tip (XX) geometry, the $\overline{\alpha}$ parameter is calculated by using Eq. 2.24 between the time interva $t_A = 150$ fm/c and $t_B = 220$ fm/c to give value $\overline{\alpha}(XX) = 0.157$. In tip-side (XY), this time interval is taken as $t_A = 170$ fm/c and $t_B = 280$ fm/c to give value $\overline{\alpha}(XY) = 0.149$. In side-tip (YX), the interval for parameter $\overline{\alpha}$ is taken as $t_A = 150$ fm/c and $t_B = 260$ fm/c to give value $\overline{\alpha}(YX) = 0.115$. Finally, in side-side (YY) geometry, the time interval for $\overline{\alpha}$ is takes as $t_A = 220$ fm/c and $t_B = 310$ fm/c to give value $\overline{\alpha}(YY) = 0.111$. The value of local equilibrium states (N_0, Z_0), and $(\overline{N_0}, \overline{Z_0})$ are same as in Sec. 4.1.2.1.

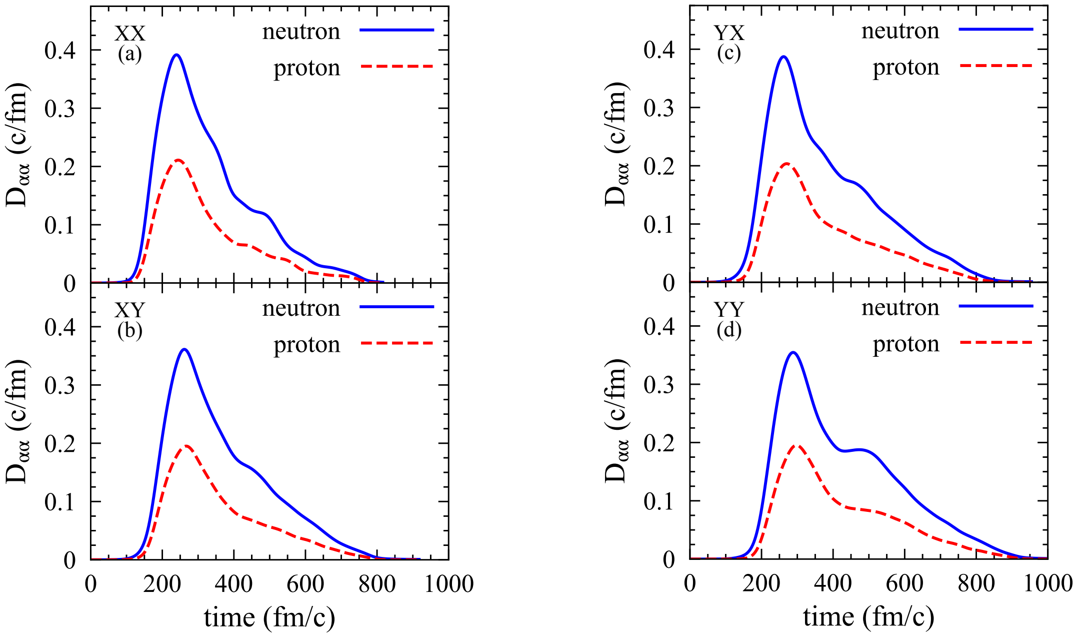

Figure 4.7: Same as Fig. 4.4 but for the ^{240}Cf + ^{246}Th system. The figure was taken from Ref. [9].

4.2 SMF results

4.2.1 Covariances of fragment charge and mass distributions

For all collisions with different initial relative orientations, Eqs.(2.8-2.10) are solved numerically for the proton, neutron variances, and mixed covariances by using the calculated reduced curvature parameters and the quantal diffusion coefficients. In Tab. 4.3, we share the asymptotic values for neutrons σ_{NN}, protons σ_{ZZ}, mixed σ_{NZ}, and mass σ_{AA} dispersions calculated for each initial angular momentum in tip-tip (XX), tip-side (XY), side-tip (YX), and side-side (YY) geometries. As an example, the calculated neutron, proton, and mixed variances as a function of time in ^{250}Cf $+$ ^{232}Th reaction in tip-tip (XX), tip-side (XY), side-tip (YX), and side-side (YY) geometries are shown in Fig 4.8. Throughout all geometries, we see that during the initial phase of the reaction, up to about $t \simeq 300$ fm/c, the magnitude of variances are in order as $\sigma_{NZ} < \sigma_{ZZ} < \sigma_{NN}$.

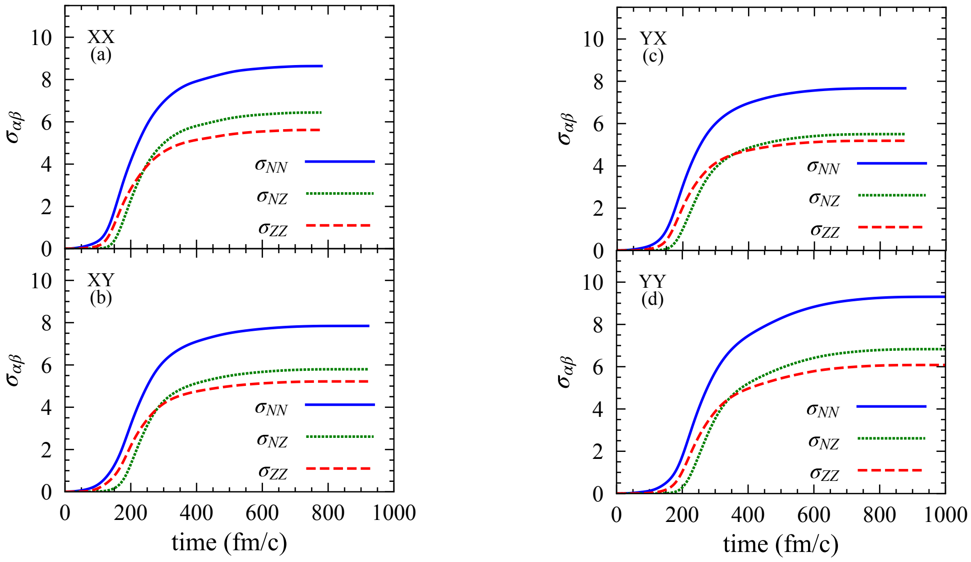

Figure 4.8: Neutron, proton, and mixed variances as a function of time for ^{250}Cf $+$ ^{232}Th system at $E_{\text{c.m.}} = 950.0$ MeV in tip-tip (XX), tip-side (XY), side-tip (YX), and side-side (YY) geometries. Solid blue, dashed red, and dotted green lines denote the neutron, σ_{NN}, proton, σ_{ZZ}, and mixed variances, σ_{NZ}, respectively. The figure was taken from Ref. [9].

Table 4.3: Results of the SMF calculations for the ^{250}Cf + ^{232}Th system at $E_{\text{c.m.}} = 950$ MeV in tip-tip (XX), tip-side (XY), side-tip (YX), and side-side (YY) geometries.

Tip-tip (XX)					Side-tip (YX)				
ℓ_i $(\hbar)$	σ_{NN}	σ_{ZZ}	σ_{NZ}	σ_{AA}	ℓ_i	σ_{NN}	σ_{ZZ}	σ_{NZ}	σ_{AA}
0	8.6	5.7	6.1	13.5	0	7.6	5.2	5.3	11.9
40	8.6	5.7	6.2	13.6	40	7.6	5.2	5.4	11.9
80	8.7	5.8	6.3	13.7	80	7.6	5.2	5.4	12.0
120	8.8	5.9	6.4	13.9	120	7.7	5.2	5.4	12.0
160	8.9	5.9	6.4	14.0	160	7.7	5.2	5.4	12.0
200	8.8	5.9	6.4	13.9	200	7.7	5.2	5.4	12.0
240	8.8	5.8	6.3	13.9	240	7.7	5.2	5.4	12.0
280	8.7	5.8	6.3	13.7	280	7.6	5.2	5.4	11.9
320	8.5	5.6	6.0	13.3	320	7.4	5.1	5.2	11.6
360	8.1	5.4	5.7	12.6	360	7.2	4.9	4.9	11.2
400	7.5	5.0	5.1	11.5	400	6.9	4.7	4.6	10.6
440	6.7	4.5	4.4	10.2	440	6.5	4.5	4.2	9.9
480	5.8	3.9	3.4	8.5	480	6.0	4.1	3.7	8.9
Tip-side (XY)					Side-side (YY)				
0	7.9	5.4	5.6	12.4	0	9.3	6.1	6.8	14.7
40	7.9	5.4	5.6	12.4	40	9.3	6.1	6.8	14.7
80	7.9	5.4	5.6	12.4	80	9.3	6.1	6.7	14.6
120	7.9	5.4	5.6	12.5	120	9.2	6.0	6.7	14.5
160	8.0	5.4	5.7	12.5	160	9.1	6.0	6.6	14.4
200	8.0	5.4	5.7	12.5	200	9.0	5.9	6.5	14.1
240	7.9	5.4	5.6	12.4	240	8.7	5.7	6.2	13.6
280	7.8	5.3	5.5	12.2	280	8.4	5.6	6.0	13.2
320	7.5	5.1	5.2	11.7	320	8.2	5.4	5.8	12.8
360	7.2	5.0	5.0	11.2	360	7.8	5.2	5.4	12.1
400	6.9	4.7	4.6	10.6	400	7.4	4.9	5.0	11.3
440	6.4	4.4	4.2	9.8	440	6.9	4.6	4.5	10.5
480	5.9	4.0	3.6	8.7	480	6.3	4.2	3.9	9.4

After that, the correlations evolve over time, changing the order to $\sigma_{ZZ} < \sigma_{NZ} < \sigma_{NN}$, demonstrating the importance of correlations arising from significant energy dissipation[1, 73, 9].

4.2.2 Primary Isotope Distribution

In this section, we continue with discussing the primary isotope distributions in ^{250}Cf+ ^{232}Th system at $E_{\text{c.m.}} = 950.0$ MeV. Since there is no experimental work for this system yet, we are unable to compare our results with the experimental data. To calculate primary isotope distribution, Eq. 2.30 and Eq. 2.32 are solved analytically with the initial angular momentum boundaries in Eq. 2.32 taken over the whole data-set, starting from $\ell_{\text{min}} = 0\hbar$ to $\ell_{\text{max}} = 480\hbar$. In Fig. 4.9, the total double cross-sections of primary fragments over the whole initial angular momentum range in $(N - Z)$ plane for tip-tip (XX), tip-side (XY), side-tip (YX), and side-side (YY) are shown. Here, the white crosses represent the initial reaction partners, ^{250}Cf and ^{232}Th, and

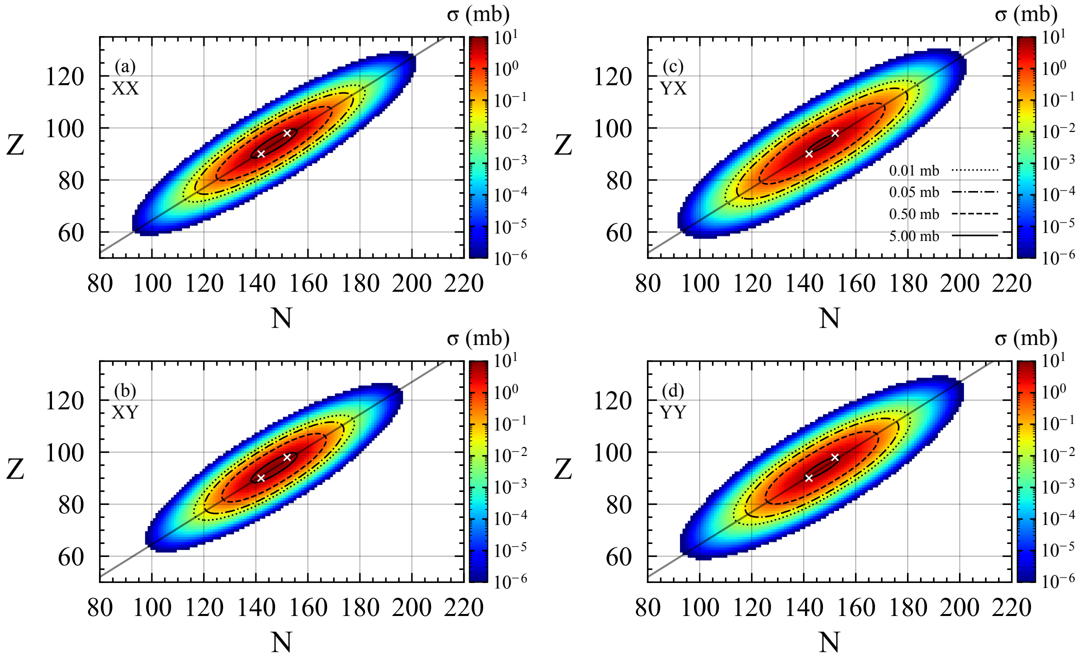

Figure 4.9: Primary isotope cross section in $(N - Z)$ plane for $^{250}\text{Cf} + {}^{232}\text{Th}$ system at $E_{\text{c.m.}} = 950.0$ MeV in tip-tip (XX), tip-side (XY), side-tip (YX), and side-side (YY) geometries. The figure was taken from Ref. [9].

the elliptic curves show the equal cross section values indicated by the legend inside the Fig. 4.9. Neutron-proton transfer correlations are strongly correlated when mixed dispersions have large values. The symmetry energy is primarily responsible for the high correlations. Consequently, in Fig. 4.9, the stability valley and the principal axes of equal cross-section elliptic curves align. Overall, the gross features of primary cross-sections are similar throughout all collision geometries in Fig. 4.9 [9]. This is mainly because the initial angular momentum range in Eq. 2.32 includes both deep-inelastic and elastic collisions. But still, due to the drift towards asymmetry direction, the magnitude of the cross-sections along the iso-scalar direction extends further towards the super heavy-island in tip-tip (XX), and side-tip (YX), collision geometries as compared to the other collision geometries.

Usually, in experimental works, the primary (and secondary) fragment detectors have a limited angular acceptance range. As a result of this, the initial angular momentum range in Eq. 2.32 should be determined by considering the scattering angles after the collision in the laboratory frame, as we have done in Sec. 3. As an extension to work in Ref.[9], we limit the initial angular momentum range in Eq. 2.32 such that the scattering angle in laboratory frame after the collision, θ_1^{lab}, in Tab. 4.3 lies within the range of $8° \leq \theta \leq 26°$. This further analysis aims to (i) show the effect of different relative orientations on cross-section and (ii) propose an experiment for this system. The resultant figure is given in Fig. 4.10. With the inclusion of this constraint, the effect of relative orientation on the primary isotope cross-section becomes clearer. In tip-tip (XX) geometry, we have already discussed that Swap Quasifission occurs, and Cf-like fragments tend to lose nucleons until they reach the thorium side. Similarly, Th-like fragments gain nucleons until they reach the californium side of the nuclear chart. Because of this trend, the primary isotope distribution is centered around the initial reaction partners, namely the ^{250}Cf and ^{232}Th. In tip-side (XY) geometry, we have a similar primary isotope distribution to tip-tip (XX), and the reason for this is that in this geometry, Quasifission is favored, and reaction partners tend to reach the mass symmetry. As a result of this, the TDHF mean values in Eq. 2.30 lie near the mass symmetry point, $^{241}\mathrm{Pu}$. In side-side (YY) geometry, the magnitude of primary isotope cross section near the mass symmetric region is smaller than the other geomteries due to (i) initial angular momentum range is smaller, (ii) dispersion values

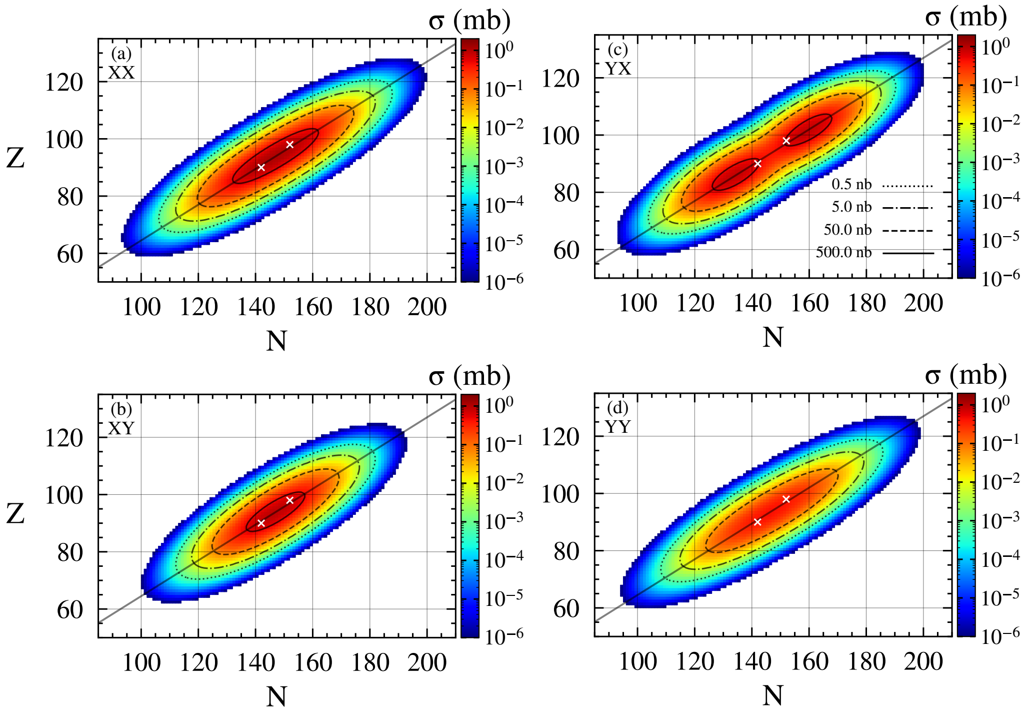

Figure 4.10: Same as Fig. 4.9 but the initial angular momentum range in Eq. 2.32 is decided with the constraints given in the text.

(σ_{NN}, σ_{ZZ}, σ_{NZ}) are larger in this geometry compared to the other geometries. The larger dispersion values widen the primary isotope cross-section in the $(N-Z)$ plane. Finally, in side-tip (YX) geometry, we can see the full extent of the effect of the Inverse Quasifission mechanism. The primary Cf-like isotopes are populated in the superheavy region, and Th-like fragments are populated near the doubly magic $^{208}\mathrm{Pb}$ nucleus. The primary isotope distribution in side-tip (YX) geometry is promising for synthesizing neutron-rich, heavy isotopes near the lead region and also synthesizing isotopes of superheavy elements with MNT reactions. Overall, magnitude of primary isotope cross sections in the ^{250}Cf + ^{232}Th system at $E_{\text{c.m.}} = 950.0$ MeV fall within experimentally detectable range. In the next section, we discuss how the overall cross sections will look after the de-excitation process, namely the secondary isotope distribution.

4.2.3 Secondary Isotope Distribution

In this section, we continue with discussing the secondary isotope distributions in ^{250}Cf + ^{232}Th system at $E_{\text{c.m.}} = 950.0$ MeV. Again, since there is no experimental work for this system yet, we are unable to compare our results with the experimental data. First, we calculate the secondary isotope distribution over the initial angular momentum range using Eq. 2.40. In Fig. 4.11, the total double cross-sections of secondary fragments over the whole initial angular momentum range in $(N - Z)$ plane for tip-tip (XX), tip-side (XY), side-tip (YX), and side-side (YY) geometries are shown. The gross features of secondary fragment distribution are similar throughout all geometries, and it can be seen that two significant factors shape the distribution. First, de-excitation of heavy primary fragments via light particle evaporation tends to continue until the isotopes reach the highly stable doubly magic $^{208}\mathrm{Pb}$ isotope, resulting in a peak in cross-section in all geometries near this region. Second, excited heavy fragments may also go under fission and then de-excite via light particle evaporation. This results in secondary fission fragments centered around the stability valley.

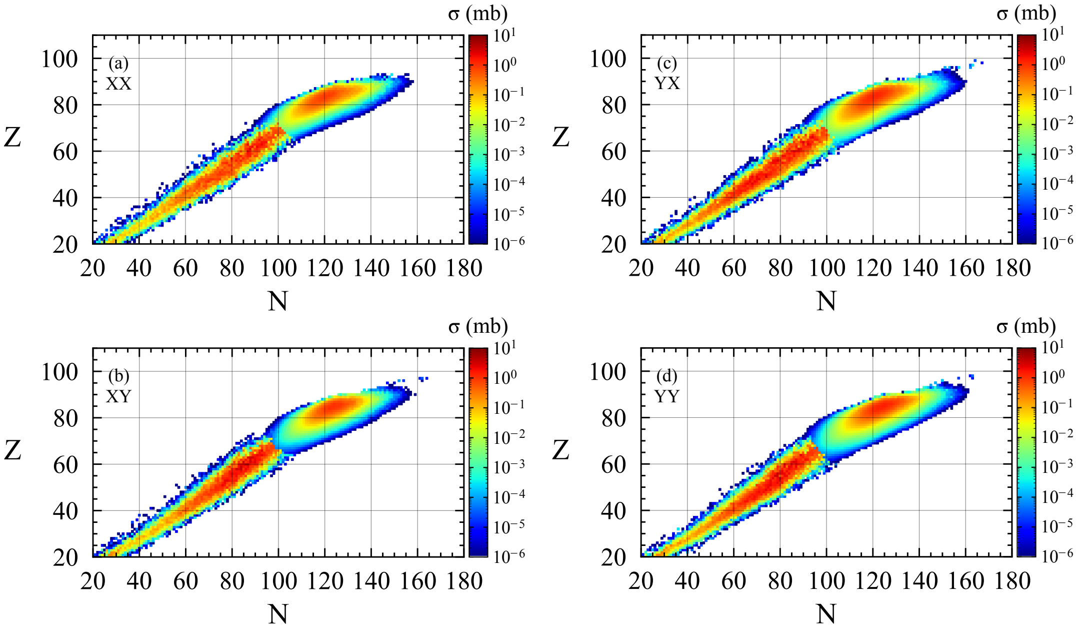

Figure 4.11: Secondary isotope cross section in $(N - Z)$ plane for ^{250}Cf + ^{232}Th system at $E_{\text{c.m.}} = 950.0$ MeV in tip-tip (XX), tip-side (XY), side-tip (YX), and side-side (YY) geometries. The figure was taken from Ref. [9].

To analyze the superheavy and neutron-rich heavy region in detail, we share the enlarged view of secondary cross sections in the $75 \leq Z \leq 104$ and $130 \leq N \leq 170$ region in Fig. 4.12. Throughout all the geometries, we can see that the secondary fragment distribution differs significantly from the primary fragment distribution. Still, both neutron-rich heavy isotopes and superheavy isotopes can be produced within experimentally detectable cross-sections in nanobarn units. One way to increase the secondary product cross-section in this system is to reduce the collision energy of the system. In this work, the collision energy with $E_{\text{c.m.}} = 950.0$ MeV is chosen. As we can see from the Tab. 4.1 and Tab. 4.2, the total kinetic energy (TKE) of the system after the collision is around 600 MeV, meaning excited primary fragments have around 350 MeV excitation energy in total in center of mass frame of the system. Within this energy scope, the primary fragments mostly go under either fission or sequential light fragment evaporation, and evaporation residue of neutron-rich heavy isotopes and isotopes of superheavy elements are greatly hindered. Similar to Sec. 4.2.2, we continue with further analyzing the secondary product cross-section

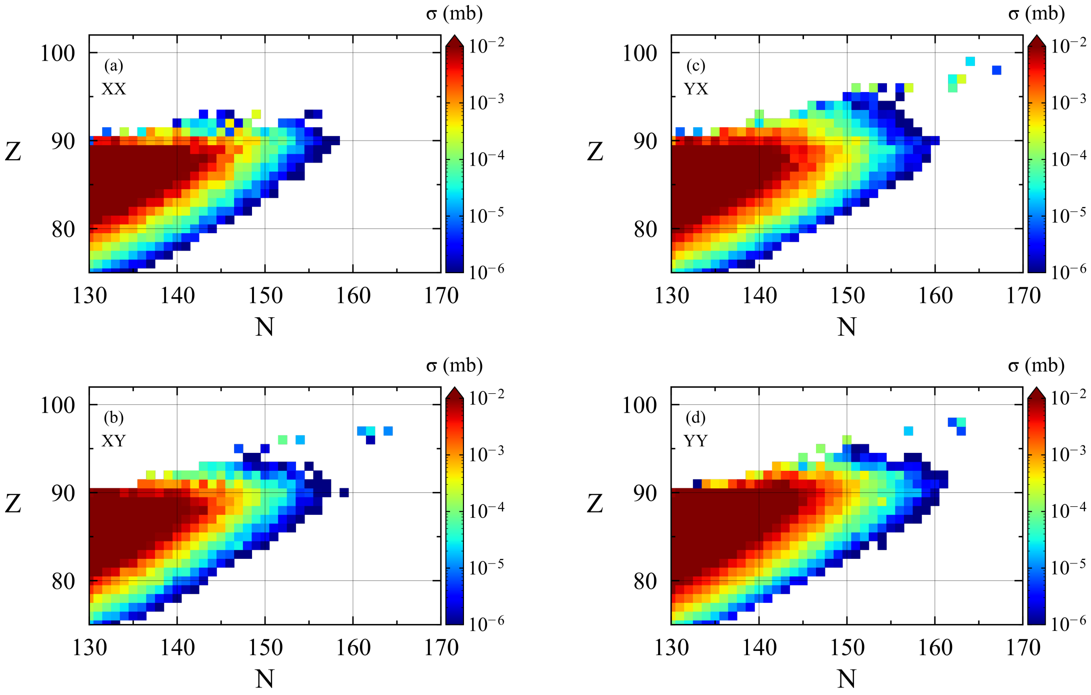

Figure 4.12: Enlarged view of secondary isotope cross section in $(N - Z)$ plane for ^{250}Cf + ^{232}Th system at $E_{\text{c.m.}} = 950.0$ MeV in tip-tip (XX), tip-side (XY), side-tip (YX), and side-side (YY) geometries. The figure was taken from Ref. [9].

with the same constrain that the scattering angle in the laboratory frame after the collision, $\theta_1^{\rm lab}$, lies within the range of $8^\circ \leq \theta_1^{\rm lab} \leq 26^\circ$. If we compare the primary fragment distribution in Fig. 4.10 with Fig. 4.13, we can see that the effect of relative orientation becomes less important in secondary product distribution. In the resultant Fig. 4.13, we share the enlarged view of the secondary isotope cross-section $(N-Z)$ plane with this constraint taken into account. If we compare the primary fragment distribution in Fig. 4.10 with Fig. 4.13, we can see that the effect of relative orientation becomes less important in secondary product distribution. Similar to the situation in the case where the cross-section calculation is done over the whole initial momentum range, we believe that the high excitation energy of the primary fragments is the main reason for this effect. Still, both Fig. 4.12 and Fig. 4.13 support the idea that multinucleon transfer reactions can be used as a mechanism to produce yet unknown neutron-rich heavy isotopes and neutron-rich superheavy elements.

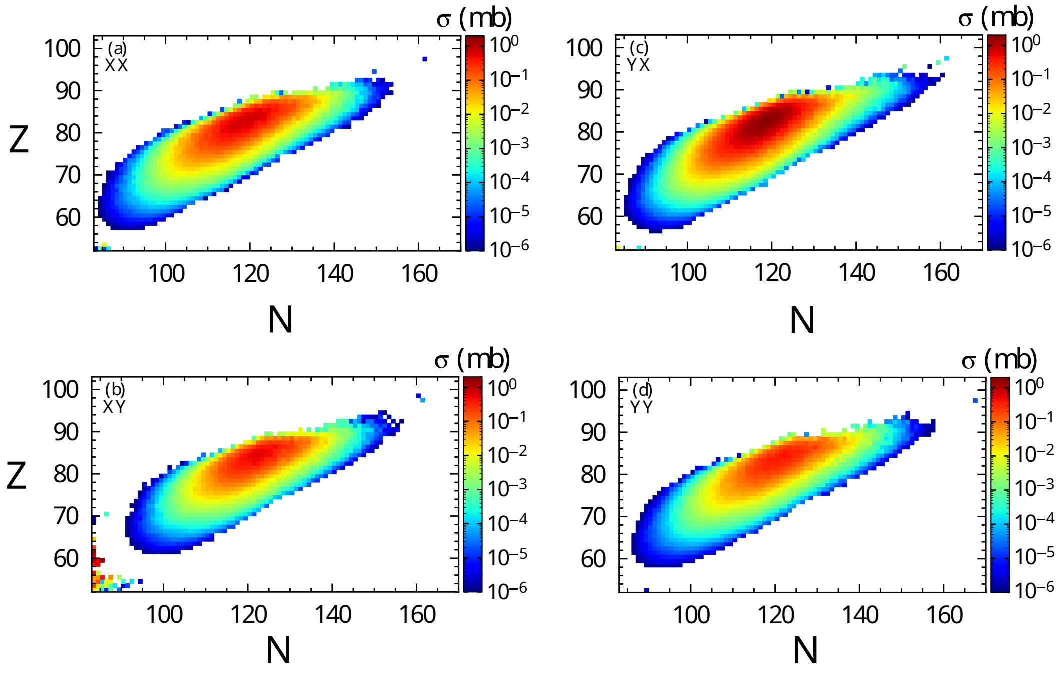

Figure 4.13: Same as Fig. 4.12 but the initial angular momentum range in Eq. 2.40 is decided with the constraints given in the text.

CHAPTER 5

CONCLUSION

The main aim of this work is to go beyond the mean-field description provided by TDHF theory within the SMF framework to study (i) the contributions from QF and FF mechanisms in MNT reactions and (ii) the effect of the relative orientation of reaction partners on primary and secondary product cross distributions in MNT reactions.

We have investigated QF and FF processes in heavy ion reactions at low energies just above the Coulomb barrier by employing the quantal diffusion approach based on the SMF framework to achieve these aims. The SMF approach incorporates mean-field fluctuations that align with the nonequilibrium statistical mechanics fluctuation-dissipation theorem, hence serving as an extension of the TDHF description.

The TDHF theory provides a deterministic description of collision dynamics by calculating a unique single-particle density matrix from an initial single Slater determinant. This results in a specific exit channel for a collision with a given charge and mass asymmetry. However, due to correlations, the initial state should be a superposition of Slater determinants, not a single one. The SMF approach represents this correlated initial state as an ensemble of single-particle density matrices with initial fluctuations. Each event in the ensemble evolves according to the TDHF equations with a self-consistent Hamiltonian of that event. Initial density matrix fluctuations follow Gaussian distributions, ensuring the ensemble's average dispersion of one-body observables matches the quantal mean-field expressions. With the help of the window plane and the geometric projection of collision dynamics, nucleon transfer is treated as a diffusion process instead of generating an ensemble of stochastically generated mean-field events. The neutron and proton numbers of the TLF fragments are chosen as the macroscopic variables of the linearized Langevin equation. The Fokker-Planck equation describes the primary fragment distribution function after the collision. The required quantities are the proton, neutron, and mixed dispersions to solve the joint probability distribution function for each initial angular momentum value. These dispersions are determined by using (i) the quantal diffusion coefficients, and (ii) the curvature of the potential energy surface around the local equilibrium value of the system. The occupied single-particle wave functions of the TDHF theory are used to estimate diffusion coefficients, which form the basis of generating fluctuations. The quantal diffusion coefficients do not involve any adjustable parameters, and they incorporate quantal effects from Pauli blocking and shell structure. The potential energy around the local equilibrium value is approximated in terms of two parabolic forms, in which the diffusion coefficients and the mean drift path of the TDHF solutions determine their values. We emphasize that the SMF theory does not involve any adjustable parameters other than the standard parameters of energy density functional employed in TDHF theory. Finally, the de-excitation of primary fragments after the collision and the FF distribution of the compound nucleus is determined by using the Monte Carlo code GEMINI++.

To analyze the contributions from FF and QF mechanisms in multinucleon transfer reactions, we have studied the primary mass distribution in $^{48}\mathrm{Ca} + {}^{244}\mathrm{Pu}$ reaction at $\mathrm{E_{c.m.}} = 203.2$ MeV and $^{86}\mathrm{Kr} + {}^{198}\mathrm{Pt}$ reaction at $\mathrm{E_{c.m.}} = 324.2$ MeV, and compared our results with the experimental data available [7, 6]. The TDHF calculations in $^{48}\mathrm{Ca} + {}^{244}\mathrm{Pu}$ system shows that nucleon drift towards mass symmetry is favored. Final values of charge and mass numbers of Pu-like fragments revolve around the doubly magic highly stable $^{208}\mathrm{Pb}$ nucleus. The averaged values of reduced curvature parameters are found for both systems using the calculated quantal diffusion coefficients and the mean values of neutron and proton numbers of TLF. The joint probability distribution function is solved using the proton, neutron, and mixed dispersions, along with the mean values of neutron and proton numbers of PLF and TLF found in the TDHF solutions. The contributions from the QF mechanism are calculated within the SMF framework, and contributions from the FF mechanism are analyzed using the GEMINI++ code. Combined together, primary mass distribution in $^{48}\mathrm{Ca} + {}^{244}\mathrm{Pu}$ reaction at $\mathrm{E_{c.m.}} = 203.2$ MeV and $^{86}\mathrm{Kr} + {}^{198}\mathrm{Pt}$ reaction at $\mathrm{E_{c.m.}} = 324.2$ MeV are calculated, and the contributions from two different mechanisms are compared and discussed. The observed overall agreement between the experimental data and the fully quantal SMF results highlights the effectiveness of the quantal diffusion approach based on the SMF theory.

To analyze the effect of different relative orientation of deformed reaction partners on primary and secondary isotope distribution, ^{250}Cf + ^{232}Th system at $E_{\text{c.m.}} = 950.0$ MeV is analyzed within the framework of SMF approach. The TDHF and SMF calculations are performed over a broad range of initial angular momenta in tip-tip(XX), tip-side(XY), side-tip(YX), and side-side(YY) collision geometries. The mean-field results of TDHF differ significantly in different relative geometries. Quasifission with the drift towards mass symmetry is observed in side-side(YY) geometry, while Inverse Quasifission is observed in collisions with small angular momenta in tip-tip(XX) and tip-side(XY) geometries. In side-tip(YX) geometry, it is observed that a large number of nucleons are transferred from lighter Th-like fragments to heavier Cf-like fragments. This type of reaction, usually called Inverse Quasifission, is optimal for producing yet-unknown-neutron-rich heavy isotopes and neutron-rich superheavy elements. The averaged values of reduced curvature parameters are found separately for each relative orientation using the calculated quantal diffusion coefficients and the mean values of neutron and proton numbers of TLF. The joint probability distribution function is solved using the proton, neutron, and mixed dispersions, along with the mean values of neutron and proton numbers of PLF and TLF found in the TDHF solutions. It is observed that the gross properties of the primary isotope distribution are similar throughout all geometries when primary isotope distribution calculations are performed over the whole initial angular momentum range. To (i) observe the effect of different geometries on primary product distribution in detail, and (ii) propose an experiment for this system, the initial angular momentum range in cross-section calculations is chosen with the constrain that the scattering angle of the Cf-like fragments after the collision satisfies, $8^\circ \leq \theta_1^{\text{lab}} \leq 26^\circ$. With this constrain, it is observed that throughout all geometries, the primary fragment cross-section of neutron-rich heavy isotopes and neutron-rich superheavy elements fall within the experimentally detectable range, especially in the side-tip(YX) geometry. Similar to primary isotope calculations, the secondary isotope cross-section calculations are performed over the initial angular momentum range and with the same constraint applied. In both cases, the gross properties of secondary product cross sections in the $(N - Z)$ plane are similar throughout all geometries. We believe that the high excitation energy of primary isotopes may cause this result.

The quantal diffusion approach based on SMF theory is a valuable framework for studying QF reactions in heavy-ion reactions at energies around the Coulomb barrier. As an extension to the TDHF theory, it is possible to calculate the primary isotope distribution after the collision within this framework. Furthermore, with the inclusion of statistical de-excitation code GEMINI++, the theory is capable of calculating the secondary isotope distribution and the FF fragment distribution of compound nuclei, allowing one to analyze the whole product distribution. The description includes the entire collision geometry, quantal effects due to shell structure, and the Pauli exclusion principle. Finally, We emphasize that the SMF theory does not involve any adjustable parameters other than the standard parameters of energy density functional employed in TDHF theory. As a final remark, gaining a microscopic grasp of reaction mechanisms and predicting the outcomes of reactions that haven't been performed yet are essential objectives for expanding the known nuclear chart.

REFERENCES

[1] M. Arik, S. Ayik, O. Yilmaz, and A. S. Umar, "Description of the multinucleon transfer mechanism for $^{48}\mathrm{Ca} +^{244} \mathrm{Pu}$ and $^{86}\mathrm{Kr} +^{198} \mathrm{Pt}$ reactions in a quantal transport approach," *Phys. Rev. C*, vol. 108, p. 064604, 2023.

[2] G. G. Adamian, N. V. Antonenko, A. Diaz-Torres, and S. Heinz, "How to extend the chart of nuclides?," *Eur. Phys. J. A*, vol. 56, p. 47, 2020.

[3] A. Nasirov, K. Kim, G. Mandaglio, G. Giardina, A. Muminov, and Y. Kim, "Main restrictions in the synthesis of new superheavy elements: Quasifission and/or fusion fission," *The European Physical Journal A 2013 49:11*, vol. 49, pp. 1–14, 2013.

[4] S. Ayik, M. Arik, O. Yilmaz, and A. S. Umar, "Supplemental online material for: Description of the multinucleon transfer mechanism for $^{48}\mathrm{Ca} +^{244} \mathrm{Pu}$ and $^{86}\mathrm{Kr} +^{198} \mathrm{Pt}$ reactions in a quantal transport approach," *Phys. Rev. C*, vol. 108, p. 064604, Dec 2023.

[5] E. M. Kozulin, G. N. Knyazheva, I. M. Itkis, M. G. Itkis, A. A. Bogachev, E. V. Chernysheva, L. Krupa, F. Hanappe, O. Dorvaux, L. Stuttgé, W. H. Trzaska, C. Schmitt, and G. Chubarian, "Fusion-fission and quasifission of superheavy systems with Z=110-116 formed in ^{48}Ca-induced reactions," *Phys. Rev. C*, vol. 90, p. 054608, 2014.

[6] A. Sen, T. K. Ghosh, E. M. Kozulin, I. M. Itkis, G. N. Knyazheva, K. V. Novikov, S. Bhattacharya, K. Banerjee, and C. Bhattacharya, "Quasifission in $^{84,86}\mathrm{Kr}$-induced reactions populating superheavy elements," *Phys. Rev. C*, vol. 105, p. 014627, 2022.

[7] E. M. Kozulin, G. N. Knyazheva, T. K. Ghosh, A. Sen, I. M. Itkis, M. G. Itkis, K. V. Novikov, I. N. Diatlov, I. V. Pchelintsev, C. Bhattacharya, S. Bhattacharya, K. Banerjee, E. O. Saveleva, and I. V. Vorobiev, "Fission and quasi-

fission of the composite system $\mathrm{Z} = 114$ formed in heavy-ion reactions at energies near the Coulomb barrier," *Phys. Rev. C*, vol. 99, p. 014616, 2019.

[8] R. Charity, "GEMINI: A code to simulate the decay of a compound nucleus by a series of binary decays," tech. rep., International Atomic Energy Agency (IAEA), 2008. INDC(NDS)–0530.

[9] S. Ayik, M. Arik, O. Yilmaz, B. Yilmaz, and A. S. Umar, "Multinucleon transfer mechanism in $^{250}\mathrm{Cf} +^{232} \mathrm{Th}$ collisions using the quantal transport description based on the stochastic mean-field approach," *Phys. Rev. C*, vol. 107, p. 014609, 2023.

[10] E. Rutherford, "LXXIX. The scattering of α and β particles by matter and the structure of the atom," *Philos. Mag. Ser. 6*, vol. 21, pp. 669–688, 1911.

[11] G. Fea, "Tabelle riassuntive e bibliografia delle trasmutazioni artificiali," *Il Nuovo Cimento*, vol. 12, pp. 368—-406, 1935.

[12] H. Koura, T. Tachibana, M. Uno, and M. Yamada, "Nuclidic mass formula on a spherical basis with an improved even-odd term," *Progress of Theoretical Physics*, vol. 113, pp. 305–325, 2005.

[13] W. Nazarewicz, "The limits of nuclear mass and charge," *Nat. Phys.*, vol. 14, pp. 537–541, 2018.

[14] A. Sobiczewski, F. A. Gareev, and B. N. Kalinkin, "Closed shells for Z$>$82 and N$>$126 in a diffuse potential well," *Phys. Lett.*, vol. 22, pp. 500–502, 1966.

[15] K. Rutz, M. Bender, T. Bürvenich, T. Schilling, P.-G. Reinhard, J. A. Maruhn, and W. Greiner, "Superheavy nuclei in self-consistent nuclear calculations," *Phys. Rev. C*, vol. 56, pp. 238–243, 1997.

[16] M. Bender, K. Rutz, P.-G. Reinhard, J. A. Maruhn, and W. Greiner, "Shell structure of superheavy nuclei in self-consistent mean-field models," *Phys. Rev. C*, vol. 60, p. 034304, 1999.

[17] A. Staszczak, A. Baran, and W. Nazarewicz, "Spontaneous fission modes and lifetimes of superheavy elements in the nuclear density functional theory," *Phys. Rev. C*, vol. 87, p. 024320, 2013.

[18] S. Ćwiok, P.-H. Heenen, and W. Nazarewicz, “Shape coexistence and triaxiality in the superheavy nuclei,” *Nature*, vol. 433, pp. 705–709, 2005.

[19] Yu. Ts.. Oganessian, V. K. Utyonkov, Y. V. Lobanov, F. S. Abdullin, A. N. Polyakov, I. V. Shirokovsky, Y. S. Tsyganov, G. G. Gulbekian, S. L. Bogomolov, B. N. Gikal, A. N. Mezentsev, S. Iliev, V. G. Subbotin, A. M. Sukhov, A. A. Voinov, G. V. Buklanov, K. Subotic, V. I. Zagrebaev, M. G. Itkis, J. B. Patin, K. J. Moody, J. F. Wild, M. A. Stoyer, N. J. Stoyer, D. A. Shaughnessy, J. M. Kenneally, and R. W. Lougheed, “Measurements of cross sections for the fusion-evaporation reactions $^{244}\mathrm{Pu}(^{48}\mathrm{Ca}, xn)^{292-x}114$ and $^{245}\mathrm{Cm}(^{48}\mathrm{Ca}, xn)^{293-x}116$,” *Phys. Rev. C*, vol. 69, p. 054607, 2004.

[20] Yu. Ts. Oganessian, V. K. Utyonkov, Yu. V. Lobanov, F. Sh. Abdullin, A. N. Polyakov, R. N. Sagaidak, I. V. Shirokovsky, Yu. S. Tsyganov, A. A. Voinov, G. G. Gulbekian, S. L. Bogomolov, B. N. Gikal, A. N. Mezentsev, S. Iliev, V. G. Subbotin, A. M. Sukhov, K. Subotic, V. I. Zagrebaev, G. K. Vostokin, M. G. Itkis, K. J. Moody, J. B. Patin, D. A. Shaughnessy, M. A. Stoyer, N. J. Stoyer, P. A. Wilk, J. M. Kenneally, J. H. Landrum, J. F. Wild, and R. W. Lougheed, “Synthesis of the isotopes of elements 118 and 116 in the $^{249}\mathrm{Cf}$ and $^{245}\mathrm{Cm} + {}^{48}\mathrm{Ca}$ fusion reactions,” *Phys. Rev. C*, vol. 74, p. 044602, 2006.

[21] Yuri Oganessian, “Heaviest nuclei from ^{48}Ca-induced reactions,” *J. Phys. G: Nucl. Part. Phys.*, vol. 34, pp. R165–R242, 2007.

[22] Yu. Ts. Oganessian, F. Sh. Abdullin, P. D. Bailey, D. E. Benker, M. E. Bennett, S. N. Dmitriev, J. G. Ezold, J. H. Hamilton, R. A. Henderson, M. G. Itkis, Yu. V. Lobanov, A. N. Mezentsev, K. J. Moody, S. L. Nelson, A. N. Polyakov, C. E. Porter, A. V. Ramayya, F. D. Riley, J. B. Roberto, M. A. Ryabinin, K. P. Rykaczewski, R. N. Sagaidak, D. A. Shaughnessy, I. V. Shirokovsky, M. A. Stoyer, V. G. Subbotin, R. Sudowe, A. M. Sukhov, Yu. S. Tsyganov, V. K. Utyonkov, A. A. Voinov, G. K. Vostokin, and P. A. Wilk, “Synthesis of a New Element with Atomic Number $Z = 117$,” *Phys. Rev. Lett.*, vol. 104, p. 142502, 2010.

[23] Yu. Ts. Oganessian, F. Sh. Abdullin, P. D. Bailey, D. E. Benker, M. E. Bennett, S. N. Dmitriev, J. G. Ezold, J. H. Hamilton, R. A. Henderson, M. G. Itkis, Yu.

V. Lobanov, A. N. Mezentsev, K. J. Moody, S. L. Nelson, A. N. Polyakov, C. E. Porter, A. V. Ramayya, F. D. Riley, J. B. Roberto, M. A. Ryabinin, K. P. Rykaczewski, R. N. Sagaidak, D. A. Shaughnessy, I. V. Shirokovsky, M. A. Stoyer, V. G. Subbotin, R. Sudowe, A. M. Sukhov, R. Taylor, Yu. S. Tsyganov, V. K. Utyonkov, A. A. Voinov, G. K. Vostokin, and P. A. Wilk, "Eleven new heaviest isotopes of elements Z = 105 to Z = 117 identified among the products of $^{249}\mathrm{Bk} + {}^{48}\mathrm{Ca}$ reactions," *Phys. Rev. C*, vol. 83, p. 054315, 2011.

[24] Yu. Ts. Oganessian, F. Sh. Abdullin, C. Alexander, J. Binder, R. A. Boll, S. N. Dmitriev, J. Ezold, K. Felker, J. M. Gostic, R. K. Grzywacz, J. H. Hamilton, R. A. Henderson, M. G. Itkis, K. Miernik, D. Miller, K. J. Moody, A. N. Polyakov, A. V. Ramayya, J. B. Roberto, M. A. Ryabinin, K. P. Rykaczewski, R. N. Sagaidak, D. A. Shaughnessy, I. V. Shirokovsky, M. V. Shumeiko, M. A. Stoyer, N. J. Stoyer, V. G. Subbotin, A. M. Sukhov, Yu. S. Tsyganov, V. K. Utyonkov, A. A. Voinov, and G. K. Vostokin, "Production and Decay of the Heaviest Nuclei $^{293,294}117$ and $^{294}118$," *Phys. Rev. Lett.*, vol. 109, p. 162501, 2012.

[25] J. Khuyagbaatar, A. Yakushev, Ch. E. Düllmann, D. Ackermann, L.-L. Andersson, M. Asai, M. Block, R. A. Boll, H. Brand, D. M. Cox, M. Dasgupta, X. Derkx, A. Di Nitto, K. Eberhardt, J. Even, M. Evers, C. Fahlander, U. Forsberg, J. M. Gates, N. Gharibyan, P. Golubev, K. E. Gregorich, J. H. Hamilton, W. Hartmann, R.-D. Herzberg, F. P. Heßberger, D. J. Hinde, J. Hoffmann, R. Hollinger, A. Hübner, E. Jäger, B. Kindler, J. V. Kratz, J. Krier, N. Kurz, M. Laatiaoui, S. Lahiri, R. Lang, B. Lommel, M. Maiti, K. Miernik, S. Minami, A. Mistry, C. Mokry, H. Nitsche, J. P. Omtvedt, G. K. Pang, P. Papadakis, D. Renisch, J. Roberto, D. Rudolph, J. Runke, K. P. Rykaczewski, L. G. Sarmiento, M. Schädel, B. Schausten, A. Semchenkov, D. A. Shaughnessy, P. Steinegger, J. Steiner, E. E. Tereshatov, P. Thörle-Pospiech, K. Tinschert, T. Torres De Heidenreich, N. Trautmann, A. Türler, J. Uusitalo, D. E. Ward, M. Wegrzecki, N. Wiehl, S. M. Van Cleve, and V. Yakusheva, "$^{48}\mathrm{Ca} + {}^{249}\mathrm{Bk}$ Fusion Reaction Leading to Element $Z = 117$: Long-Lived α-Decaying $^{270}\mathrm{Db}$ and Discovery of $^{266}\mathrm{Lr}$," *Phys. Rev. Lett.*, vol. 112, p. 172501, 2014.

[26] Yu. Ts. Oganessian and V. K. Utyonkov, "Superheavy nuclei from $^{48}\mathrm{Ca}$-

induced reactions," *Nucl. Phys. A*, vol. 944, pp. 62–98, 2015.

[27] Itkis, M. G., Knyazheva, G. N., Itkis, I. M., and Kozulin, E. M., "Experimental investigation of cross sections for the production of heavy and superheavy nuclei," *Eur. Phys. J. A*, vol. 58, p. 178, 2022.

[28] S. Hofmann and G. Münzenberg, "The discovery of the heaviest elements," *Rev. Mod. Phys.*, vol. 72, pp. 733–767, 2000.

[29] S. Hofmann, F. P. Heßberger, D. Ackermann, G. Münzenberg, S. Antalic, P. Cagarda, B. Kindler, J. Kojouharova, M. Leino, B. Lommel, R. Mann, A. G. Popeko, S. Reshitko, S. Śaro, J. Uusitalo, and A. V. Yeremin, "New results on elements 111 and 112," *Eur. Phys. J. A*, vol. 14, pp. 147–157, 2002.

[30] K. Morita, K. Morimoto, D. Kaji, T. Akiyama, S. ichi Goto, H. Haba, E. Ideguchi, R. Kanungo, K. Katori, H. Koura, H. Kudo, T. Ohnishi, A. Ozawa, T. Suda, K. Sueki, H. Xu, T. Yamaguchi, A. Yoneda, A. Yoshida, and Y. Zhao, "Experiment on the Synthesis of Element 113 in the Reaction $^{209}\mathrm{Bi}(^{70}\mathrm{Zn}, n)^{278}113$," *J. Phys. Soc. Japan*, vol. 73, pp. 2593–2596, 2004.

[31] A. Chatillon, Ch. Theisen, P. T. Greenlees, G. Auger, J. E. Bastin, E. Bouchez, B. Bouriquet, J. M. Casandjian, R. Cee, E. Clément, R. Dayras, G. de France, R. de Toureil, S. Eeckhaudt, A. Göergen, T. Grahn, S. Grévy, K. Hauschild, R.-D. Herzberg, P. J. C. Ikin, G. D. Jones, P. Jones, R. Julin, S. Juutinen, H. Kettunen, A. Korichi, W. Korten, Y. Le Coz, M. Leino, A. Lopez-Martens, S. M. Lukyanov, Yu. E. Penionzhkevich, J. Perkowski, A. Pritchard, P. Rahkila, M. Rejmund, J. Saren, C. Scholey, S. Siem, M. G. Saint-Laurent, C. Simenel, Yu. G. Sobolev, Ch. Stodel, J. Uusitalo, A. Villari, M. Bender, P. Bonche, and P.-H. Heenen, "Spectroscopy and single-particle structure of the odd-Z heavy elements ^{255}Lr, ^{251}Md and ^{247}Es," *Eur. Phys. J. A*, vol. 30, pp. 397–411, 2006.

[32] R.-D. Herzberg, P. T. Greenlees, P. A. Butler, G. D. Jones, M. Venhart, I. G. Darby, S. Eeckhaudt, K. Eskola, T. Grahn, C. Gray-Jones, F. P. Heßberger, P. Jones, R. Julin, S. Juutinen, S. Ketelhut, W. Korten, M. Leino, A.-P. Leppanen, S. Moon, M. Nyman, R. D. Page, J. Pakarinen, A. Pritchard, P. Rahkila, J. Saren, C. Scholey, A. Steer, Y. Sun, Ch. Theisen, and J. Uusitalo, "Nuclear

isomers in superheavy elements as stepping stones towards the island of stability," *Nature*, vol. 442, pp. 896–899, 2006.

[33] Heinz, S. and Devaraja, H. M., "Nucleosynthesis in multinucleon transfer reactions," *Eur. Phys. J. A*, vol. 58, p. 114, 2022.

[34] K. Sapotta, R. Bass, V. Hartmann, H. Noll, R. E. Renfordt, and K. Stelzer, "Mass and charge transfer in the heavy ion reactions $^{208}\mathrm{Ni}$ and $^{208}\mathrm{Ni}$," *Phys. Rev. C*, vol. 31, pp. 1297–1314, 1985.

[35] K. E. Rehm, A. M. v. Berg, J. J. Kolata, D. G. Kovar, W. Kutschera, G. Rosner, G. S. F. Stephans, and J. L. Yntema, "Transition from quasi-elastic to deep-inelastic reactions in the $^{48}\mathrm{Ti}+^{208}\mathrm{Pb}$ system," *Phys. Rev. C*, vol. 37, pp. 2629–2646, 1988.

[36] W. von Oertzen, "Cold multi-nucleon transfer between heavy nuclei and the synthesis of new elements," *Z. Phys. A*, vol. 342, pp. 177–182, 1992.

[37] U. W. Scherer, W. Brüchle, M. Brügger, C. Frink, H. Gäggeler, G. Herrmann, J. V. Kratz, K. J. Moody, M. Schädel, K. Sümmerer, N. Trautmann, and G. Wirth, "Reactions of40ar with233u,235u, and238u at the barrier," *Zeitschrift für Physik A Atomic Nuclei*, vol. 335, pp. 421–430, 1990.

[38] J. Speer, W. von Oertzen, D. Schüll, M. Wilpert, H. G. Bohlen, B. Gebauer, B. Kohlmeyer, and F. Pühlhofer, "Cold multi-proton-pair transfer between $^{144}\mathrm{Sm}$ and $^{208}\mathrm{Pb}$," *Physics Letters B*, vol. 259, pp. 422–426, 1991.

[39] S. A. Kalandarov, G. G. Adamian, N. V. Antonenko, H. M. Devaraja, and S. Heinz, "Production of neutron deficient isotopes in the multinucleon transfer reaction $^{48}\mathrm{Ca}$ $(E_{\mathrm{lab}} = 5.63\ \mathrm{MeV/nucleon}) + {}^{248}\mathrm{Cm}$," *Phys. Rev. C*, vol. 102, p. 024612, 2020.

[40] C. L. Jiang, K. E. Rehm, H. Esbensen, D. J. Blumenthal, B. Crowell, J. Gehring, B. Glagola, J. P. Schiffer, and A. H. Wuosmaa, "Multineutron transfer in $^{58}\mathrm{Ni} + {}^{124}\mathrm{Sn}$ collisions at sub-barrier energies," *Phys. Rev. C*, vol. 57, pp. 2393–2400, 1998.

[41] L. Corradi, S. J. Skorka, U. Lenz, K. E. G. Löbner, P. R. Pascholati, U. Quade, K. Rudolph, W. Schomburg, M. Steinmayer, H. G. Thies, G. Montagnoli, D. R.

Napoli, A. M. Stefanini, A. Tivelli, S. Beghini, F. Scarlassara, C. Signorini, and F. Soramel, “Near-barrier transfer and fusion of the systems $^{33}\mathrm{S} + {}^{90,91,92}\mathrm{Zr}$,” *Z. Phys. A*, vol. 335, pp. 55–72, 1990.

[42] L. Corradi, J. H. He, D. Ackermann, A. M. Stefanini, A. Pisent, S. Beghini, G. Montagnoli, F. Scarlassara, G. F. Segato, G. Pollarolo, C. H. Dasso, and A. Winther, “Multinucleon transfer reactions in $^{40}\mathrm{Ca} + {}^{124}\mathrm{Sn}$,” *Phys. Rev. C*, vol. 54, pp. 201–205, 1996.

[43] L. Corradi, A. M. Stefanini, J. H. He, S. Beghini, G. Montagnoli, F. Scarlassara, G. F. Segato, G. Pollarolo, and C. H. Dasso, “Evidence of complex degrees of freedom in multinucleon transfer reactions of $^{48}\mathrm{Ca} + {}^{124}\mathrm{Sn}$,” *Phys. Rev. C*, vol. 56, pp. 938–941, 1997.

[44] S. Szilner, L. Corradi, G. Pollarolo, S. Beghini, B. R. Behera, E. Fioretto, A. Gadea, F. Haas, A. Latina, G. Montagnoli, F. Scarlassara, A. M. Stefanini, M. Trotta, A. M. Vinodkumar, and Y. Wu, “Multinucleon transfer processes in $^{40}\mathrm{Ca} + {}^{208}\mathrm{Pb}$,” *Phys. Rev. C*, vol. 71, p. 044610, 2005.

[45] E. M. Kozulin, G. N. Knyazheva, I. M. Itkis, M. G. Itkis, A. A. Bogachev, L. Krupa, T. A. Loktev, S. V. Smirnov, V. I. Zagrebaev, J. Äystö, W. H. Trzaska, V. A. Rubchenya, E. Vardaci, A. M. Stefanini, M. Cinausero, L. Corradi, E. Fioretto, P. Mason, G. F. Prete, R. Silvestri, S. Beghini, G. Montagnoli, F. Scarlassara, F. Hanappe, S. V. Khlebnikov, J. Kliman, A. Brondi, A. Nitto, R. Moro, N. Gelli, and S. Szilner, “Investigation of the reaction $^{64}\mathrm{Ni} + {}^{238}\mathrm{U}$ being an option of synthesizing element 120,” *Phys. Lett. B*, vol. 686, pp. 227–232, 2010.

[46] E. M. Kozulin, E. Vardaci, G. N. Knyazheva, A. A. Bogachev, S. N. Dmitriev, I. M. Itkis, M. G. Itkis, A. G. Knyazev, T. A. Loktev, K. V. Novikov, E. A. Razinkov, O. V. Rudakov, S. V. Smirnov, W. Trzaska, and V. I. Zagrebaev, “Mass distributions of the system $^{136}\mathrm{Xe} + {}^{208}\mathrm{Pb}$ at laboratory energies around the Coulomb barrier: A candidate reaction for the production of neutron–rich nuclei at $N = 126$,” *Phys. Rev. C*, vol. 86, p. 044611, 2012.

[47] E. M. Kozulin, G. N. Knyazheva, S. N. Dmitriev, I. M. Itkis, M. G. Itkis, T. A. Loktev, K. V. Novikov, A. N. Baranov, W. H. Trzaska, E. Vardaci, S. Heinz,

O. Beliuskina, and S. V. Khlebnikov, “Shell effects in damped collisions of $^{88}\mathrm{Sr}$ with $^{176}\mathrm{Yb}$ at the Coulomb barrier energy,” *Phys. Rev. C*, vol. 89, p. 014614, 2014.

[48] E. M. Kozulin, G. N. Knyazheva, K. V. Novikov, I. M. Itkis, M. G. Itkis, S. N. Dmitriev, Yu. Ts. Oganessian, A. A. Bogachev, N. I. Kozulina, I. Harca, W. H. Trzaska, and T. K. Ghosh, “Fission and quasifission of composite systems with Z=108-120 : Transition from heavy-ion reactions involving S and Ca to Ti and Ni ions,” *Phys. Rev. C*, vol. 94, p. 054613, 2016.

[49] M. G. Itkis, J. Äystö, S. Beghini, A. A. Bogachev, L. Corradi, O. Dorvaux, A. Gadea, G. Giardina, F. Hanappe, I. M. Itkis, M. Jandel, J. Kliman, S. V. Khlebnikov, G. N. Kniajeva, N. A. Kondratiev, E. M. Kozulin, L. Krupa, A. Latina, T. Materna, G. Montagnoli, Yu. Ts. Oganessian, I. V. Pokrovsky, E. V. Prokhorova, N. Rowley, V. A. Rubchenya, A. Ya. Rusanov, R. N. Sagaidak, F. Scarlassara, A. M. Stefanini, L. Stuttge, S. Szilner, M. Trotta, W. H. Trzaska, D. N. Vakhtin, A. M. Vinodkumar, V. M. Voskressenski, and V. I. Zagrebaev, “Shell effects in fission and quasi-fission of heavy and superheavy nuclei,” *Nucl. Phys. A*, vol. 734, pp. 136–147, 2004.

[50] M. G. Itkis, A. A. Bogachev, I. M. Itkis, J. Kliman, G. N. Knyazheva, N. A. Kondratiev, E. M. Kozulin, L. Krupa, Yu. Ts. Oganessian, I. V. Pokrovsky, E. V. Prokhorova, and A. Ya. Rusanov, “The processes of fusion-fission and quasifission of superheavy nuclei,” *Nucl. Phys. A*, vol. 787, pp. 150–159, 2007.

[51] M. G. Itkis, I. M. Itkis, G. N. Knyazheva, and E. M. Kozulin, “Fusion-fission and quasifission of superheavy systems in heavy-ion induced reactions,” *Nucl. Phys. A*, vol. 834, pp. 374c–377c, 2010.

[52] C. Simenel, D. J. Hinde, R. du Rietz, M. Dasgupta, M. Evers, C. J. Lin, D. H. Luong, and A. Wakhle, “Influence of entrance-channel magicity and isospin on quasi-fission,” *Phys. Lett. B*, vol. 710, pp. 607–611, 2012.

[53] D. J. Hinde, R. du Rietz, M. Dasgupta, R. G. Thomas, and L. R. Gasques, “Two Distinct Quasifission Modes in the $^{32}\mathrm{S} + {}^{232}\mathrm{Th}$ Reaction,” *Phys. Rev. Lett.*, vol. 101, p. 092701, 2008.

[54] D. J. Hinde, “Fusion and Quasifission in Superheavy Element Synthesis,” *Nuclear Physics News*, vol. 28, pp. 13–19, 2018.

[55] D. J. Hinde, R. d. Rietz, D. Y. Jeung, K. J. Cook, M. Dasgupta, E. C. Simpson, R. G. Thomas, M. Evers, C. J. Lin, D. H. Luong, L. R. Gasques, R. Rafiei, A. Wakhle, and C. Simenel, “Experimental investigation of the role of shell structure in quasifission mass distributions,” *Phys. Rev. C*, vol. 106, p. 064614, 2022.

[56] T. Niwase, Y. X. Watanabe, Y. Hirayama, M. Mukai, P. Schury, A. N. Andreyev, T. Hashimoto, S. Iimura, H. Ishiyama, Y. Ito, S. C. Jeong, D. Kaji, S. Kimura, H. Miyatake, K. Morimoto, J.-Y. Moon, M. Oyaizu, M. Rosenbusch, A. Taniguchi, and M. Wada, “Discovery of new isotope $^{241}\mathrm{U}$ and systematic high-precision atomic mass measurements of neutron-rich pa-pu nuclei produced via multinucleon transfer reactions,” *Phys. Rev. Lett.*, vol. 130, p. 132502, 2023.

[57] M. Schädel, W. Brüchle, H. Gäggeler, J. V. Kratz, K. Sümmerer, G. Wirth, G. Herrmann, R. Stakemann, G. Tittel, N. Trautmann, J. M. Nitschke, E. K. Hulet, R. W. Lougheed, R. L. Hahn, and R. L. Ferguson, “Actinide Production in Collisions of $^{238}\mathrm{U}$ with $^{248}\mathrm{Cm}$,” *Phys. Rev. Lett.*, vol. 48, pp. 852–855, 1982.

[58] H. Gäggeler, W. Brüchle, M. Brügger, M. Schädel, K. Sümmerer, G. Wirth, J. V. Kratz, M. Lerch, T. Blaich, G. Herrmann, N. Hildebrand, N. Trautmann, D. Lee, K. J. Moody, K. E. Gregorich, R. B. Welch, G. T. Seaborg, D. C. Hoffman, W. R. Daniels, M. M. Fowler, and H. R. von Gunten, “Production of cold target-like fragments in the reaction $^{48}\mathrm{Ca} + {}^{248}\mathrm{Cm}$,” *Phys. Rev. C*, vol. 33, pp. 1983–1987, 1986.

[59] C. H. Dasso, G. Pollarolo, and A. Winther, “Systematics of Isotope Production with Radioactive Beams,” *Phys. Rev. Lett.*, vol. 73, pp. 1907–1910, 1994.

[60] C. H. Dasso, G. Pollarolo, and A. Winther, “Particle evaporation following multinucleon transfer processes with radioactive beams,” *Phys. Rev. C*, vol. 52, pp. 2264–2265, 1995.

[61] G. G. Adamian, N. V. Antonenko, and W. Scheid, "Characteristics of quasifission products within the dinuclear system model," *Phys. Rev. C*, vol. 68, p. 034601, 2003.

[62] G. G. Adamian, N. V. Antonenko, and A. S. Zubov, "Production of unknown transactinides in asymmetry-exit-channel quasifission reactions," *Phys. Rev. C*, vol. 71, p. 034603, 2005.

[63] Valery Zagrebaev and Walter Greiner, "Production of New Heavy Isotopes in Low–Energy Multinucleon Transfer Reactions," *Phys. Rev. Lett.*, vol. 101, p. 122701, 2008.

[64] David J. Kedziora and Cédric Simenel, "New inverse quasifission mechanism to produce neutron-rich transfermium nuclei," *Phys. Rev. C*, vol. 81, p. 044613, 2010.

[65] V. I. Zagrebaev and W. Greiner, "Production of heavy and superheavy neutron-rich nuclei in transfer reactions," *Phys. Rev. C*, vol. 83, p. 044618, 2011.

[66] V. I. Zagrebaev and W. Greiner, "Production of heavy trans-target nuclei in multinucleon transfer reactions," *Phys. Rev. C*, vol. 87, p. 034608, 2013.

[67] Kazuyuki Sekizawa and Kazuhiro Yabana, "Time-dependent Hartree-Fock calculations for multinucleon transfer processes in $^{40,48}\mathrm{Ca}+{}^{124}\mathrm{Sn}$, $^{40}\mathrm{Ca}+{}^{208}\mathrm{Pb}$, and $^{58}\mathrm{Ni}+{}^{208}\mathrm{Pb}$ reactions," *Phys. Rev. C*, vol. 88, p. 014614, 2013.

[68] K. Sekizawa and K. Yabana, "Particle-number projection method in time-dependent Hartree-Fock theory: Properties of reaction products," *Phys. Rev. C*, vol. 90, p. 064614, 2014.

[69] K. Sekizawa and K. Yabana, "Time-dependent Hartree–Fock calculations for multi-nucleon transfer processes: Effects of particle evaporation on production cross sections," *EPJ Web Conf.*, vol. 86, p. 00043, 2015.

[70] K. Sekizawa and K. Yabana, "Time-dependent Hartree-Fock calculations for multinucleon transfer and quasifission processes in the $^{64}\mathrm{Ni}+{}^{238}\mathrm{U}$ reaction," *Phys. Rev. C*, vol. 93, p. 054616, 2016.

[71] K. Sekizawa, "Microscopic description of production cross sections including deexcitation effects," *Phys. Rev. C*, vol. 96, p. 014615, 2017.

[72] K. Sekizawa, "Enhanced nucleon transfer in tip collisions of $^{238}\mathrm{U} + {}^{124}\mathrm{Sn}$," *Phys. Rev. C*, vol. 96, p. 041601(R), 2017.

[73] K. Sekizawa and S. Ayik, "Quantal diffusion approach for multinucleon transfer processes in the $^{58,64}\mathrm{Ni} +^{208}\mathrm{Pb}$ reactions: Toward the production of unknown neutron-rich nuclei," *Phys. Rev. C*, vol. 102, p. 014620, 2020.

[74] S. Ayik, B. Yilmaz, O. Yilmaz, A. S. Umar, and G. Turan, "Multinucleon transfer in central collisions of $^{238}\mathrm{U} + {}^{238}\mathrm{U}$," *Phys. Rev. C*, vol. 96, p. 024611, 2017.

[75] S. Ayik, B. Yilmaz, O. Yilmaz, and A. S. Umar, "Quantal diffusion description of multinucleon transfers in heavy–ion collisions," *Phys. Rev. C*, vol. 97, p. 054618, 2018.

[76] S. Ayik, B. Yilmaz, O. Yilmaz, and A. S. Umar, "Quantal diffusion approach for multinucleon transfers in $\mathrm{Xe} + \mathrm{Pb}$ collisions," *Phys. Rev. C*, vol. 100, p. 014609, 2019.

[77] S. Ayik, O. Yilmaz, B. Yilmaz, and A. S. Umar, "Heavy-isotope production in $^{136}\mathrm{Xe} + {}^{208}\mathrm{Pb}$ collisions at $E_{\mathrm{c.m.}} = 514$ MeV," *Phys. Rev. C*, vol. 100, p. 044614, 2019.

[78] S. Ayik, B. Yilmaz, O. Yilmaz, and A. S. Umar, "Merging of transport theory with the time-dependent Hartree-Fock approach: Multinucleon transfer in $\mathrm{U} + \mathrm{U}$ collisions," *Phys. Rev. C*, vol. 102, p. 024619, 2020.

[79] S. Ayik, M. Arik, E. C. Karanfil, O. Yilmaz, B. Yilmaz, and A. S. Umar, "Quantal diffusion description of isotope production via the multinucleon transfer mechanism in $^{48}\mathrm{Ca} +^{238}\mathrm{U}$ collisions," *Phys. Rev. C*, vol. 104, p. 054614, 2021.

[80] V. V. Saiko and A. V. Karpov, "Analysis of multinucleon transfer reactions with spherical and statically deformed nuclei using a Langevin-type approach," *Phys. Rev. C*, vol. 99, p. 014613, 2019.

[81] V. Saiko and A. Karpov, "Multinucleon transfer as a method for production of

new heavy neutron-enriched isotopes of transuranium elements," *Eur. Phys. J. A*, vol. 58, p. 41, 2022.

[82] L. Zhu, J. Su, W.-J. Xie, and F.-S. Zhang, "Theoretical study on production of heavy neutron-rich isotopes around the N=126 shell closure in radioactive beam induced transfer reactions," *Phys. Lett. B*, vol. 767, pp. 437–442, 2017.

[83] L. Zhu, "Shell inhibition on production of $\mathrm{N} = 126$ isotones in multinucleon transfer reactions," *Phys. Lett. B*, vol. 816, p. 136226, 2021.

[84] Z. Liao, L. Zhu, J. Su, and C. Li, "Dynamics of charge equilibration and effects on producing neutron-rich isotopes around n=126 in multinucleon transfer reactions," *Physical Review C*, vol. 107, p. 014614, 2023.

[85] Z. Liao, Z. Gao, Y. Yang, L. Zhu, and J. Su, "Shell effects on the drift and fluctuation in multinucleon transfer reactions," *Physical Review C*, vol. 109, p. 054612, 2024.

[86] L. Zhu, "New model based on coupling the master and langevin equations in the study of multinucleon transfer reactions," *Physics Letters B*, vol. 849, p. 138423, 2024.

[87] Y. H. Zhang, J. J. Li, N. Tang, X. R. Zhang, Z. Liu, and F. S. Zhang, "Production cross sections of new neutron-rich isotopes with z=92-106 in the multinucleon transfer reaction au 197 + th 232," *Physical Review C*, vol. 107, p. 024604, 2023.

[88] D. D. Zhang, D. Vretenar, T. Nikšić, P. W. Zhao, and J. Meng, "Multinucleon transfer with time-dependent covariant density functional theory," *Physical Review C*, vol. 109, p. 024614, 2024.

[89] Y. H. Zhang, J. J. Li, C. Li, M. H. Zhang, Y. Zou, and F. S. Zhang, "Microscopic study of the production of neutron-rich isotopes near n=126 in the multinucleon transfer reactions kr 78,82,86 + pb 208," *Physical Review C*, vol. 109, p. 044617, 2024.

[90] V. V. Saiko and A. V. Karpov, "Production of neutron-enriched isotopes along magic number n=126 by multinucleon transfer reactions with radioactive-ion beams," *Physical Review C*, vol. 109, p. 064607, 2024.

[91] Y. X. Watanabe, Y. H. Kim, S. C. Jeong, Y. Hirayama, N. Imai, H. Ishiyama, H. S. Jung, H. Miyatake, S. Choi, J. S. Song, E. Clement, G. de France, A. Navin, M. Rejmund, C. Schmitt, G. Pollarolo, L. Corradi, E. Fioretto, D. Montanari, M. Niikura, D. Suzuki, H. Nishibata, and J. Takatsu, "Pathway for the Production of Neutron–Rich Isotopes around the $N = 126$ Shell Closure," *Phys. Rev. Lett.*, vol. 115, p. 172503, 2015.

[92] E. M. Kozulin, V. I. Zagrebaev, G. N. Knyazheva, I. M. Itkis, K. V. Novikov, M. G. Itkis, S. N. Dmitriev, I. M. Harca, A. E. Bondarchenko, A. V. Karpov, V. V. Saiko, and E. Vardaci, "Inverse quasifission in the reactions $^{156,160}\mathrm{Gd}+^{186}\mathrm{W}$," *Phys. Rev. C*, vol. 96, p. 064621, 2017.

[93] V. Saiko and A. Karpov, "Role of charge equilibration in multinucleon transfer in damped collisions of heavy ions," *EPJ Web Conf.*, vol. 223, p. 01055, 2019.

[94] V. E. Oberacker, A. S. Umar, and C. Simenel, "Dissipative dynamics in quasifission," *Phys. Rev. C*, vol. 90, p. 054605, 2014.

[95] D. J. Hinde, M. Dasgupta, J. R. Leigh, J. C. Mein, C. R. Morton, J. O. Newton, and H. Timmers, "Conclusive evidence for the influence of nuclear orientation on quasifission," *Phys. Rev. C*, vol. 53, pp. 1290–1300, 1996.

[96] G. N. Knyazheva, E. M. Kozulin, R. N. Sagaidak, A. Yu. Chizhov, M. G. Itkis, N. A. Kondratiev, V. M. Voskressensky, A. M. Stefanini, B. R. Behera, L. Corradi, E. Fioretto, A. Gadea, A. Latina, S. Szilner, M. Trotta, S. Beghini, G. Montagnoli, F. Scarlassara, F. Haas, N. Rowley, P. R. S. Gomes, and A. Szanto de Toledo, "Quasifission processes in $^{40,48}\mathrm{Ca}+{}^{144,154}\mathrm{Sm}$ reactions," *Phys. Rev. C*, vol. 75, p. 064602, 2007.

[97] K. Nishio, H. Ikezoe, S. Mitsuoka, I. Nishinaka, Y. Nagame, Y. Watanabe, T. Ohtsuki, K. Hirose, and S. Hofmann, "Effects of nuclear orientation on the mass distribution of fission fragments in the reaction of $^{36}\mathrm{S}+{}^{238}\mathrm{U}$," *Phys. Rev. C*, vol. 77, p. 064607, 2008.

[98] T. K. Ghosh, S. Pal, T. Sinha, S. Chattopadhyay, P. Bhattacharya, D. C. Biswas, and K. S. Golda, "Anomalous increase in width of fission-fragment mass distribution as a probe for onset of quasifission reactions in deformed target-

projectile system at near and sub-barrier energies," *Phys. Rev. C*, vol. 70, p. 011604, 2004.

[99] A. Wakhle, C. Simenel, D. J. Hinde, M. Dasgupta, M. Evers, D. H. Luong, R. du Rietz, and E. Williams, "Interplay between Quantum Shells and Orientation in Quasifission," *Phys. Rev. Lett.*, vol. 113, p. 182502, 2014.

[100] A. Iwamoto, P. Möller, J. Nix, and H. Sagawa, "Collisions of deformed nuclei: A path to the far side of the superheavy island," *Nucl. Phys. A*, vol. 596, pp. 329–354, 1996.

[101] K. Nishio, H. Ikezoe, S. Mitsuoka, and J. Lu, "Fusion of deformed nuclei in the reactions of $^{76}\mathrm{Ge}+{}^{150}\mathrm{Nd}$ and $^{28}\mathrm{Si}+{}^{198}\mathrm{Pt}$ at the Coulomb barrier region," *Phys. Rev. C*, vol. 62, p. 014602, 2000.

[102] S. Mitsuoka, H. Ikezoe, K. Nishio, and J. Lu, "Sub-barrier fusion of deformed nuclei in $^{60}\mathrm{Ni}+{}^{154}\mathrm{Sm}$ and $^{32}\mathrm{S}+{}^{182}\mathrm{W}$ reactions," *Phys. Rev. C*, vol. 62, p. 054603, 2000.

[103] B. B. Back, P. B. Fernandez, B. G. Glagola, D. Henderson, S. Kaufman, J. G. Keller, S. J. Sanders, F. Videbæk, T. F. Wang, and B. D. Wilkins, "Entrance-channel effects in quasifission reactions," *Phys. Rev. C*, vol. 53, pp. 1734–1744, 1996.

[104] D. J. Hinde, M. Dasgupta, and A. Mukherjee, "Severe Inhibition of Fusion by Quasifission in Reactions Forming ^{220}Th," *Phys. Rev. Lett.*, vol. 89, p. 282701, 2002.

[105] R. Rafiei, R. G. Thomas, D. J. Hinde, M. Dasgupta, C. R. Morton, L. R. Gasques, M. L. Brown, and M. D. Rodriguez, "Strong evidence for quasifission in asymmetric reactions forming ^{202}Po," *Phys. Rev. C*, vol. 77, p. 024606, 2008.

[106] I. M. Itkis, E. M. Kozulin, M. G. Itkis, G. N. Knyazheva, A. A. Bogachev, E. V. Chernysheva, L. Krupa, Yu. Ts. Oganessian, V. I. Zagrebaev, A. Ya. Rusanov, F. Goennenwein, O. Dorvaux, L. Stuttgé, F. Hanappe, E. Vardaci, and E. de Goés Brennand, "Fission and quasifission modes in heavy-ion-induced

reactions leading to the formation of Hs*," *Phys. Rev. C*, vol. 83, p. 064613, 2011.

[107] V. I. Zagrebaev, Yu. Ts. Oganessian, M. G. Itkis, and W. Greiner, "Superheavy nuclei and quasi-atoms produced in collisions of transuranium ions," *Phys. Rev. C*, vol. 73, p. 031602(R), 2006.

[108] Valery Zagrebaev and Walter Greiner, "New way for the production of heavy neutron-rich nuclei," *J. Phys. G: Nucl. Part. Phys.*, vol. 35, p. 125103, 2008.

[109] A. V. Karpov and V. V. Saiko, "Modeling near-barrier collisions of heavy ions based on a Langevin-type approach," *Phys. Rev. C*, vol. 96, p. 024618, 2017.

[110] K. Zhao, X. Wu, and Z. Li, "Quantum molecular dynamics study of the mass distribution of products in $7.0A$ MeV $^{238}\mathrm{U} + {}^{238}\mathrm{U}$ collisions," *Phys. Rev. C*, vol. 80, p. 054607, 2009.

[111] Z.-Q. Feng, G.-M. Jin, and J.-Q. Li, "Production of heavy isotopes in transfer reactions by collisions of $^{238}\mathrm{U} + {}^{238}\mathrm{U}$," *Phys. Rev. C*, vol. 80, p. 067601, 2009.

[112] Z.-Q. Feng, "Production of neutron–rich isotopes around $N = 126$ in multinucleon transfer reactions," *Phys. Rev. C*, vol. 95, p. 024615, 2017.

[113] K. Zhao, Z. Li, Y. Zhang, N. Wang, Q. Li, C. Shen, Y. Wang, and X. Wu, "Production of unknown neutron–rich isotopes in $^{238}\mathrm{U} + {}^{238}\mathrm{U}$ collisions at near–barrier energy," *Phys. Rev. C*, vol. 94, p. 024601, 2016.

[114] N. Wang and L. Guo, "New neutron-rich isotope production in $^{154}\mathrm{Sm}+{}^{160}\mathrm{Gd}$," *Phys. Lett. B*, vol. 760, pp. 236–241, 2016.

[115] A. Winther, "Grazing reactions in collisions between heavy nuclei," *Nucl. Phys. A*, vol. 572, pp. 191–235, 1994.

[116] A. Winther, "Dissipation, polarization and fluctuation in grazing heavy-ion collisions and the boundary to the chaotic regime," *Nucl. Phys. A*, vol. 594, pp. 203–245, 1995.

[117] R. Yanez and W. Loveland, "Predicting the production of neutron-rich heavy nuclei in multinucleon transfer reactions using a semi-classical model includ-

ing evaporation and fission competition, grazing-f," *Phys. Rev. C*, vol. 91, p. 044608, 2015.

[118] P. W. Wen, C. J. Lin, C. Li, L. Zhu, F. Zhang, F. S. Zhang, H. M. Jia, F. Yang, N. R. Ma, L. J. Sun, D. X. Wang, F. P. Zhong, H. H. Sun, L. Yang, and X. X. Xu, "Evaporation and fission of the primary fragments produced by multinucleon transfer reactions," *Phys. Rev. C*, vol. 99, p. 034606, 2019.

[119] C. Simenel, "Particle Transfer Reactions with the Time-Dependent Hartree-Fock Theory Using a Particle Number Projection Technique," *Phys. Rev. Lett.*, vol. 105, p. 192701, 2010.

[120] C. Simenel, K. Godbey, and A. S. Umar, "Timescales of Quantum Equilibration, Dissipation and Fluctuation in Nuclear Collisions," *Phys. Rev. Lett.*, vol. 124, p. 212504, 2020.

[121] T. Nakatsukasa, K. Matsuyanagi, M. Matsuo, and K. Yabana, "Time-dependent density-functional description of nuclear dynamics," *Rev. Mod. Phys.*, vol. 88, p. 045004, 2016.

[122] A. S. Umar, V. E. Oberacker, and C. Simenel, "Shape evolution and collective dynamics of quasifission in the time-dependent Hartree-Fock approach," *Phys. Rev. C*, vol. 92, p. 024621, 2015.

[123] A. S. Umar and V. E. Oberacker, "Time-dependent HF approach to SHE dynamics," *Nucl. Phys. A*, vol. 944, pp. 238–256, 2015.

[124] A. S. Umar, V. E. Oberacker, and C. Simenel, "Fusion and quasifission dynamics in the reactions $^{48}\mathrm{Ca}+{}^{249}\mathrm{Bk}$ and $^{50}\mathrm{Ti}+{}^{249}\mathrm{Bk}$ using a time-dependent Hartree-Fock approach," *Phys. Rev. C*, vol. 94, p. 024605, 2016.

[125] K. Hammerton, Z. Kohley, D. J. Hinde, M. Dasgupta, A. Wakhle, E. Williams, V. E. Oberacker, A. S. Umar, I. P. Carter, K. J. Cook, J. Greene, D. Y. Jeung, D. H. Luong, S. D. McNeil, C. S. Palshetkar, D. C. Rafferty, C. Simenel, and K. Stiefel, "Reduced quasifission competition in fusion reactions forming neutron-rich heavy elements," *Phys. Rev. C*, vol. 91, p. 041602(R), 2015.

[126] A. S. Umar, C. Simenel, and W. Ye, "Transport properties of isospin asymmetric nuclear matter using the time-dependent Hartree–Fock method," *Phys. Rev. C*, vol. 96, p. 024625, 2017.

[127] C. Simenel, "Nuclear quantum many-body dynamics," *Eur. Phys. J. A*, vol. 48, p. 152, 2012.

[128] C. Simenel and A. S. Umar, "Heavy-ion collisions and fission dynamics with the time–dependent Hartree-Fock theory and its extensions," *Prog. Part. Nucl. Phys.*, vol. 103, pp. 19–66, 2018.

[129] K. Sekizawa and K. Hagino, "Time-dependent Hartree-Fock plus Langevin approach for hot fusion reactions to synthesize the $Z = 120$ superheavy element," *Phys. Rev. C*, vol. 99, p. 051602, 2019.

[130] P. D. Stevenson and M. C. Barton, "Low–energy heavy-ion reactions and the Skyrme effective interaction," *Prog. Part. Nucl. Phys.*, vol. 104, pp. 142–164, 2019.

[131] S. Ayik and K. Sekizawa, "Kinetic-energy dissipation and fluctuations in strongly damped heavy-ion collisions within the stochastic mean-field approach," *Phys. Rev. C*, vol. 102, p. 064619, 2020.

[132] Sonika, B. J. Roy, A. Parmar, U. K. Pal, H. Kumawat, V. Jha, S. K. Pandit, V. V. Parkar, K. Ramachandran, K. Mahata, A. Pal, S. Santra, A. K. Mohanty, and K. Sekizawa, "Multinucleon transfer study in ^{206}Pb$(^{18}\mathrm{O}, x)$ at energies above the Coulomb barrier," *Phys. Rev. C*, vol. 92, p. 024603, 2015.

[133] B. J. Roy, Y. Sawant, P. Patwari, S. Santra, A. Pal, A. Kundu, D. Chattopadhyay, V. Jha, S. K. Pandit, V. V. Parkar, K. Ramachandran, K. Mahata, B. K. Nayak, A. Saxena, S. Kailas, T. N. Nag, R. N. Sahoo, P. P. Singh, and K. Sekizawa, "Deep-inelastic multinucleon transfer processes in the $^{16}\mathrm{O} + {}^{27}\mathrm{Al}$ reaction," *Phys. Rev. C*, vol. 97, p. 034603, 2018.

[134] Z. Wu and L. Guo, "Microscopic studies of production cross sections in multinucleon transfer reaction $^{58}\mathrm{Ni} +^{124}\mathrm{Sn}$," *Phys. Rev. C*, vol. 100, p. 014612, 2019.

[135] C. L. Jiang, D. Santiago-Gonzalez, S. Almaraz-Calderon, K. E. Rehm, B. B. Back, K. Auranen, M. L. Avila, A. D. Ayangeakaa, S. Bottoni, M. P. Carpenter, C. Dickerson, B. DiGiovine, J. P. Greene, C. R. Hoffman, R. V. F. Janssens, B. P. Kay, S. A. Kuvin, T. Lauritsen, R. C. Pardo, J. Sethi, D. Seweryniak, R. Talwar, C. Ugalde, S. Zhu, D. Bourgin, S. Courtin, F. Haas, M. Heine, G. Fruet, D. Montanari, D. G. Jenkins, L. Morris, A. Lefebvre-Schuhl, M. Alcorta, X. Fang, X. D. Tang, B. Bucher, C. M. Deibel, and S. T. Marley, "Reaction rate for carbon burning in massive stars," *Phys. Rev. C*, vol. 97, p. 012801, 2018.

[136] X. Jiang and N. Wang, "Probing the production mechanism of neutron-rich nuclei in multinucleon transfer reactions," *Phys. Rev. C*, vol. 101, p. 014604, 2020.

[137] X. Jiang and N. Wang, "Predictions of New Neutron-Rich Isotopes at $N = 126$ in the Multinucleon Transfer Reaction $^{136}\mathrm{Xe}+^{194}\mathrm{Ir}$," *Front. Phys.*, vol. 8, p. 38, 2020.

[138] M. Tohyama and A. S. Umar, "Quadrupole resonances in unstable oxygen isotopes in time-dependent density-matrix formalism," *Phys. Lett. B*, vol. 549, pp. 72–78, 2002.

[139] M. Tohyama, "Applications of Time-Dependent Density-Matrix Approach," *Front. Phys.*, vol. 8, p. 67, 2020.

[140] C. Simenel, "Particle-Number Fluctuations and Correlations in Transfer Reactions Obtained Using the Balian-Vénéroni Variational Principle," *Phys. Rev. Lett.*, vol. 106, p. 112502, 2011.

[141] D. Lacroix and S. Ayik, "Stochastic quantum dynamics beyond mean field," *Eur. Phys. J. A*, vol. 50, p. 95, 2014.

[142] R. Balian and M. Vénéroni, "Time-dependent variational principle for the expectation value of an observable: Mean-field applications," *Ann. Phys. (NY)*, vol. 164, p. 334, 1985.

[143] R. Balian and M. Vénéroni, "Correlations and fluctuations in static and dynamic mean-field approaches," *Ann. Phys.*, vol. 216, p. 351, 1992.

[144] E. Williams, K. Sekizawa, D. J. Hinde, C. Simenel, M. Dasgupta, I. P. Carter, K. J. Cook, D. Y. Jeung, S. D. McNeil, C. S. Palshetkar, D. C. Rafferty, K. Ramachandran, and A. Wakhle, "Exploring Zeptosecond Quantum Equilibration Dynamics: From Deep-Inelastic to Fusion-Fission Outcomes in $^{58}\mathrm{Ni} + {}^{60}\mathrm{Ni}$ Reactions," *Phys. Rev. Lett.*, vol. 120, p. 022501, 2018.

[145] K. Godbey and A. S. Umar, "Quasifission Dynamics in Microscopic Theories," *Front. Phys.*, vol. 8, p. 40, 2020.

[146] K. Godbey, C. Simenel, and A. S. Umar, "Microscopic predictions for the production of neutron-rich nuclei in the reaction $^{176}\mathrm{Yb} + {}^{176}\mathrm{Yb}$," *Phys. Rev. C*, vol. 101, p. 034602, 2020.

[147] J. M. A. Broomfield and P. D. Stevenson, "Mass dispersions from giant dipole resonances using the Balian-Vénéroni variational approach," *J. Phys. G: Nucl. Part. Phys.*, vol. 35, p. 095102, 2008.

[148] S. Ayik, "A stochastic mean-field approach for nuclear dynamics," *Phys. Lett. B*, vol. 658, p. 174, 2008.

[149] Kouhei Washiyama, Sakir Ayik, and Denis Lacroix, "Mass dispersion in transfer reactions with a stochastic mean-field theory," *Phys. Rev. C*, vol. 80, p. 031602, 2009.

[150] B. Yilmaz, S. Ayik, D. Lacroix, and K. Washiyama, "Nucleon exchange mechanism in heavy-ion collisions at near-barrier energies," *Phys. Rev. C*, vol. 83, p. 064615, 2011.

[151] B. Yilmaz, S. Ayik, D. Lacroix, and O. Yilmaz, "Nucleon exchange in heavy-ion collisions within a stochastic mean-field approach," *Phys. Rev. C*, vol. 90, p. 024613, 2014.

[152] B. Yilmaz, S. Ayik, O. Yilmaz, and A. S. Umar, "Multinucleon transfer in $^{58}\mathrm{Ni} + {}^{60}\mathrm{Ni}$ and $^{60}\mathrm{Ni} + {}^{60}\mathrm{Ni}$ in a stochastic mean-field approach," *Phys. Rev. C*, vol. 98, p. 034604, 2018.

[153] S. Ayik, B. Yilmaz, and O. Yilmaz, "Multinucleon exchange in quasifission reactions," *Phys. Rev. C*, vol. 92, p. 064615, 2015.

[154] S. Ayik, O. Yilmaz, B. Yilmaz, A. S. Umar, A. Gokalp, G. Turan, and D. Lacroix, “Quantal description of nucleon exchange in a stochastic mean-field approach,” *Phys. Rev. C*, vol. 91, p. 054601, 2015.

[155] S. Ayik, O. Yilmaz, B. Yilmaz, and A. S. Umar, “Quantal nucleon diffusion: Central collisions of symmetric nuclei,” *Phys. Rev. C*, vol. 94, p. 044624, 2016.

[156] O. Yilmaz, G. Turan, and B. Yilmaz, “Quasi-fission and fusion-fission reactions in $^{48}\mathrm{Ca} + {}^{208}\mathrm{Pb}$ collisions at $E_{\mathrm{c.m.}} = 190$ MeV,” *Eur. Phys. J. A*, vol. 56, p. 37, 2020.

[157] S. Ayik, M. Arik, E. Erbayri, O. Yilmaz, and A. S. Umar, “Multinucleon transfer mechanism in $^{160}\mathrm{Gd} +^{186}\mathrm{W}$ collisions in stochastic mean-field theory,” *Phys. Rev. C*, vol. 108, p. 054605, Nov 2023.

[158] A. Kayaalp, S. E. Ocal, B. Yaprakli, M. Arik, S. Ayik, O. Yilmaz, and A. S. Umar, “A theoretical study on quasifission and fusion–fission processes in heavy-ion collisions,” *The European Physical Journal A 2024 60:4*, vol. 60, pp. 1–10, 2024.

[159] Y. Tanimura, D. Lacroix, and S. Ayik, “Microscopic Phase–Space Exploration Modeling of $^{258}\mathrm{Fm}$ Spontaneous Fission,” *Phys. Rev. Lett.*, vol. 118, p. 152501, 2017.

[160] D. Lacroix, S. Ayik, and B. Yilmaz, “Symmetry breaking and fluctuations within stochastic mean-field dynamics: Importance of initial quantum fluctuations,” *Phys. Rev. C*, vol. 85, p. 041602, 2012.

[161] S. Ayik, N. Er, O. Yilmaz, and A. Gokalp, “Quantal effects on spinodal instabilities in charge asymmetric nuclear matter,” *Nucl. Phys. A*, vol. 812, pp. 44–57, 2008.

[162] S. Ayik, O. Yilmaz, N. Er, A. Gokalp, and P. Ring, “Spinodal instabilities in nuclear matter in a stochastic relativistic mean-field approach,” *Phys. Rev. C*, vol. 80, p. 034613, 2009.

[163] S. Ayik, O. Yilmaz, F. Acar, B. Danisman, N. Er, and A. Gokalp, “Investigations of instabilities in nuclear matter in stochastic relativistic models,” *Nucl. Phys. A*, vol. 859, pp. 73–86, 2011.

[164] O. Yilmaz, S. Ayik, and A. Gokalp, "Quantal description of instabilities in nuclear matter in a stochastic relativistic model," *Eur. Phys. J. A*, vol. 47, p. 123, 2011.

[165] O. Yilmaz, S. Ayik, F. Acar, S. Saatci, and A. Gokalp, "Investigations of spinodal dynamics in asymmetric nuclear matter within a stochastic relativistic model," *Eur. Phys. J. A*, vol. 49, p. 33, 2013.

[166] O. Yilmaz, S. Ayik, F. Acar, and A. Gokalp, "Growth of spinodal instabilities in nuclear matter," *Phys. Rev. C*, vol. 91, p. 014605, 2015.

[167] F. Acar, S. Ayik, O. Yilmaz, and A. Gokalp, "Growth of spinodal instabilities in nuclear matter. ii. asymmetric matter," *Phys. Rev. C*, vol. 92, p. 034605, 2015.

[168] J. Randrup, "Theory of transfer-induced transport in nuclear collisions," *Nucl. Phys. A*, vol. 327, pp. 490–516, 1979.

[169] W. U. Schröder, J. R. Huizenga, and J. Randrup, "Correlated mass and charge transport induced by statistical nucleon exchange in damped nuclear reactions," *Phys. Lett. B*, vol. 98, pp. 355–359, 1981.

[170] A. C. Merchant and W. Nörenberg, "Microscopic transport theory of heavy-ion collisions," *Z. Phys. A*, vol. 308, pp. 315–327, 1982.

[171] U. Weiss, *Quantum Dissipative Systems*. Singapore: World Scientific, second ed., 1999.

[172] C. W. Gardiner, *Quantum Noise*. Berlin: Springer–Verlag, 1991.

[173] Hannes Risken and Till Frank, *The Fokker–Planck Equation*. Berlin: Springer–Verlag, 1996.

[174] J. M. Gates, C. E. Düllmann, M. Schädel, A. Yakushev, A. Türler, K. Eberhardt, J. V. Kratz, D. Ackermann, L.-L. Andersson, M. Block, W. Brüchle, J. Dvorak, H. G. Essel, P. A. Ellison, J. Even, U. Forsberg, J. Gellanki, A. Gorshkov, R. Graeger, K. E. Gregorich, W. Hartmann, R.-D. Herzberg, F. P. Heßberger, D. Hild, A. Hübner, E. Jäger, J. Khuyagbaatar, B. Kindler, J. Krier, N. Kurz, S. Lahiri, D. Liebe, B. Lommel, M. Maiti, H. Nitsche, J. P. Omtvedt,

E. Parr, D. Rudolph, J. Runke, H. Schaffner, B. Schausten, E. Schimpf, A. Semchenkov, J. Steiner, P. Thörle-Pospiech, J. Uusitalo, M. Wegrzecki, and N. Wiehl, "First superheavy element experiments at the GSI recoil separator TASCA: The production and decay of element 114 in the ^{244}Pu(^{48}Ca,3-4n) reaction," *Phys. Rev. C*, vol. 83, p. 054618, 2011.

[175] R. Kumar, M. Maiti, A. Pal, S. Santra, P. Kaur, M. Sagwal, A. Singh, P. C. Rout, A. Baishya, R. Gandhi, and T. Santhosh, "Shell effect driven fission modes in fragment mass and total kinetic energy distribution of ^{192}Hg*," *Phys. Rev. C*, vol. 107, p. 034614, 2023.

[176] K. Banerjee, D. J. Hinde, M. Dasgupta, J. Sadhukhan, E. C. Simpson, D. Y. Jeung, C. Simenel, B. M. A. Swinton-Bland, E. Williams, L. T. Bezzina, I. P. Carter, K. J. Cook, H. M. Albers, Ch.E. Düllmann, J. Khuyagbaatar, B. Kindler, B. Lommel, C. Mokry, E. Prasad, J. Runke, N. Schunck, C. Sengupta, J. F. Smith, P. Thörle-Pospiech, N. Trautmann, K. Vo-Phuoc, J. Walshe, and A. Yakushev, "Sensitive search for near-symmetric and super-asymmetric fusion-fission of the superheavy element Flerovium (Z=114)," *Phys. Lett. B*, vol. 820, p. 136601, 2021.

[177] L. Guo, C. Shen, C. Yu, and Z. Wu, "Isotopic trends of quasifission and fusion-fission in the reactions ^{48}Ca + ^{239,244}Pu," *Phys. Rev. C*, vol. 98, p. 064609, 2018.

[178] "Nuclear reactions video project, low energy nuclear knowledge base, `http://nrv.jinr.ru/nrv/`." Last accessed: 2023-12-27.

[179] R. Bass, *Nuclear Reactions with Heavy Ions*. New York: Springer–Verlag, 1980.

[180] A. S. Umar, M. R. Strayer, J. S. Wu, D. J. Dean, and M. C. Güçlü, "Nuclear Hartree-Fock calculations with splines," *Phys. Rev. C*, vol. 44, pp. 2512–2521, 1991.

[181] A. S. Umar and V. E. Oberacker, "Three-dimensional unrestricted time-dependent Hartree-Fock fusion calculations using the full Skyrme interaction," *Phys. Rev. C*, vol. 73, p. 054607, 2006.

[182] E. Chabanat, P. Bonche, P. Haensel, J. Meyer, and R. Schaeffer, “A Skyrme parametrization from subnuclear to neutron star densities Part II. Nuclei far from stabilities,” *Nucl. Phys. A*, vol. 635, pp. 231–256, 1998.

[183] Ka–Hae Kim, Takaharu Otsuka, and Paul Bonche, “Three-dimensional TDHF calculations for reactions of unstable nuclei,” *J. Phys. G: Nucl. Part. Phys.*, vol. 23, p. 1267, 1997.